



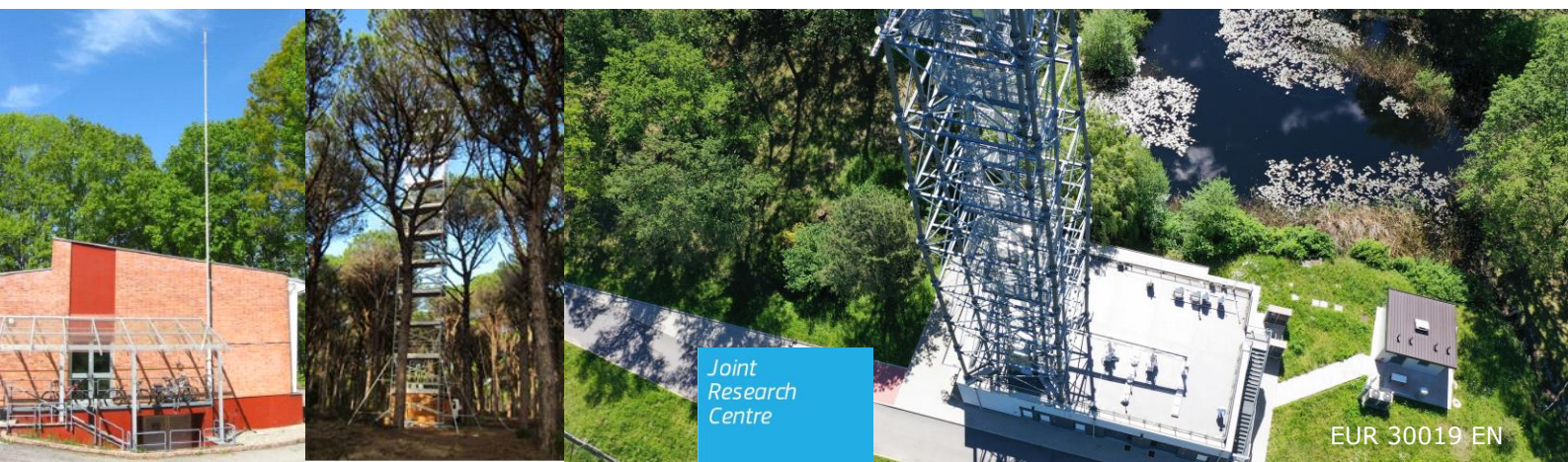
JRC TECHNICAL REPORTS

The European Commission Atmospheric Observatory

2018 Report

J.P. Putaud, N. Arriga, P. Bergamaschi, F. Cavalli,
R. Connolly, O. Gazetas, I. Goded, F. Grassi, C.
Gruening, N.R. Jensen, F. Lagler, G. Manca, S.
Martins Dos Santos, M. Matteucci, R. Passarella,
V. Pedroni.

2019



EUR 30019 EN

This publication is a Technical report by the Joint Research Centre (JRC), the European Commission's science and knowledge service. It aims to provide evidence-based scientific support to the European policymaking process. The scientific output expressed does not imply a policy position of the European Commission. Neither the European Commission nor any person acting on behalf of the Commission is responsible for the use that might be made of this publication.

Contact information

Name: Jean-Philippe Putaud
Address: European Commission, Joint Research Centre, Ispra, Italy
E-mail: jean.putaud@ec.europa.eu

EU Science Hub

<https://ec.europa.eu/jrc>

JRC 118992

EUR 30019 EN

PDF	ISBN 978-92-76-14183-9	ISSN 1031-9424	doi:10.2760/47713
Print	ISBN 978-92-76-14184-6	ISSN 1018-5593	doi:10.2760/510610

Luxembourg: Publications Office of the European Union, 2019

© European Union, 2019

The reuse policy of the European Commission is implemented by Commission Decision 2011/833/EU of 12 December 2011 on the reuse of Commission documents (OJ L 330, 14.12.2011, p. 39). Reuse is authorised, provided the source of the document is acknowledged and its original meaning or message is not distorted. The European Commission shall not be liable for any consequence stemming from the reuse. For any use or reproduction of photos or other material that is not owned by the EU, permission must be sought directly from the copyright holders.

All content © European Union 2019, except: *Fig. 1 (background from Google Earth), Fig. 15 (EMEP), Fig. 20 (Thermo Scientific), Fig. 57 (Gill Instruments), Fig. 58 (LI-COR), Fig. 59 (Wikipedia), and Fig. 60 (Schlumberger Water Services).*

How to cite this report: Putaud, J.P., Arriga, N., Bergamaschi, P., Cavalli, F., Connolly, R., Goded, I., Gazetas, O., Grassi, F., Gruening, C., Jensen, N.R., Lagler, F., Manca, G., Martins Dos Santos, S., Matteucci, M., Passarella, R., Pedroni, V., *The European Commission Atmospheric Observatory: 2018 report*, EUR 30019 EN, Publications Office of the European Union, Luxembourg, 2019, ISBN 978-92-76-14183-9, doi:10.2760/47713, JRC 118992.

Contents

Abstract	1
1 Introduction.....	3
2 Quality management system.....	4
3 Greenhouse gas concentration monitoring at the JRC-Ispra site	7
3.1 Location.....	7
3.2 Measurement programme	7
3.3 Instrumentation in Building 5	9
3.3.1 Sampling.....	9
3.3.2 Analyses	9
3.4 Instrumentation in the new Atmospheric Observatory (Bd 77R)	11
3.4.1 Air sampling	11
3.4.2 Analyses	11
3.5 Overview of measurement results	16
4 Short-lived atmospheric species at the JRC-Ispra site	25
4.1 Introduction	25
4.1.1 Location	25
4.1.2 Underpinning programmes	25
4.2 Measurements and data processing.....	29
4.2.1 Air pollutant and short-lived radiative forcer measurements at the Atmospheric Observatory in Ispra in 2018	29
4.2.2 Measurement techniques.....	30
4.2.3 On-line data acquisition system/data management.....	41
4.2.4 Data evaluation.....	43
4.3 Quality assurance	47
4.4 Results for the year 2018.....	49
4.4.1 Meteorology	49
4.4.2 Gas phase air pollutants.....	49
4.4.3 Particulate phase.....	53
4.4.4 Wet deposition chemistry	69
4.5 Results of year 2018 in relation to 30+ years of measurements	71
4.5.1 Sulphur and nitrogen compounds	71
4.5.2 Particulate matter mass	73
4.5.3 Ozone.....	73
4.5.4 Aerosol micro-physical and optical properties.....	75
4.6 Conclusions.....	75

5. Atmosphere – Biosphere flux monitoring at the forest station of San Rossore.....	79
5.1 Location and site description	79
5.2 Measurements in 2018	81
5.3 Description of the instruments.....	82
5.3.1 Infrastructural	82
5.3.2 Ecosystem fluxes	82
5.3.3 Radiation instruments.....	84
5.3.4 Meteorological sensors.....	84
5.3.5 Soil instruments.....	84
5.3.6 Flux data processing.....	87
5.4 Results of the year 2018.....	89
5.4.1 Meteorology	89
5.4.2 Radiation	89
5.4.3 Soil meteo-climatic variables	91
5.4.4 Eddy covariance flux measurements	91
5.4.5 Ancillary measurements.....	95
Links	98
List of figures.....	99
List of tables.....	102

Abstract

A comprehensive set of essential atmospheric variables have been measured in 2018 at the European Commission Atmospheric Observatory on the site of the historical EMEP-GAW station of the JRC in Ispra to continue the assessment of the impact of European policies and international conventions on air pollution and climate forcing that started in 1985. Atmospheric measurements performed in parallel at other sites in the JRC premises were disrupted in July 2018. The variables we measure at the Atmospheric Observatory in Ispra include greenhouse gas concentrations (CO_2 , CH_4), radon (^{222}Rn) activity concentration, short-lived gaseous and particulate pollutant concentrations (CO , SO_2 , NO , NO_2 , O_3 , NMHCs, $\text{PM}_{2.5}$ and its main ionic and carbonaceous constituents), atmospheric particle micro-physical characteristics (number concentration and size distribution) and optical properties (light scattering and absorption in-situ, light scattering and extinction vertical profiles remotely), eutrophying and acidifying species (SO_4^{2-} , NO_3^- , NH_4^+) wet deposition. On-line measurements data are visible in real time at <http://abc-is.jrc.ec.europa.eu/>.

Vegetation \leftrightarrow atmosphere exchanges (CO_2 , O_3 , H_2O and heat) are measured at our Mediterranean Forest Flux Station of San Rossore, backed up by meteorological and pedological measurements.

All measurements are performed under international projects and programmes including ICOS (Integrated Carbon Observation System), ACTRIS (Aerosols, Clouds and Trace gases Research Infra-Structure), EMEP (co-operative Programme for Monitoring and Evaluation of the long range transmission of air pollutants in Europe) and GAW (Global Atmosphere Watch), each of which requires the use of standard methods and scales, and the participation in quality assurance activities. The JRC has a leading role in ACTRIS and EMEP regarding the quality assurance for carbonaceous aerosol measurements. Data obtained at the Atmospheric Observatory are submitted to international open data bases (www.europe-fluxdata.eu, fluxnet.ornl.gov, www.ingos-infrastructure.eu, [ACTRIS Data Portal](http://ACTRIS-Data-Portal)) and can be freely downloaded (partly in real-time) from these web sites. The data we produce are used in European wide assessments, for model inputs and validation, and for calibrating satellite airborne sensors. The European Commission Atmospheric Observatory 2018 report presents the data produced during the past year in the context of the previous years of measurements.

All the essential in-situ and remote sensing measurements scheduled for 2018 were regularly performed across the year, except for very short periods needed for moving, calibrating, and maintaining the equipment.

Greenhouse gas (GHG) measurements have been performed at the JRC Ispra site since October 2007. Minimum values of CH_4 , N_2O and SF_6 measured in Ispra under clean air conditions are close to marine background values, while CO_2 levels can even be lower than the Mace Head baseline due to the continental biospheric CO_2 sink. Deviations from baseline concentrations provide information about regional and larger scale European greenhouse gas sources. ICOS-

compliant GHG measurements from the Atmospheric Observatory 100 m high tower started in December 2016. The new GHG laboratory received the ICOS certificate on 30 November 2018

Atmospheric pollution has been characterised at the Ispra site 1986. In 2018, the annual mean concentrations of SO₂, NO₂ and CO were less than during the previous years, which confirm the general trend of improvement in these air quality indicators over the last 3 decades. The concentrations of anthropogenic volatile hydrocarbons like benzene and toluene also dropped down by a factor of ~2 compared to 20 years ago. In contrast, most O₃ exposure indicators did not improve in 2018 (in line with the trend observed since 2010), which can certainly not be explained only by the warm and sunny conditions occurring from spring to autumn this year. The concentration of PM_{2.5} mass and of most of its components (NO₃⁻, SO₄²⁻, NH₄⁺, POM and EC) significantly decreased in 2018 compared to 2017, and reached levels close to their historical minima. PM_{2.5} average chemical composition was dominated by carbonaceous species (POM: 44%, EC: 6%), followed by secondary inorganics (NH₄⁺: 8%, NO₃⁻: 12%, SO₄²⁻: 12%). As previously observed, there was a clear increase of NO₃⁻ contribution to PM_{2.5} when shifting from cleaner (3 < PM_{2.5} < 10 µg/m³) to more polluted periods (PM_{2.5} > 25 µg/m³) during both cold and warmer months. PM_{2.5} (from gravimetric analyses at 20% RH) annual mean mass concentration (14 µg/m³) was well below the EU annual limit value (25 µg/m³), and wintertime maxima stopped to increase in 2018. The long-term time series of PM concentrations still suggests a decreasing trend of - 1.0 µg m⁻³ yr⁻¹ over the last 3 decades. The increase in particle number concentration observed since 2014 (following a net decrease till 2011) also stopped and the annual average (7300 cm⁻³) was in 2018 less than during the 3 previous years. These trends are reflected in several other aerosol in-situ variables like the aerosol light scattering coefficient, and as a consequence, the aerosol single scattering albedo (0.80 in 2018) increases since 2014. The annual wet deposition fluxes of the main acidifying and eutrophying species NH₄⁺, NO₃⁻, and SO₄²⁻ (1.3, 2.7, and 1.3 g m⁻², respectively) was larger than in 2017 (probably due to the exceptional amount of rainfall), but was still 10 to 40% less than during the 2000's. Only 2 rain samples with pH<4.6 were collected in 2018 (historical low record). Rainwater acidity has indeed drastically dropped over the past 3 decades. The changes observed in the long-term trends of particulate and O₃ pollution would of course need to be confirmed over several more years and at other observatories to have a wider scientific and policy-relevant significance.

The atmosphere ↔ vegetation exchange measurements at our Mediterranean forest flux station of San Rossore show that the pine tree forest was a net sink for CO₂ in 2018 (370 gC/m² absorbed) but less than during previous years. The sequence of alternate wet and dry years since 2013 (when the measurement site was moved 600 m inland) allowed us to observe that the total annual precipitation amount is not a key factor for determining the annual carbon sequestration by this Mediterranean ecosystem.

1 Introduction

The mission of the European Commission Atmospheric Observatory (formerly called ABC-IS) is to measure changes in atmospheric variables to obtain data that are essential for the conception, development, implementation and monitoring of the impact of European policies and International conventions on air pollution and climate change. Measurements include greenhouse gas concentrations, forest ↔ atmosphere fluxes, and concentrations of pollutants in the gas phase, particulate matter and precipitations, as well as aerosol micro-physical and optical properties. Most measurements are performed at the JRC-Ispira site (Fig. 1), and some at the typical Mediterranean site of San Rossore site (Fig. 51). The scope of the Observatory is to establish real world interactions between air pollution, climate change and the biosphere, highlighting possible trade-offs and synergies between air pollution and climate change policies. Possible interactions include the role of pollutants in climate forcing, the impact of climate change and air pollution on CO₂ uptake by vegetation, the effect of biogenic emission on air pollution and climate forcing, etc...

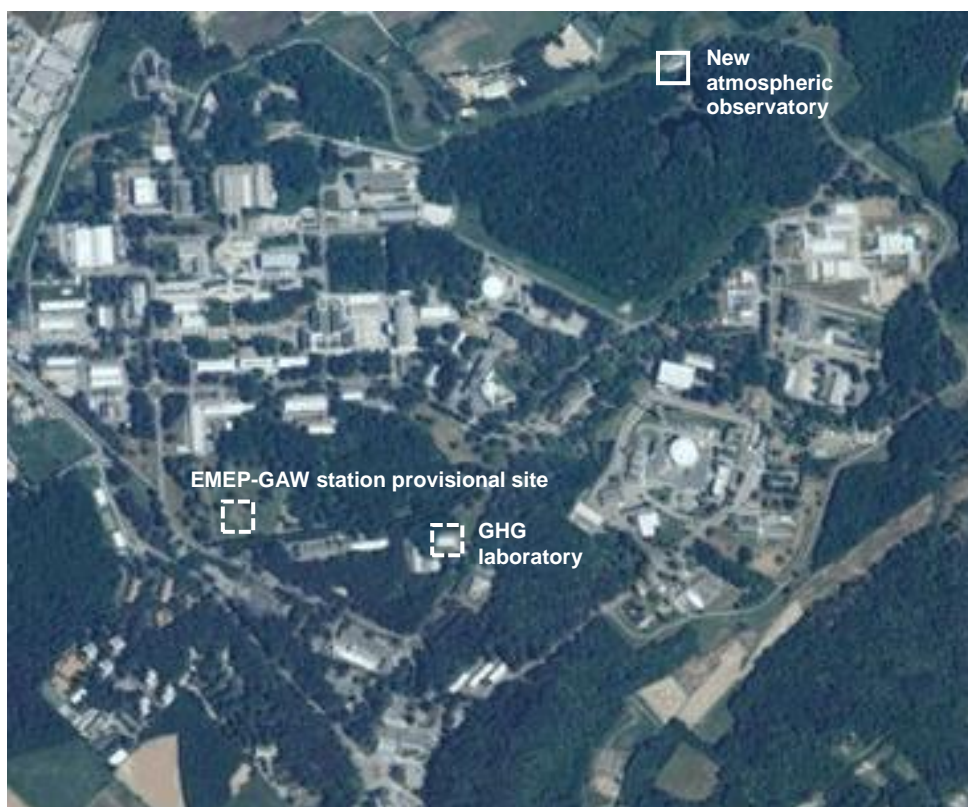


Fig. 1: The JRC-Ispira site and the location of the provisional EMEP-GAW site, the greenhouse gas laboratory, and the new atmospheric observatory, built on the spot of the historical EMEP-GAW station. The provisional site and the GHG laboratory are no longer in operation since July 2017 and 2018, respectively.

The Observatory is part of the spread European research infrastructures [ICOS](#) (Integrated Carbon Observation System) and [ACTRIS](#) (Aerosol, Clouds, and Trace Gases Research Infrastructure). Measurements are performed under international monitoring programs like [EMEP](#) (Co-operative program for monitoring and evaluation of the long range transmission of air pollutants in Europe of the UN-ECE *Convention on Long-Range Transboundary Air Pollution CLRTAP*) and [GAW](#) (the Global Atmosphere Watch program of the World Meteorological Organization). The Observatory infrastructure has also been used in competitive projects (e.g. [ACTRIS-2](#), [InGOS](#)).

The participation of the Observatory in international networks involves the organisation of inter-laboratory comparisons and the development of standard methods within the European Reference Laboratory for Air Pollution (ERLAP) of the JRC-Air and Climate Unit.

2 Quality management system

The European Commission Atmospheric Observatory is a research infrastructure of JRC's *Directorate for Energy, Transport and Climate*.

We achieved ISO 9001 certification in 2010 and re-certification in 2013, in 2016 and in 2018, all by external audits, which is also valid for the year 2018 (ISO 9001 is mainly about "project management"). In addition, internal audit of ISO 9001 was also performed successfully in 2018.

In addition to ISO 9001, JRC Ispra also achieved in 2010 the ISO 14001 certificate (ISO 14001 is mainly about "environmental issues"). In 2017, an external audit for re-certification took successfully place at JRC-Ispra (achieving again the ISO 14001 certificate). In 2018, an internal audit of ISO 14001 took successfully place at JRC-Ispra.

For information (the links below being accessible to JRC staff only), the "quality management system (QMS) for the Atmospheric Observatory" includes server space at the following links:

\\ies.jrc.it\H02\H02QMS_year_2018

<\\ies.jrc.it\H02\LargeFacilities\ABC-IS\>

<\\ies.jrc.it\H02\Laboratories>

<\\ies.jrc.it\H02\Laboratories\LifeCycleSheets>

where the following information can be found: standard operational procedures (SOP's); list of instruments; information about calibrations; standards used and maintenance; instrument lifecycle sheets and log-books; manuals for the instruments; etc. For additional specific details about QMS, for the year 2018 and the Atmospheric Observatory, see e.g. the file *2018_Instruments'_calibration_&_standards_&_maintenance.xls*, that can be found under \\ies.jrc.it\H02\LargeFacilities\ABC-IS\Quality_management.

More QMS information/details can also be found in the sections "Measurement techniques" in this report.

More general QMS information/documentations about how the AC Unit (C5) was run in 2018, the management of all of the projects within the Unit and the running of the Atmospheric Observatory can also be found at:

\\ies.jrc.it\h02\H02QMS_year_2018\1_Unit\QMS_info\QMS_documents_and_Unit

\\ies.jrc.it\h02\H02QMS_year_2019\1_Unit\QMS_info\QMS_documents_and_Unit

and especially in the seven C5 Unit QMS documents listed here (latest versions):

QMS_DIR_C_C5_Quality_Unit_Management_Manual_v14_0_in_ares.pdf

QMS_C5_MANPROJ_PROJ_Laboratory_Management_v13_0_in_ares.pdf

QMS_C5_MANPROJ_PROJ_Model_Management_v13_0_in_ares.pdf

QMS_C5_MANPROJ_PROJ_Informatics_Management_v13_0_in_ares.pdf

QMS_C5_MANPROJ_PROJ_Knowledge_Management_v13_0_in_ares.pdf

QMS_C5_MANPROJ_PROJ_Review_Verification_Validation_Approval_v9_0_in_ares.pdf

QMS_C5_MANPROJ_PROJ_Administration_Implementation_v8_0_in_ares.pdf

The latest versions of these documents are available at:

\\ies.jrc.it\H02\H02QMS_year_2019\1_UNIT\QMS_info\QMS_documents_and_Unit.



Fig. 2: The laboratories for atmospheric GHG measurements at Building 5 with 15m mast (left), and at the new Atmospheric Observatory with the 100m-tall tower (Building 77r).

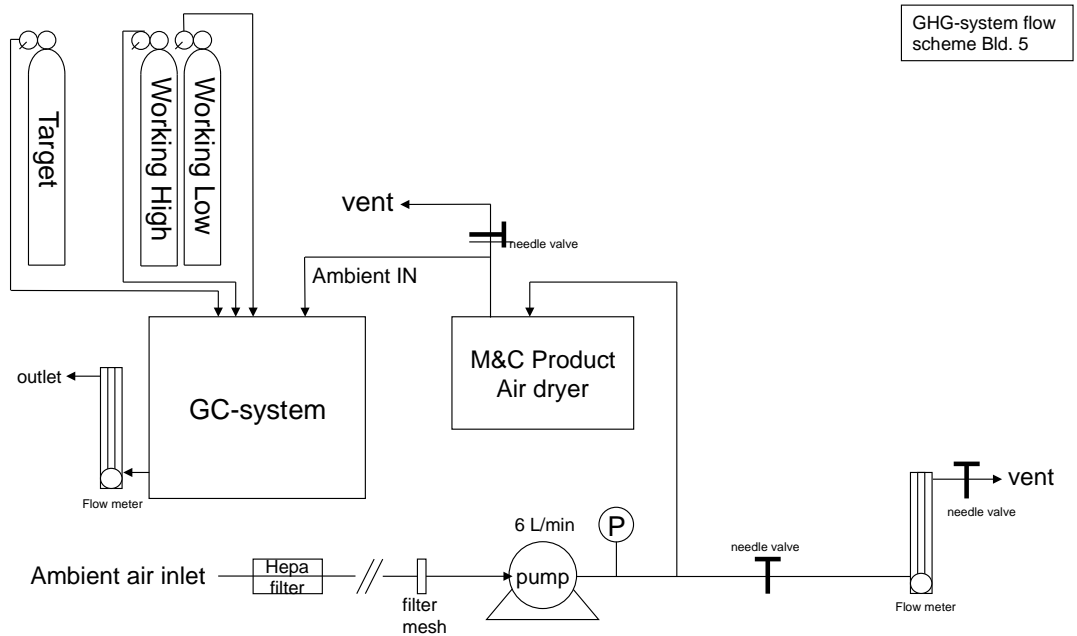


Fig. 3: Bd 5 GHG-system flow scheme

3 Greenhouse gas concentration monitoring at the JRC-Ispra site

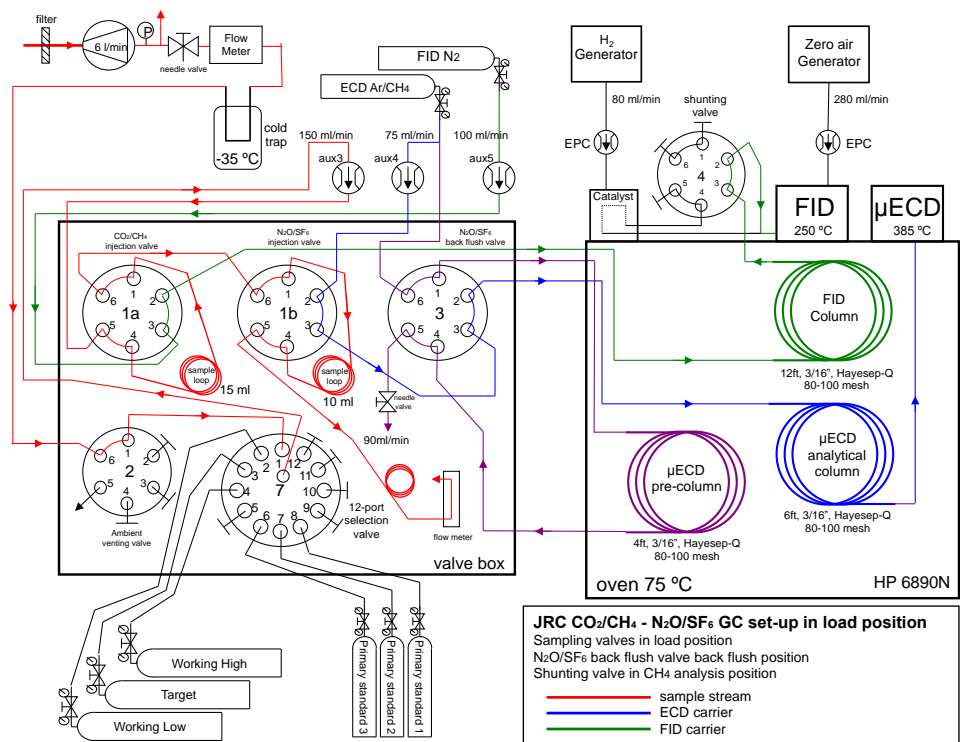
3.1 Location

The JRC monitoring station at Ispra is currently the only low altitude measurement site for greenhouse gases (GHGs) near the Po Valley. The unique location of the station at the South-Eastern border of Lake Maggiore in a semi-rural area at the North-Western edge of the Po Valley allows sampling of highly polluted air masses from the Po Valley during meteorological conditions with southerly flow, contrasted by situations with northerly winds bringing relatively clean air to the site. A high-resolution modelling study analysed in detail the sensitivity of the atmospheric concentrations at the monitoring station [*Bergamaschi and Brunner, 2015*]. The sensitivity usually shows a significant diurnal cycle, during night dominated by the area 40-60 km around the station, while daytime footprints are much larger, typically dominated by distances of more than 60 km. During summer daytime, the radius τ_{s50} (at which the cumulative surface sensitivity reaches 50% of the total sensitivity) is about 187 km on average. Furthermore, the diurnal cycle in local wind direction due to the regional mountain - lake/valley wind system leads to a significant diurnal cycle of the sensitivity (north-west vs. south-east), especially during summer time.

The main cities around the station are Varese, 20 km east of the station, Novara, 40 km south, Gallarate - Busto Arsizio, about 20 km southeast, and Milan, 60 km south-east of the station. The JRC GHG station has been setup in 2007 at Building 5 (Fig. 2) of the JRC Ispra site (45.807°N, 8.631°E, 223 m asl) and has been operated at that location continuously since end 2007 until June 2018 and has been discontinued afterwards. In 2016 a new station building inside the JRC premises (building 77r, 45.8147°N, 8.6360°E, 210 m asl) has been completed. The new station includes a 100m tower on top of the station building (Fig. 2), with platforms every 20 m. End of 2016 the new station has been equipped with a new GHG instrument and sampling system, with multiple sampling lines at 40, 60, and 100m. The new GHG station has been integrated into the European Integrated Carbon Observation System (ICOS) network (<https://www.icos-ri.eu/>) and received the ICOS certificate at the ICOS General Assembly on 30 November 2018.

3.2 Measurement programme

The GHG monitoring station in building 5 is in operation since October 2007, complementary to the JRC-Ispra EMEP-GAW station, which started in 1985 [*Putaud et al., 2018*], and to the flux measurement tower in the forest of San Rossore. GHG measurements at the new Atmospheric Observatory started end of November 2016. The new GHG station has successfully passed the second step of the official ICOS labelling procedure on 6 November 2018 and received the ICOS certificate at the ICOS General Assembly on 30 November 2018. The station is now an official "ICOS class-2" atmospheric station, which requires continuous CO₂, CH₄ and meteorological measurements, following strictly the ICOS guidelines (which includes rigorous standardization of instrumentation, sampling, calibration, QA/QC and centralized data processing).



Data File C:\CHEM32\1\DATA\ISPR\AMBIENT_20150807 2018-02-23 14-45-10\SIG11012.D
 Sample Name: AMBIENT

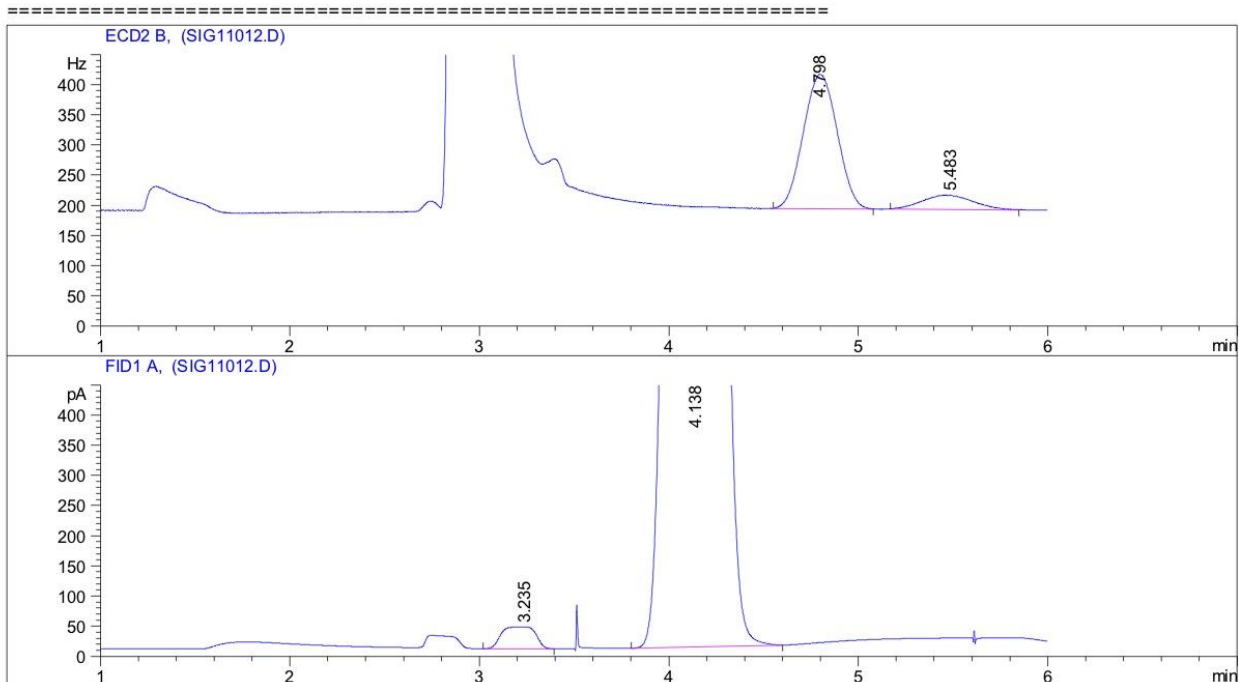


Fig. 4: The top panel shows a schematic of the GC-system set-up. Typical chromatograms are shown in the lower panels.

The GHG station in Building 5 has been run until end of June 2018 (providing overlapping measurements from both stations during an 18 month period) and has been discontinued afterwards.

3.3 Instrumentation in Building 5

3.3.1 Sampling

Air samples in Building 5 are collected on the top of a 15 m high mast via a 50 m ½" Teflon tube at a flow rate of ~6 L/min using a KNF membrane pump (KNF N811KT.18). The sampled air is filtered from aerosols by a Pall Hepa filter (model PN12144) positioned 10 m downstream of the inlet and dried cryogenically by a commercial system from M&C TechGroup (model EC30 FD) down to a water vapour content of <0.015%v before being directed to the analyzer. The remaining water vapour is equivalent to a maximum 'volumetric error' of <0.06 ppmv of CO₂ or <0.3 ppbv of CH₄ or <0.05 ppbv N₂O. A schematic overview of the sample flow set-up is shown in Fig. 3.

3.3.2 Analyses

3.3.2.1 Gas Chromatograph Agilent 6890N (S/N US10701038)

Continuous monitoring at 6 minute time resolution of CO₂, CH₄, N₂O, and SF₆ is performed with an Agilent 6890N gas chromatograph equipped with a Flame Ionization Detector (FID) and micro-Electron Capture Detector (μECD) using a set-up described by *Worthy et al.* (1998). The calibration strategy has been adopted from *Pepin et al.* (2001) and is based on a Working High (WH) and Working Low (WL) standard (namely bracketing standards), which are calibrated regularly using NOAA primary standards. The WH and WL are both measured 2 times per hour for calculating ambient mixing ratios, and a target (TG) sample is measured every 6 hours for quality control. The working standards and target cylinders are filled with synthetic air, while NOAA primary standards are filled with real air.

N₂O concentrations were also calculated using a second calibration strategy that is based on the one-point-reference method with a correction for non-linearity of μECD. The non-linear response of the μECD was estimated using NOAA primary standards and then it has been applied to the entire time series. This second method improves the quality of the time series when the bracketing standards do not cover the range for N₂O ambient concentrations (i.e. range too large or range that does not include ambient concentrations). GHG measurements are reported as dry air mole fractions (mixing ratios) using the WMO NOAA2004 scale for CH₄, the WMOX2007 for CO₂ and the NOAA2006A scale for N₂O and SF₆. We apply a suite of five NOAA tanks ranging from 369-523 ppm for CO₂, 1782-2397 ppb for CH₄, 318-341 ppb for N₂O, and 6.1-14.3 ppt for SF₆ as primary standards. The GC control and peak integration runs on *ChemStation* commercial software. Further processing of the raw data is based on custom built software developed in C language and named GC_6890N_Pro. A schematic of the GC-system set-up and typical chromatograms are shown in Fig. 4.

In March 2016 all the GC columns were replaced with new ones. The new columns have the same properties as the old columns. The nickel catalyst used to convert CO₂ to CH₄ was replaced during the same intervention.

The different types of uncertainties affecting the GC measurements have been estimated using the algorithms developed in the InGOS ("Integrated non-CO₂ Greenhouse gas Observing System") project (<http://www.ingos-infrastructure.eu/>). These uncertainties are defined as follows:

- 'Working standard repeatability' is calculated as the 24-hours centered moving, 1σ standard deviation of the bracketing standards (or reference standard in case of the one-point-reference method).
- 'Laboratory internal scale consistency uncertainty' (LISC) is the median of the difference between measured and assigned values of the target gas. The median is calculated for different time periods where GC settings were constant (including the used working standards and target gas).
- 'Monthly reproducibility' represents the values of the smoothed target residuals. Smoothing is performed with a centered running median with a window length of 30 days.

'Scale transfer and non-linearity uncertainty' is based on the uncertainty of the assigned working standard concentration and it accounts for the uncertainty introduced by scale transfer from NOAA standards to the working standards.

3.3.2.2 Radon analyser ANSTO (custom built)

²²²Radon activity concentrations in Bq m⁻³ have been monitored semi-continuously (30 minute time integration) applying an ANSTO dual-flow loop two-filter detector (Zahorowski et al., 2004) since October of 2008 till December 2016 [Putaud et al., 2018]. In December 2016 the detector has been moved to the new Atmospheric Observatory (Building 77r).

3.4 Instrumentation in the new Atmospheric Observatory (Bd 77R)

3.4.1 Air sampling

Air samples are collected at the different levels on the tower using ½" Synflex tubes at a flow rate of ~10 L min⁻¹. Each sampling line is provided with a KNF diaphragm pump (KNF N811 KTE or KNF N815 KTE) and three different particulate filters: a Pall Hepa Capsule Versapor filter at the inlet, and two filters with nominal pore sizes of 40 µm and 7 µm (model Swagelok SS-8TF-40 and SS-8TF-7, respectively).

A small air flow (around 0.2 L min⁻¹) is diverted from the main line toward the Picarro G2401 instrument using a dedicated vacuum pump (model Vacuubrand, MD1) located downstream to the analyser. As no liquid water has been observed in the sampling system since the beginning of measurements, the chiller used to dry the flow to a dew point of 5 °C (M&C Techground, model ECS) has been removed. This allowed to reduce the risk of leaks, because there are fewer connections in the sampling system, and to measure actual atmospheric water vapour concentration. A liquid water alarm is still in place to prevent any liquid water reaching the analyser.

3.4.2 Analyses

3.4.2.2 Cavity Ring-Down Spectrometer Picarro G2401 (S/N 2326-CFKADS2193)

The GHG laboratory at the new Atmospheric Observatory (Building 77r) is equipped with a Picarro G2401 Cavity Ring-Down Spectrometer that measures concentrations of CO₂, CH₄, CO and H₂O with a time resolution of 5 seconds. Concentrations are measured at three levels on the tower: 40 m, 60 m and 100 m above ground level (Fig. 5) following the ICOS technical specifications for class-2 atmospheric stations (<https://icos-atc.lscce.ipsl.fr/node/99/27248>). A rotary valve, model Valco Vici EMT2SD16MWE, allows to select the tower level to be analysed.

Table 1: Source signatures for $\delta^{13}\text{C}_s - \text{CO}_2$ of different sources (Vardag et.al, 2016).

Emission source	Used $\delta_{F,i}$ or δ_{bio} [‰]	Range of literature values $\delta_{F,i}$ or δ_{bio} [‰]
Fuel types		
Coal		-23 to -27
- Hard coal	-25	
- Brown coal	-27	
Peat	-28	-22 to -29
Oil	-29	-19 to -35
Gas		
- Natural gas	-46	-20 to -100
- Derived gas	-28	-26 to -29
Solid waste	-28	-20 to -30
Solid biomass	-27	-20 to -30
Bio liquid	-29	-20 to -30
Biogas	-11	0 to -16
Biosphere		
Photosynthesis	-23	-20 to -30
Respiration	-25	-20 to -30

Table 2: Source signatures for $\delta^{13}\text{C}_s - \text{CH}_4$ of different sources (Dlugokencky et.al, 2011).

Source	$\delta^{13}\text{CH}_4$ (‰)
Anthropogenic Energy	
Coal and industry	-35±3
Gas	
North Sea	-34±3
Siberia	-50±3
Enteric fermentation	
C_4 diet	-49±4
C_3 diet	-70±4
Rice agriculture	
Biomass burning	
C_4 vegetation	-17±3
C_3 vegetation	-26±3
Waste	
Landfills	-53±2
Domestic sewage	-57±3
Animal waste	-58±3
Natural	
Wetlands	
Swamps	-55±3
Bogs and tundra	-65±5
Termites	
Oceans	
Total	-52.9

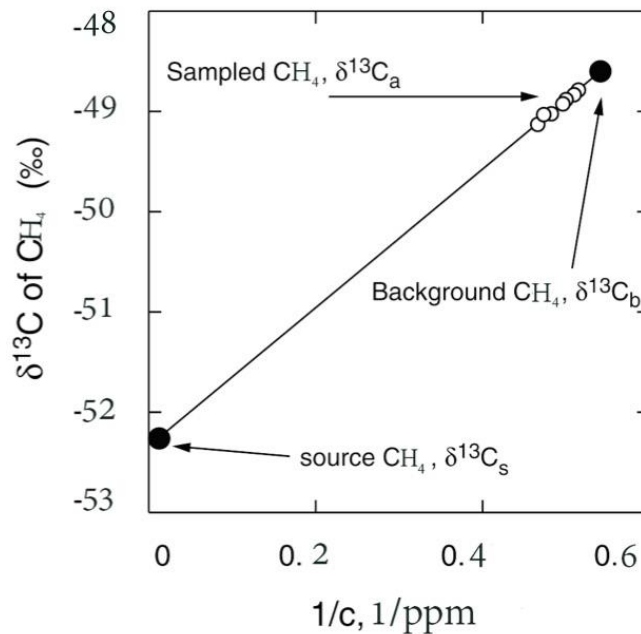


Fig. 6: Graphical illustration of the Keeling plot method applied to specific CH_4 measurements. $1/c$ represents the reciprocal of the atmospheric concentration of CH_4 for that specific observation [Pataki et.al, 2003].

The Picarro G2401 instrument directly controls this valve in order to sample the three levels sequentially within one hour. Measurement sequence is showed in Table 3.

Table 3: Measurement sequence of Picarro G2401. This cycle is repeated continuously every hour.

Sampling Level	Sampling duration (minutes)
100 m	15 (first 5 min rejected)
60 m	15 (first 5 min rejected)
100 m	15 (first 5 min rejected)
40 m	15 (first 5 min rejected)

The calibration strategy for the Picarro G2401 instrument is based on four gas tanks provided by ICOS CAL laboratory (<https://www.icos-cal.eu/>). Performances of the Picarro G2401 instrument have been evaluated using a short-term target (currently measured 3 times a day) and a long-term target (currently measured twice a month). Both targets were provided by ICOS-CAL laboratory.

3.4.2.3 Cavity ring-down Spectrometer G2201-i (S/N CFIDS2067)

In addition, the GHG laboratory performed measurements of ¹³C stable isotope in CO₂ and CH₄ using the isotopic analyzer Picarro G2201-i from April 2018 to February 2019 (instrument kindly provided by ICOS Atmosphere Thematic Centre). Air samples were collected at 40 m on the tower using ½" Synflex tubes at a flow rate of ~10 L min⁻¹ maintained by a KNF diaphragm pump (KNF N811 KT.18). Two particulate filters were placed on the sampling line: a Pall Hepa Capsule Versapor filter at the line inlet, and a 7 µm filter (model Swagelok SS-4FW-05) at the analyser inlet. A small air flow (around 0.2 L min⁻¹) is diverted from the main line toward the Picarro G2201-i instrument using a dedicated vacuum pump (model Vacuubrand, MD1) located downstream to the analyser.

The Picarro G2201-i analyzer can measure atmospheric concentration of ¹²CO₂ and ¹²CH₄ together with δ¹³C in CO₂ and δ¹³C in CH₄ by using Cavity Ring-Down Spectroscopy. δ¹³C is an isotopic signature, a measure of the ratio of stable isotopes ¹³C/¹²C, reported in parts per thousand (per mil, ‰). It is defined by the following equation:

$$\delta^{13}C = \left(\frac{\left(\frac{^{13}C}{^{12}C} \right)_{sample}}{\left(\frac{^{13}C}{^{12}C} \right)_{standard}} - 1 \right) * 1000$$

where the standard is an established reference material.

Analysis of stable isotopes is a widely used tool to identify sources (and sinks) of greenhouse gases, since different sources are characterized by different isotopic signatures (see Table 1 for CO₂ and Table 2 for CH₄). The isotopic signature of the sources can be derived from atmospheric measurements using the Keeling plot method [Keeling, 1958 and Keeling, 1961], which is based on mass conservation principle.

Atmospheric concentration (c_a) of a gas in a specific location is the combination of background concentration (c_b) and contributions from sources (c_s) nearby that location:

$$c_a = c_b + c_s$$

Considering conservation of mass,

$$\delta^{13}C_a c_a = \delta^{13}C_b c_b + \delta^{13}C_s c_s$$

and combining this equation with the previous one, we get

$$\delta^{13}C_a = c_b(\delta^{13}C_b - \delta^{13}C_s) \left(\frac{1}{c_a} \right) + \delta^{13}C_s$$

where $\delta^{13}C_s$ is the average value of all sources for the specific gas observed. It is also called the isotopic signature of sources affecting ambient concentration of the measured gas. The value of $\delta^{13}C_s$ is estimated as the intercept of the linear regression of $\delta^{13}C_a$ and $1/c_a$ values as illustrated in Fig. 6. Measured values of $\delta^{13}C_s$ can be compared with values published in the scientific literature for specific sources in order to identify the main sources affecting our measurements. Table 1 and Table 2 show literature value of $\delta^{13}C_s$ – CO₂ and $\delta^{13}C_s$ – CH₄ for different sources.

For the isotopic analysis, we used mainly night-time measurements, i.e. making use of the typical enrichment of GHGs in the nocturnal boundary layer. The geometric mean or standard major axis regression [Pataki *et al*, 2003] has been used to estimate $\delta^{13}C_s$ for methane and carbon dioxide.

3.4.2.4 Radon analyser ANSTO (custom built)

Measurements of ²²²Rn at the Atmospheric Observatory (Building 77r) started in December 2016, after the move of the ANSTO radon monitor from Building 5 to Building 77r. Air sample is taken from a separate inlet at 100 m above ground by using a blower (Becker, model SV 8.130/1-01). A 500 L decay tank is placed in the inlet line to allow for the decay of Thoron (²²⁰Rn with a half-life of 55.6 s) before reaching the ²²²Radon monitor. The ANSTO ²²²Radon monitor has been calibrated once a month using a commercial passive ²²⁶Radium source from Pylon Electronic Inc. (Canada) inside the calibration unit with an activity of 21.99 kBq, which corresponds to a ²²²Radon delivery rate of 2.77 Bq min⁻¹. The lower detection limit is 0.02 Bq m⁻³ for a 30% precision (relative counting error). The total measurement uncertainty is estimated to be <5% for ambient ²²²Radon activities at Ispra.

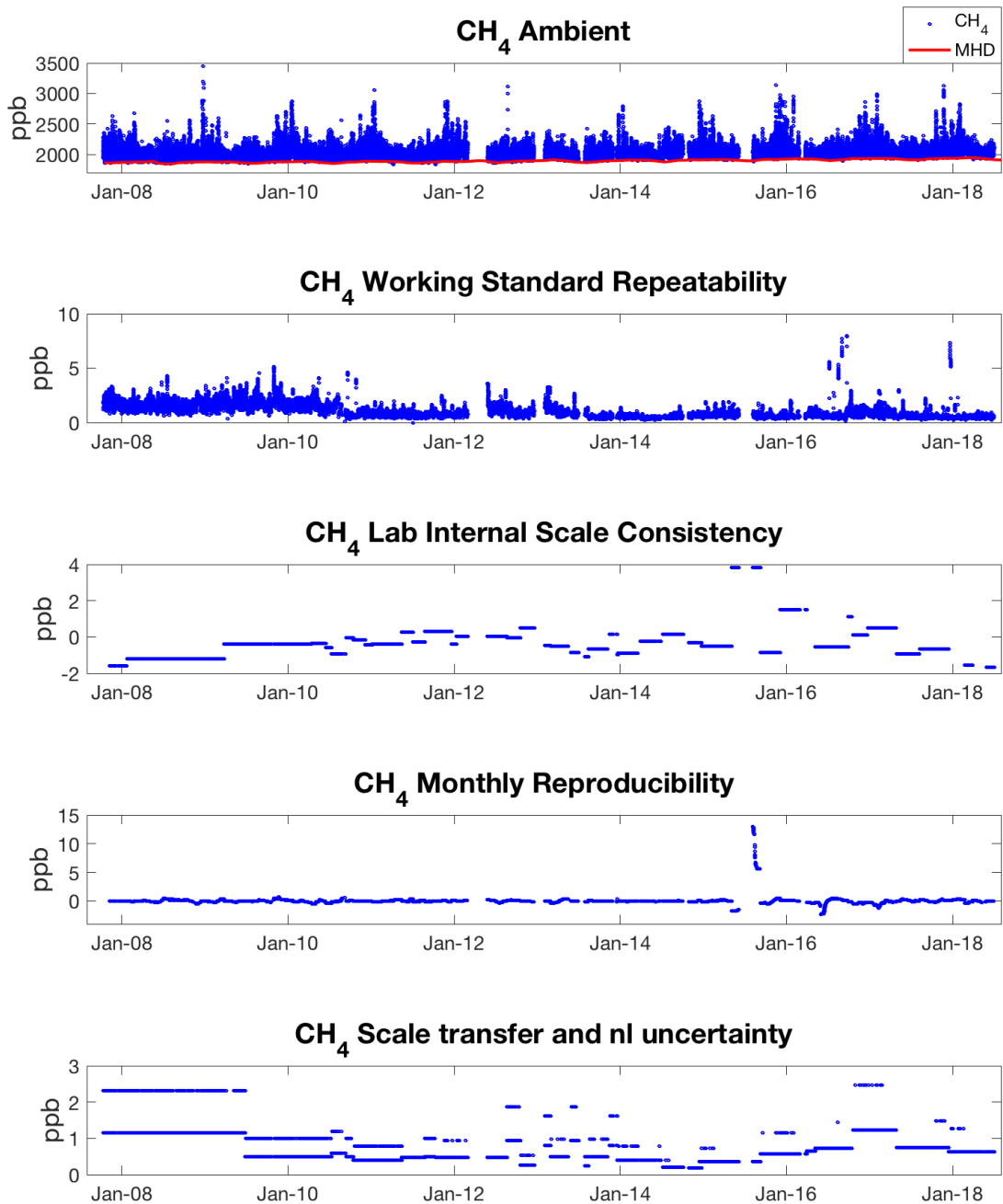


Fig. 7: Time series of continuous CH₄ ambient measurements at Ispra (Building 5) between October 2007 and July 2018 with associated uncertainties. CH₄ ambient concentrations are reported as hourly mean values of dry air mole fractions. Furthermore, monthly mean concentrations from the background station Mace Head (MHD) on the West coast of Ireland are also included (Mace Head data from Simon O'Doherty, University of Bristol).

3.5 Overview of measurement results

Fig. 7, 8, 9 and 10 give an overview of the GC GHG measurements in building 5 since the start of measurements in October 2007 until beginning of July 2018. These figures show also the uncertainties of the ambient concentrations; the 'scale transfer and non-linearity' uncertainty has been calculated only for CH₄ and N₂O. For N₂O and SF₆ only data since 15/09/2010 are shown. Before this date there was a dilution problem of the sample loop connected to the column of the μ ECD detector. The flushing of the sample loop during ambient measurement was not sufficient to remove completely the carrier gas used in the previous analysis. The N₂O data shown in Fig. 9 are calculated using the one-point-reference method (see above).

Measurements collected in building 5 are plotted together with the monthly mean baseline data from the Mace Head (Ireland) station to illustrate the Atlantic background mixing ratios. Minimum values of CH₄, N₂O and SF₆ measured at the JRC-Ispra site are close to the Mace Head baseline, while CO₂ mixing ratios can be lower than the Mace Head baseline due to the continental biospheric CO₂ sink.

During summer 2015 the GC has undergone a significant maintenance in which the jet of the FID detector, the multi-position rotary valve and the nickel catalyser were replaced. After the maintenance, the precision of CO₂ measurements was worse than before because of the continuous decrease in the efficiency of the new nickel catalyst used to convert the CO₂ into methane. This catalyser has been replaced in March 2016. Afterward, the precision of CO₂ measurements has returned to typical values observed before summer 2015.

During the period October 2016 – April 2017 precision of CH₄ measurements was worse than before because of the too large range covered by working standards cylinders. In particular the WH bracketing standard concentration was too high (3135 ppb) compared to ambient concentrations observed in Ispra.

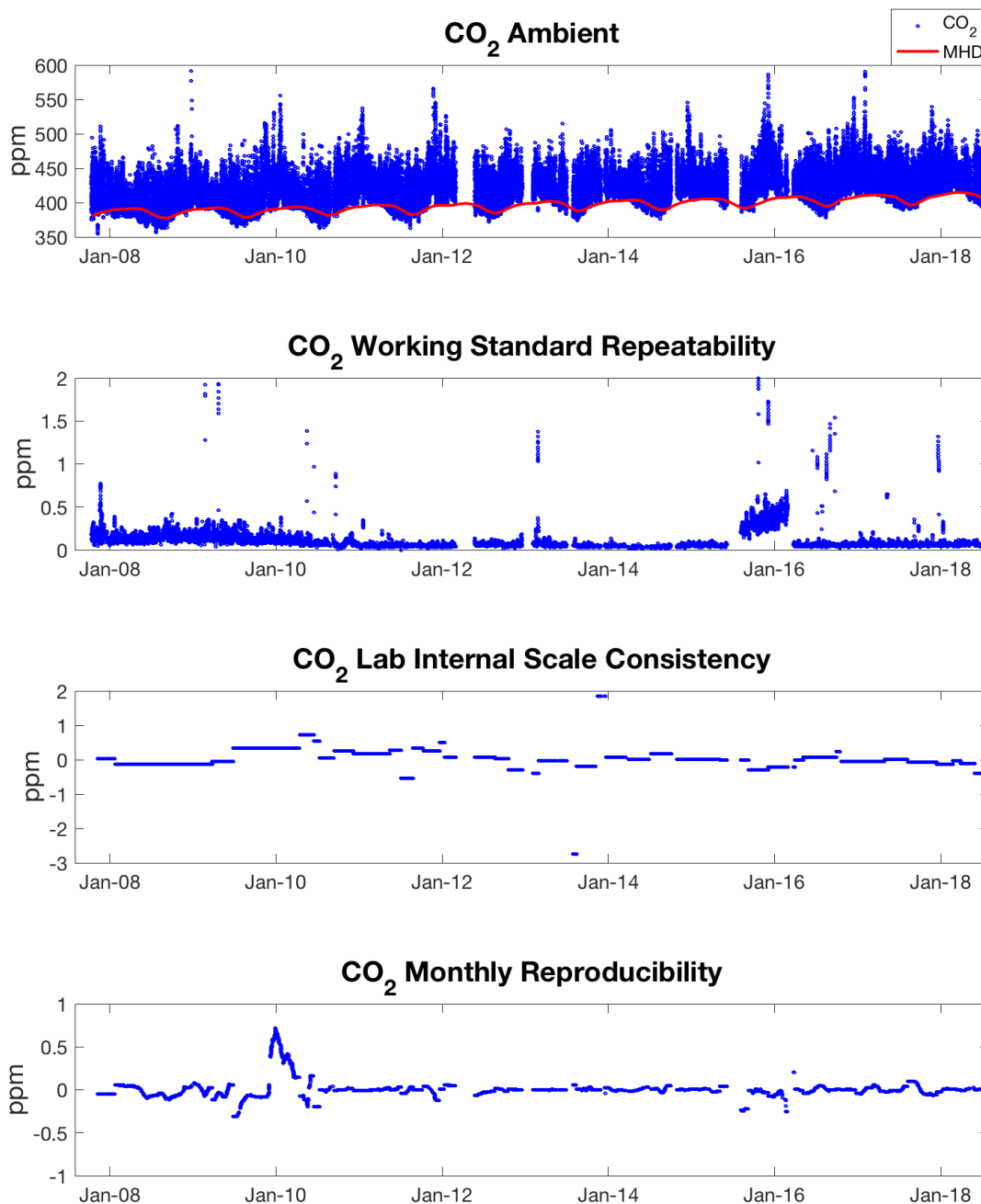


Fig. 8: Time series of continuous CO₂ ambient measurements at Ispra (Building 5) between October 2007 and July 2018 with associated uncertainties. CO₂ ambient concentrations are reported as hourly mean values of dry air mole fractions. Furthermore, flask measurements from the background station Mace Head (MHD) on the West coast of Ireland are also included (Dlugokencky, et al., 2017; Thoning, 2019).

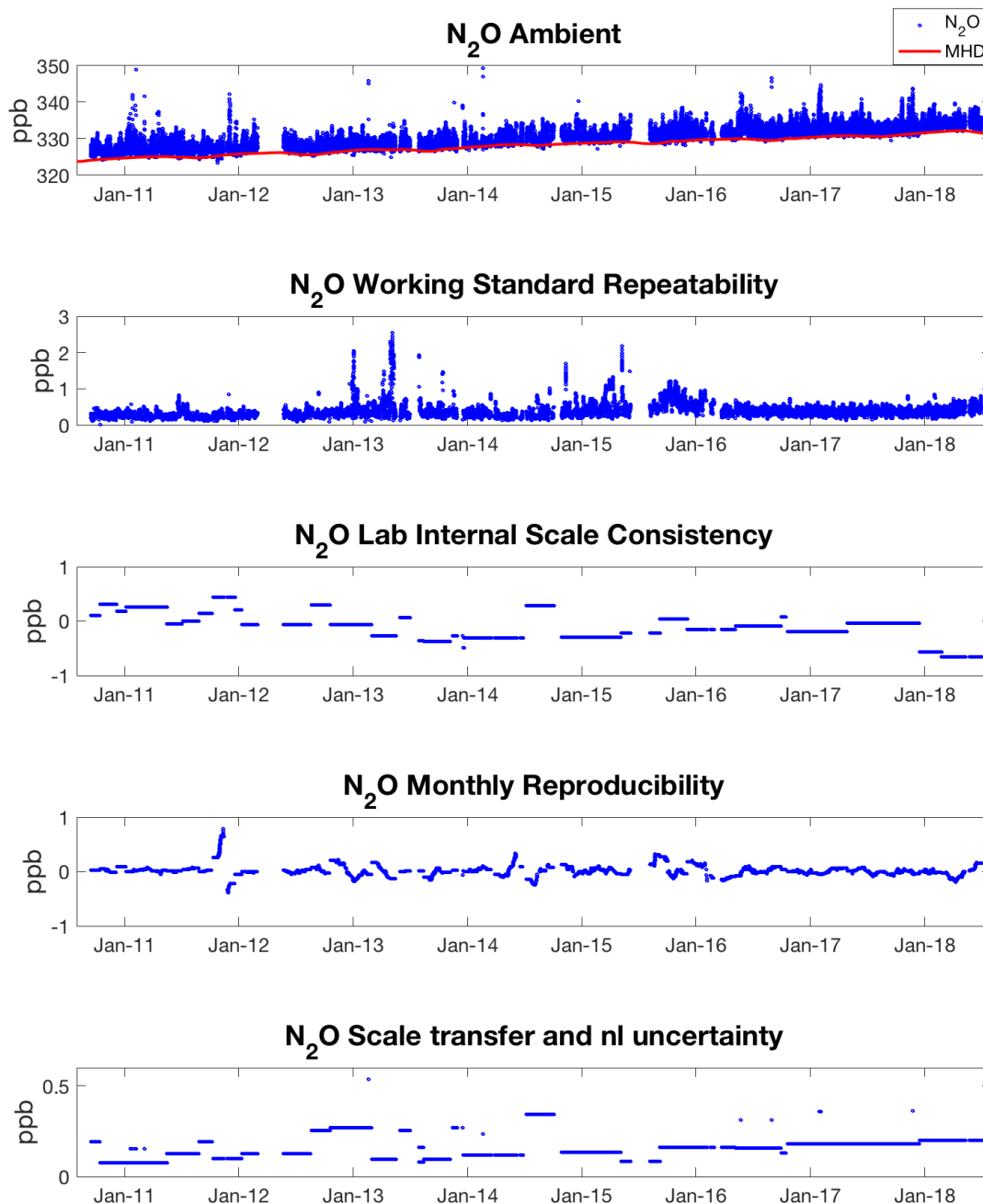


Fig. 9: Time series of continuous N₂O ambient measurements at Ispra (Building 5) between September 2010 and July 2018 with associated uncertainties. N₂O ambient concentrations are reported as hourly mean values of dry air mole fractions. Furthermore, monthly mean concentrations from the background station Mace Head (MHD) on the West coast of Ireland are also included (Mace Head data from Simon O'Doherty, University of Bristol).

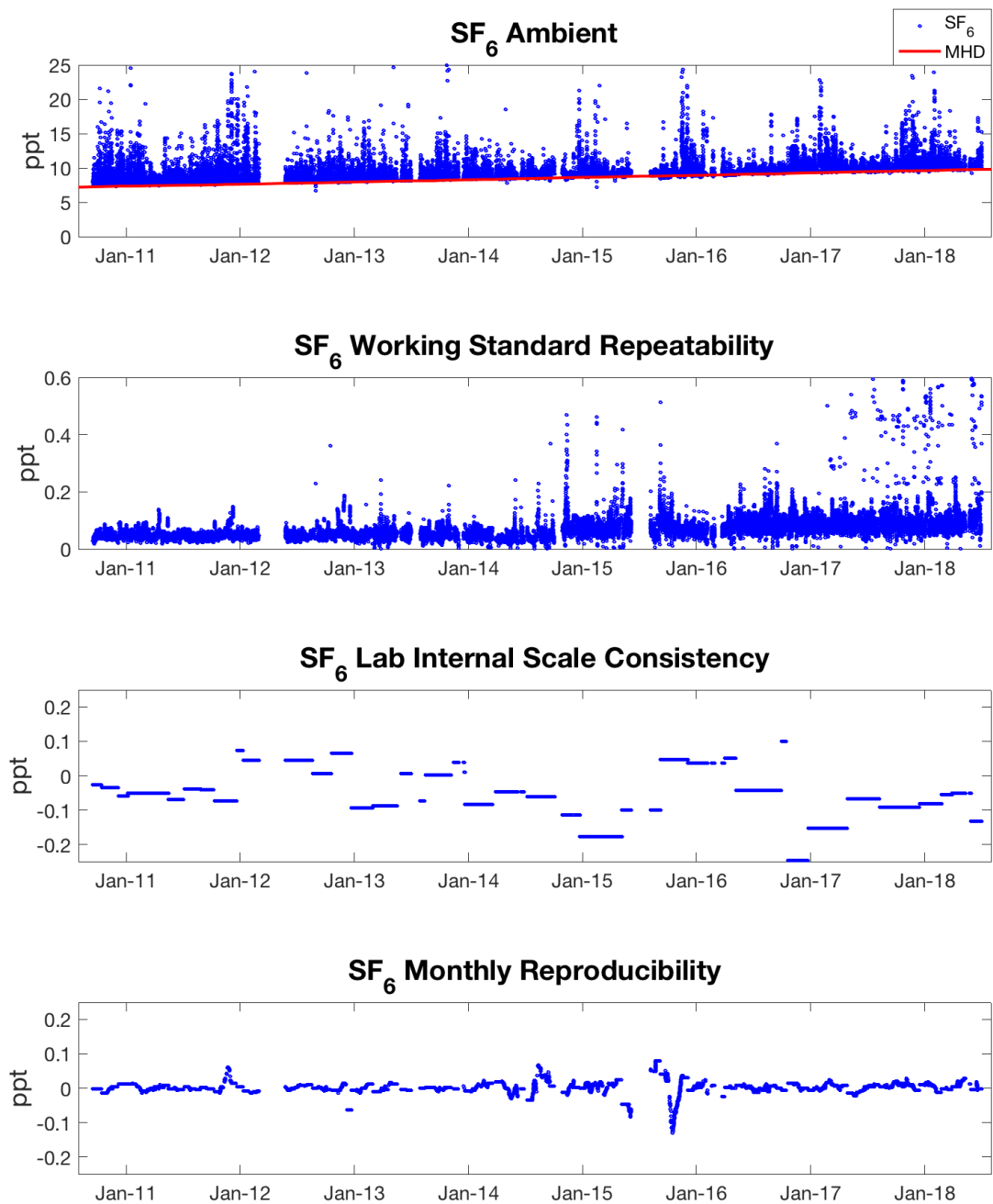


Fig. 10: Time series of continuous SF₆ ambient measurements at Ispra (Building 5) between September 2010 and July 2018 with associated uncertainties. SF₆ ambient concentrations are reported as hourly mean values of dry air mole fractions. Furthermore, monthly mean concentrations from the background station Mace Head (MHD) on the West coast of Ireland are also included (Mace Head data from Simon O'Doherty, University of Bristol).

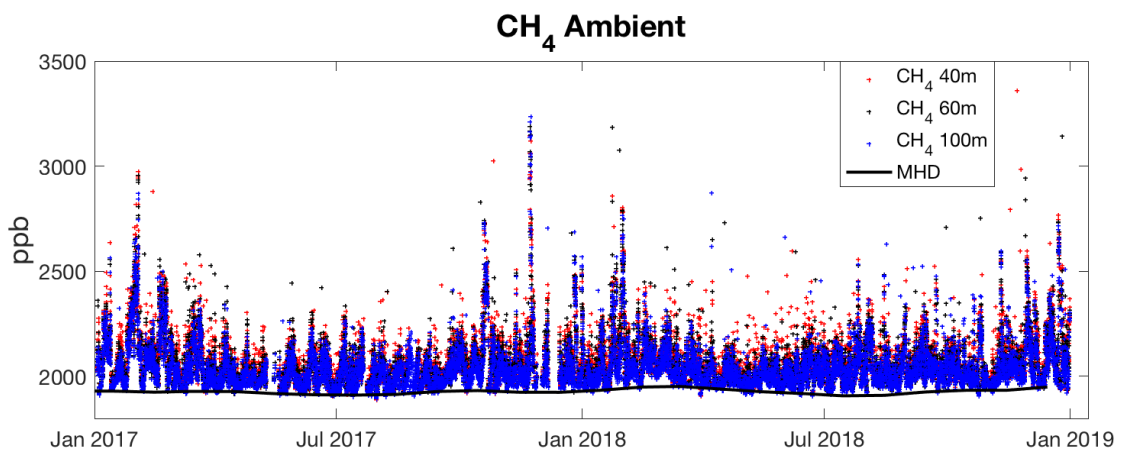
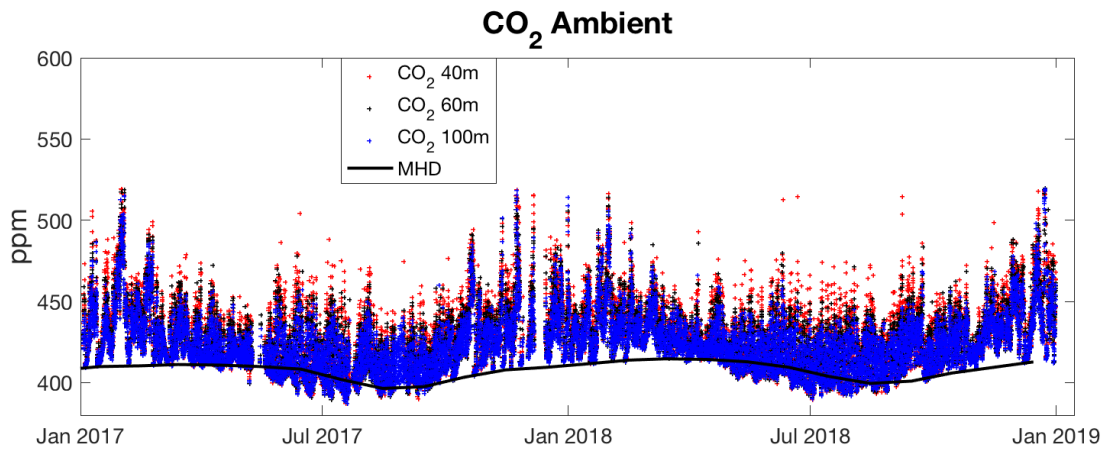


Fig. 11: Time series of continuous CH₄ and CO₂ ambient measurements at the Atmospheric Observatory (Bd 77r), sampled at three different heights (40m, 60m, 100m), between December 2016 and December 2018. Concentrations are reported as hourly mean values of dry air mole fractions. Furthermore, flask measurements from the background station Mace Head (MHD) on the West coast of Ireland are also included (Dlugokencky et al., 2019a; and Dlugokencky, 2019b).

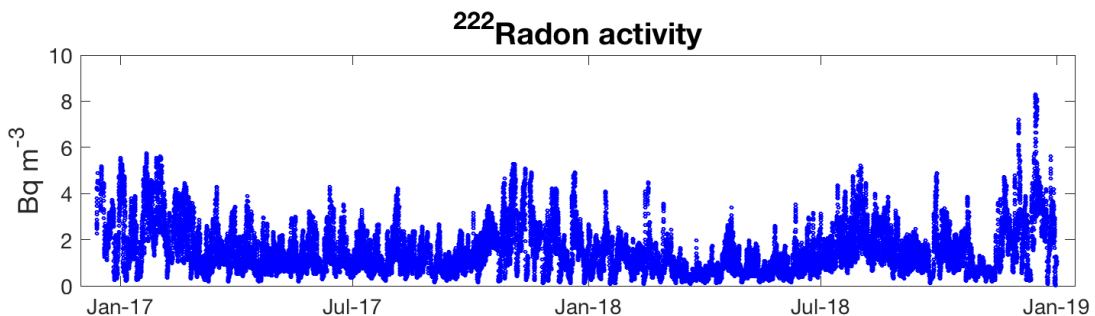


Fig. 12: ²²²Rn measurements at Atmospheric Observatory (building 77r). The figure shows the time series of hourly mean ²²²Rn activity, collected at 100m height, between December 2016 and December 2018.

Fig. 11 shows measurements of CH₄ and CO₂ at the Atmospheric Observatory (building 77r) at three different heights above ground (100m, 60m and 40m) between December 2016 and December 2018. Monthly mean baseline data from Mace Head station is also plotted to illustrate the Atlantic background mixing ratios.

Typically CH₄ and CO₂ concentrations show significant gradients during night (when the stable nocturnal boundary layers is developed), but are usually very close at all three heights during day (when tracers are usually well-mixed in the boundary layer).

Finally, Fig. 12 shows hourly mean ²²²Radon activity concentrations measured in building 77r at 100m level between December 2016 and December 2018. ²²²Radon activity concentrations show large diurnal and seasonal variations, mainly due to the diurnal and seasonal variations of the boundary layer height [*Koffi et al.*, 2016].

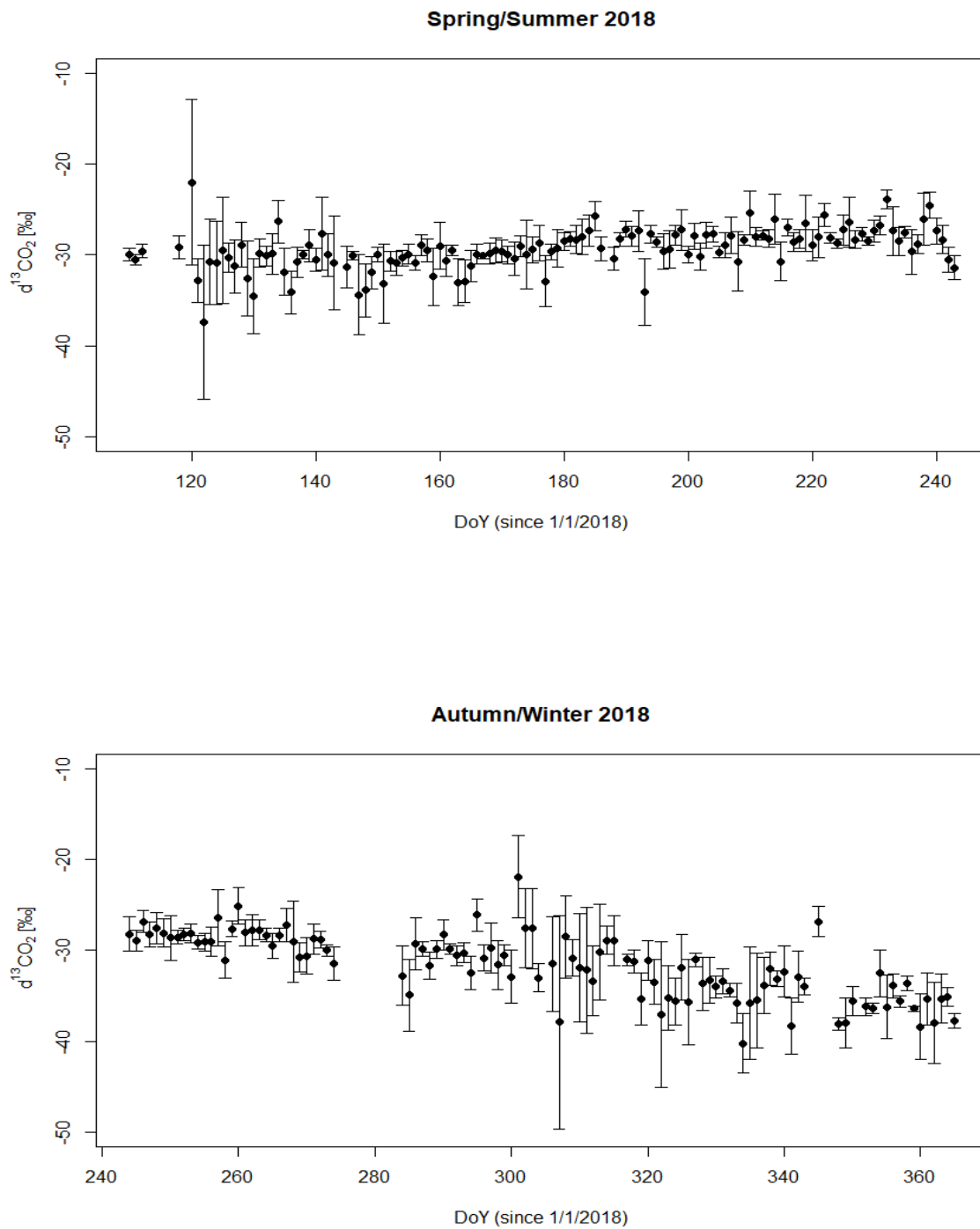


Fig. 13: Values of $\delta^{13}C_s$ for CO_2 estimated for the periods spring – summer 2018 (a) and autumn – winter 2018 (b). Each point represents the intercept of the geometric mean regression applied to the Keeling plot values for a specific night.

Fig. 13 shows values of isotopic signature of sources affecting night time CO₂ measurements during spring – summer and autumn – winter periods. During spring-summer period, the isotopic CO₂ signatures are quite stable with a slight increase (less negative values) during the summer months mainly related to the effect of the photosynthesis, while in autumn – winter period is evident a decreasing trend of isotopic signature values because of the reduction of photosynthesis and respiration at the ecosystem level and the increase of fossil fuel combustion. Fig. 14 shows values of isotopic signature of sources affecting night time CH₄ measurements during spring – summer and autumn – winter periods. Both in spring – summer and autumn – winter periods, no clear trend is observed. Most values range from -60 ‰ to -70 ‰, which is the typical isotopic signature of biogenic sources, such as methane produced by enteric fermentation of ruminants.

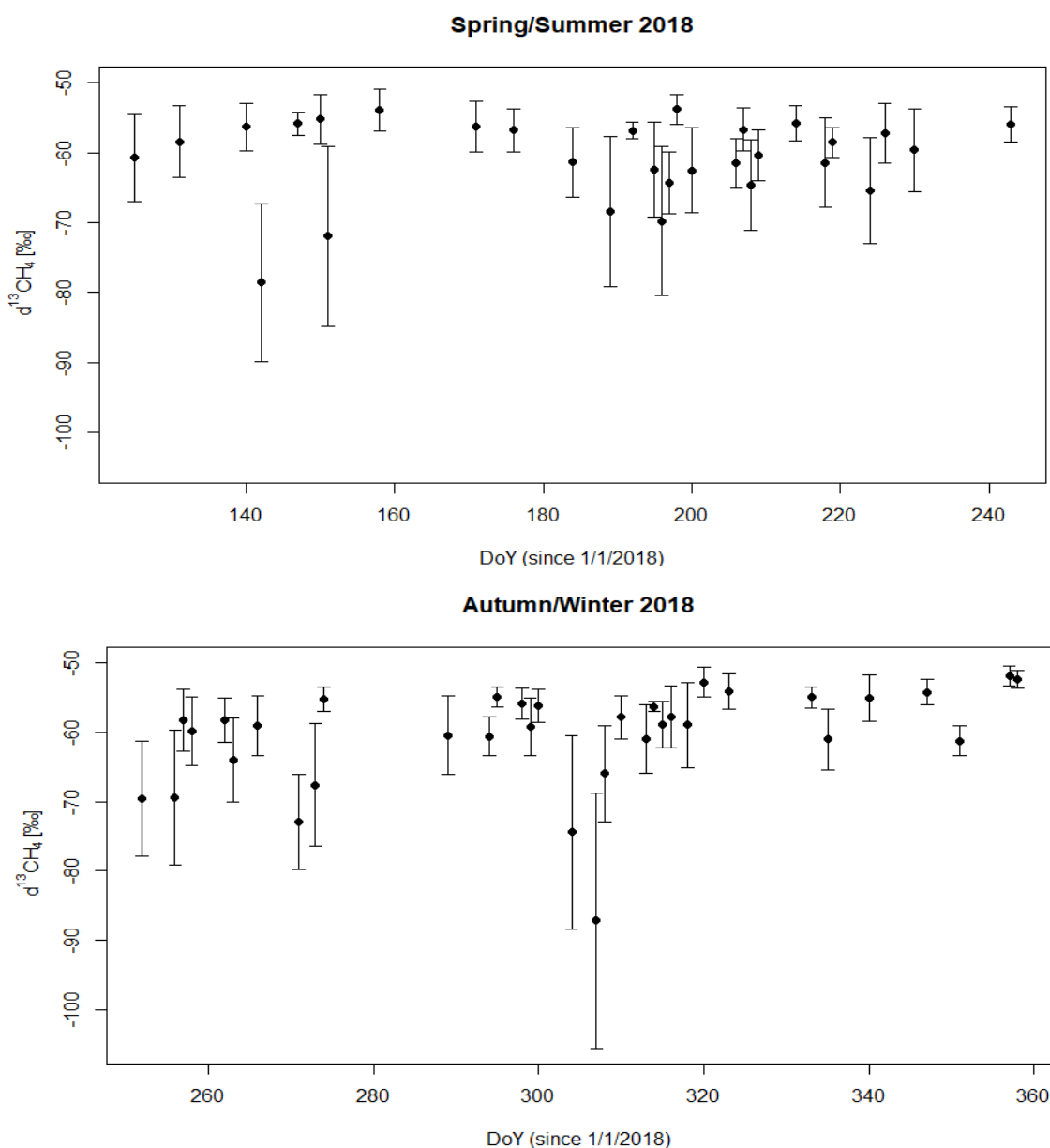


Fig. 14: Values of $\delta^{13}C_s$ for CH₄ estimated for the periods spring – summer 2018 (a) and autumn – winter 2018 (b). Each point represents the intercept of the geometric mean regression applied to the Keeling plot values for a specific night.

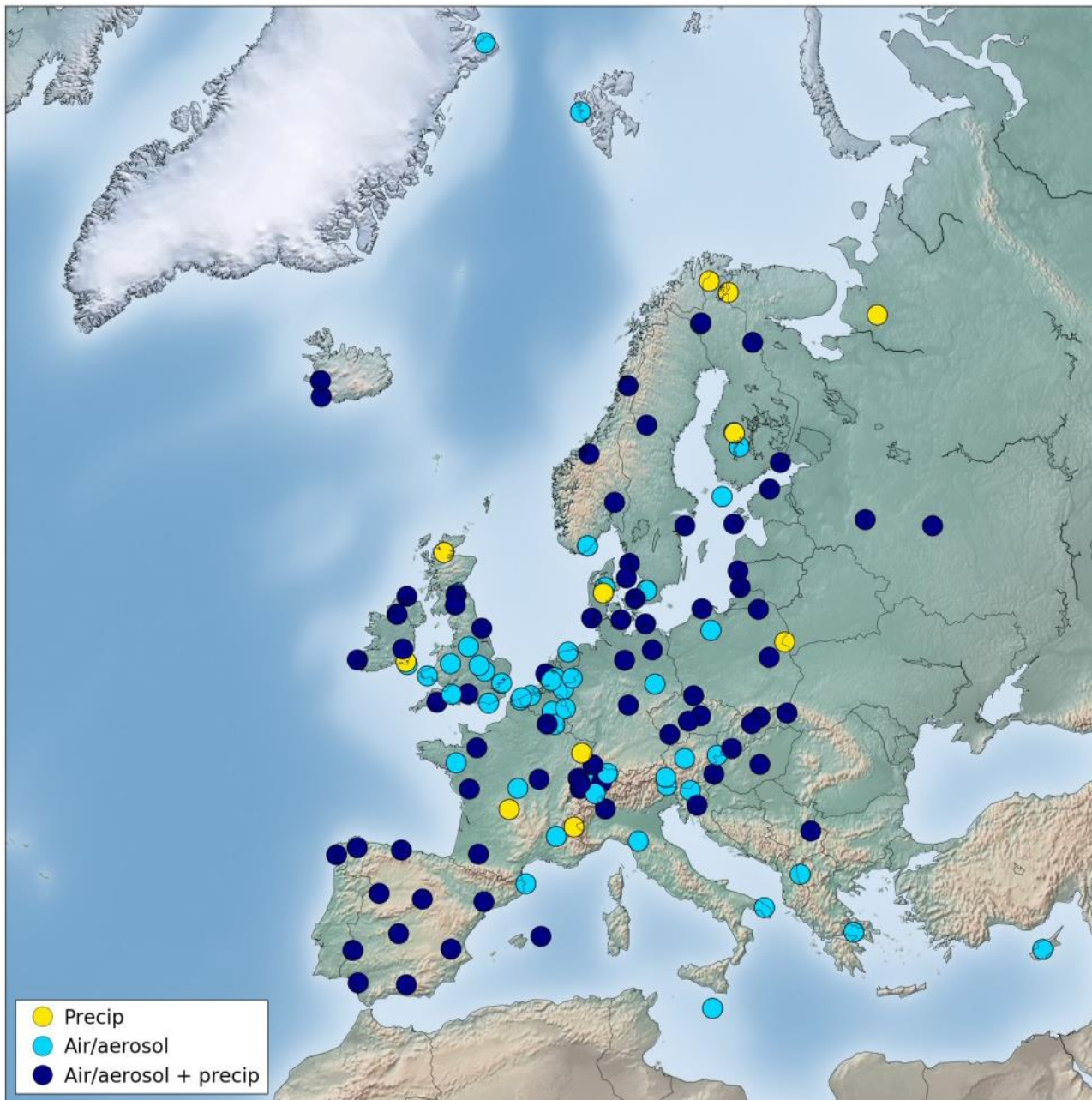


Fig. 15: most recent map of the EMEP stations across Europe (2017) taken from the 2019 Chemical co-ordinating Centre ([CCC](#)) [report](#).

4 Short-lived atmospheric species at the JRC-Ispra site

4.1 Introduction

4.1.1 Location

Air pollution has been monitored since 1985 at the atmospheric observatory (45°48.881'N, 8°38.165'E, 209 m a.s.l.) located by the Northern fence of the JRC-Ispra site (see Fig. 1), situated in a semi-rural area at the NW edge of the Po valley in Italy. From the end of March 2013 until June 2017, the measurement of short-lived atmospheric species (Table 2) was performed at a provisional site (45°48.438'N, 8°37.582'E, 217 m a.s.l.), due to the reconstruction of the laboratory at the historical site (Fig. 1). Gaseous pollutant measurements actually continued at the provisional site until December 2017 for comparison.

The nearest cities are Varese (20 km east), Novara (40 km south), Gallarate – Busto Arsizio (about 20 km south-east) and the Milan conurbation (60 km to the south-east). Busy roads and highways link these urban centres. Emissions of pollutants reported for the four industrial large point sources (CO₂ emissions > 1000 tons d⁻¹) located between 5 and 45 km NE to SE from Ispra also include 1.5 and 3 tons of CO per day, plus 2 tons of NO_x (as NO₂) per day for the 2 closest ones (**PRTR emissions**, 2017).

4.1.2 Underpinning programmes

4.1.2.1 The EMEP programme (<http://www.emep.int/>)

Currently, about 50 countries and the European Community have ratified the **CLRTAP**. Lists of participating institutions and monitoring stations (Fig. 15) can be found at: <http://www.nilu.no/projects/coc/network/index.html>

The set-up and running of the JRC-Ispra EMEP station resulted from a proposal of the Directorate General for Environment of the European Commission in Brussels, in agreement with the Joint Research Centre, following the Council Resolution **N° 81/462/EEC**, article 9, to support the implementation of the EMEP programme.

The JRC-Ispra station has operated on a regular basis in the extended EMEP measurement programme since November 1985. Data are transmitted yearly to the EMEP Chemical Co-ordinating Centre (CCC) for data control and statistical evaluation, and available from the EBAS data bank (Emep Database, <http://ebas.nilu.no/>).

4.1.2.2. The GAW programme (http://www.wmo.int/web/arep/gaw/gaw_home.html)

WMO's Global Atmosphere Watch (GAW) was established in 1989 with the scope of providing information on the physico-chemical composition of the atmosphere. These data provide a basis to improve our understanding of both atmospheric changes and atmosphere-biosphere interactions. GAW is one of WMO's most important contributions to the study of environmental issues, with about 80 countries participating in GAW's measurement programme. Since December 1999, the JRC-Ispra station is also part of the GAW coordinated network of regional stations. Data contributing to the GAW programme are also available via [EBAS](#).

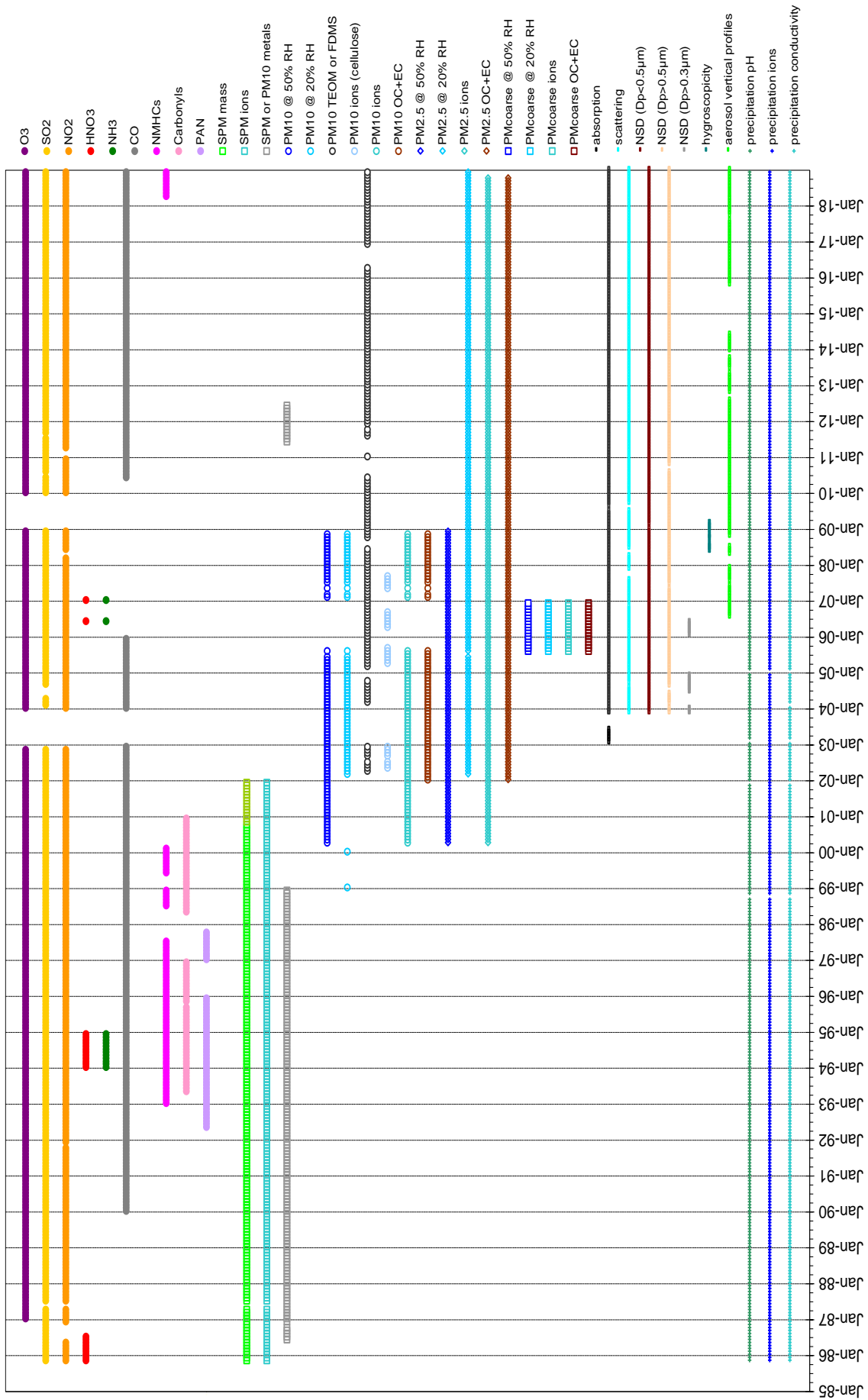


Fig. 16: Atmospheric short-lived species measurements performed at the JRC-Ispra atmospheric observatory since 1985.

4.1.2.3. The institutional programme (<http://ec.europa.eu/jrc/en/research-topic/air-quality>)

Since 2002, the measurement programme of the air pollution monitoring station of JRC-Ispra has gradually been focused on short-lived climate forcers such as tropospheric ozone and aerosols and their precursors (Fig. 16). Concretely, more sensitive gas monitors were introduced, as well as a set of new measurements providing aerosol characteristics that are linked to radiative forcing. The station contributes to the "Ex-post analysis of transport emission standards" as listed in the JRC institutional project work plan 2018 (Project AIR, WP IACA, Deliverable 8).

The atmospheric observatory is also used for research and development purposes. Regarding particulate organic and elemental carbon, techniques developed by the Air and Climate unit in Ispra have been implemented and validated by international atmospheric research networks ([EUSAAR](#), [ACTRIS](#)), recommended in the EMEP sampling and analytical procedure manual and adopted by the European Committee for Standardisation (CEN) as a standard method (EN16909:2017).

Currently, preliminary air pollution data obtained at the JRC-Ispra are visible and downloadable in real time from <http://abc-is.jrc.ec.europa.eu>. All validated data obtained at the JRC-Ispra station under the EMEP and the GAW programme, and other past and current international projects (EUSAAR, ACTRIS) can be retrieved from the EBAS database (<http://ebas.nilu.no/>), selecting "Ispra" as station of interest.

Additional information about the JRC-Ispra air monitoring station and other stations from the EMEP network can also be found in the following papers: Van Dingenen et al., 2004; Putaud et al., 2004; Mira-Salama et al., 2008; Putaud et al., 2010; Putaud et al., 2014; Cavalli et al., 2016.

Table 4: Variables related to short-lived pollutants and radiative forcers measured in 2018

METEOROLOGY	Pressure, temperature, humidity, wind, solar radiation
GAS PHASE	SO ₂ , NO ₂ , NO, NO _x , O ₃ , CO, NMHC
PARTICULATE PHASE	PM _{2.5} mass, Cl ⁻ , NO ₃ ⁻ , SO ₄ ²⁻ , C ₂ O ₄ ²⁻ , Na ⁺ , NH ₄ ⁺ , K ⁺ , Mg ²⁺ , Ca ²⁺ , OC, and EC contents Number size distribution (10 nm - 10 μm) Aerosol light absorption, scattering and back-scattering coefficients Altitude-resolved aerosol light back-scattering and extinction
WET DEPOSITION	Cl ⁻ , NO ₃ ⁻ , SO ₄ ²⁻ , C ₂ O ₄ ²⁻ , Na ⁺ , NH ₄ ⁺ , K ⁺ , Mg ²⁺ , Ca ²⁺ pH, conductivity

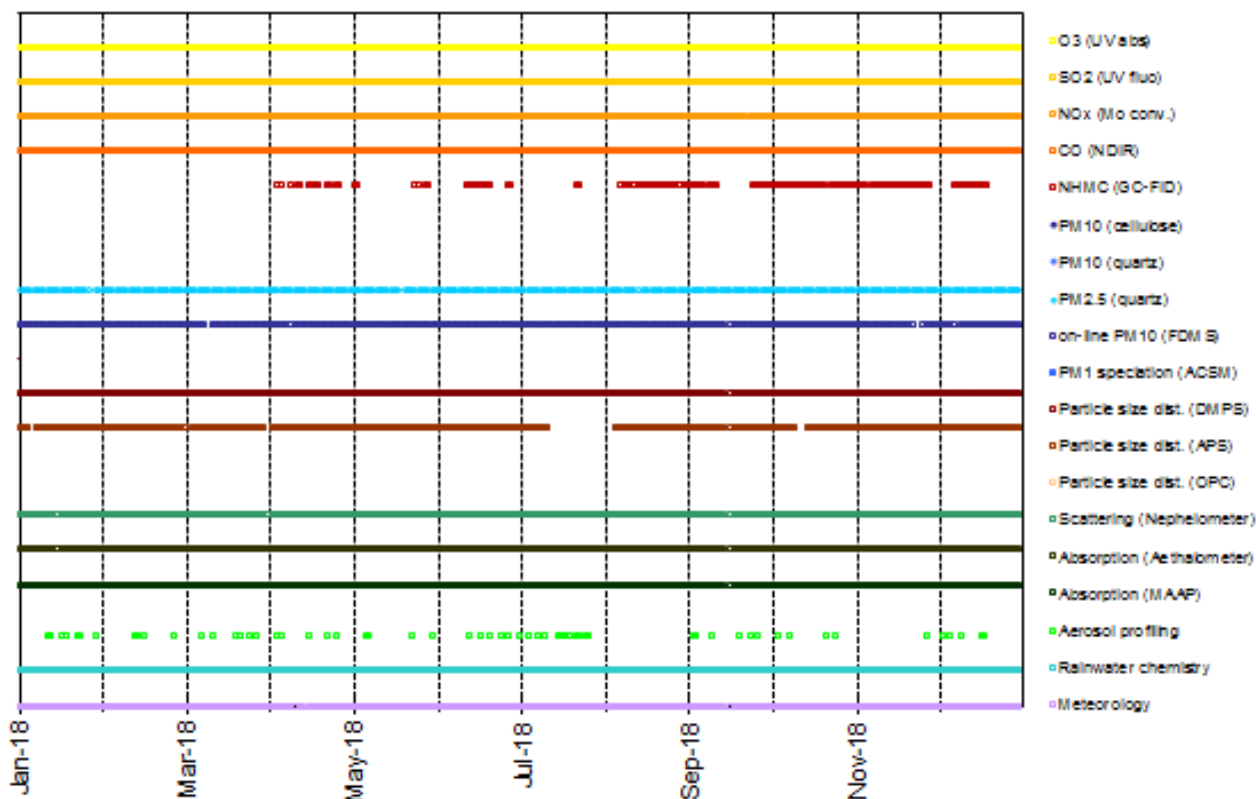


Fig. 17. Short-lived pollutants' data coverage for year 2018.

4.2 Measurements and data processing

4.2.1 Air pollutant and short-lived radiative forcer measurements at the Atmospheric Observatory in Ispra in 2018

Since 1985, the JRC-Ispra air monitoring station programme has evolved significantly (Fig. 16). Measurements were carried out at the Atmospheric Observatory from July 2017. The measurements performed in 2018 are listed in Table 4, and Fig. 17 shows the data coverage.

Meteorological variables were measured almost continuously, with three 1-2 day gaps filled by data taken from other weather stations from the JRC-Ispra site.

SO₂, O₃, NO_x and CO were measured quite continuously during the year 2018, with only 1 measurement day missing for NO_x (23 September) and 2 days for CO (17-18 December) due to repair works.

Daily particulate matter (PM_{2.5}) samples were collected and analysed for PM_{2.5} mass (at 20% RH), main ions, OC (organic carbon) and EC (elemental carbon), for the whole of 2018, with only 3 days missed (sampler malfunctioning).

On-line PM₁₀ measurements (FDMS-TEOM, Filter Dynamics Measurement System - Tapered Element Oscillating Microbalance) were carried out for the whole of 2018, except for 5 short (1-3 days) periods of time (total = 10 days) due to preventive and corrective maintenance.

Particle number size distributions (10 nm < D_p < 800 nm), light scattering and light absorption coefficients were measured almost continuously (99% coverage) in 2018. Super-micron particle number size distribution (90% data coverage) were stopped for the period 13 July – 15 August for maintenance at the manufacturers' and for 5 more 2-4 day slots distributed throughout the year for preventive and corrective maintenance.

The Raman LiDAR was operated according to the EARLINET schedule (Mon. at solar noon ±1 hr, at sunset -2,+3hr, Thu. at sunset -2,+3hr, and during the ESA satellite Calipso overpasses (± 1hr), weather and staff availability permitting).

Precipitation was collected throughout the year and analysed for pH, conductivity, and main ions (collected water volume permitting). Only a few major precipitation events were missed.

4.2.2 Measurement techniques

4.2.2.1 On-line monitoring

Meteorological Variables

Meteorological data and solar radiation were measured directly at the EMEP station with the instrumentation described below.

WXT510 (S/N: A1410010) at PS until 24.11.2018

WXT530 (S/N N2120878) at AO from 11.10.2018

Two WXT510 weather transmitters from [Vaisala](#) recorded the six weather variables temperature, pressure, relative humidity, precipitation and wind speed and direction from the top of a 10 m high mast at the provisional station, and from a 2 m mast on the terrace of the new observatory since Oct. 2017.

The wind data measurements utilise three equally spaced ultrasonic transducers that determine the wind speed and direction from the time it takes for ultrasound to travel from one transducer to the two others. Precipitation rate is measured with a piezoelectric sensor that detects the impact of individual raindrops and thus infers the accumulated rainfall. For the pressure, temperature and humidity measurements, separate sensors employing high precision RC oscillators are used.

Kipp and Zonen CMP 11 (S/N: 070289) at PS until 24.11.2018

Kipp and Zonen, SMP 11-V (S/N: 167256) at AO from 11.10.2018

To determine the total solar radiation, a [Kipp and Zonen](#) CMP11 Pyranometer has been installed in 2015, which measures the irradiance (in W/m²) on a plane surface from direct solar radiation and diffuse radiation incident from the hemisphere above the device. The CMP11 that was installed on the top of the container (3 m above ground) was replaced by the SMP11 on the terrace of the new observatory in Oct. 2017. The measurement principle is based on a thermal detector. The radiant energy is absorbed by a black disc and the heat generated flows through a thermal resistance to a heat sink. The temperature difference across the thermal resistance is then converted into a voltage and precisely measured. The CMP11 features a fast response time of 12 s, a small non stability of +/-0.5 % and a small non linearity of +/-0.2 %.

Gas Phase Air Pollutants

Sampling

SO₂, NO, NO_x, O₃ and CO were measured at the new atmospheric observatory (at the same place as the historical site) since June 2017, and only there since January 2018.

The sampling line at the Atmospheric Observatory (inlet about 5 m above ground) consists of an inlet made of a stainless steel cylindrical cap (to prevent rain and bugs to enter the line), outside a stainless steel tube (diameter = about 4 cm), inside a glass tube (d = about 2.7 cm) and a glass manifold with eight ¼" connectors. This inlet is flushed by an about 45 L min⁻¹ flow with a fan-coil (*measured 2 times per year with a gas-counter made by RITTER, sn. 11456, and online controlled with a flow sensor*). Each instrument samples from the tube with its own pump through a 0.25 inch Teflon line and a 5 µm pore size 47 mm diameter Teflon filter (to eliminate particles from the sampled air). See also Fig. 18.

In 2018, the gas phase monitors were verified daily by an automatic zero/span check and calibrated four times with traceable working standards (span gas cylinders and zero air) (see text for more details).

Sampling flow rates were as follows:

Compounds	Flow rates (L min ⁻¹)
SO ₂	0.5
NO, NO _x	1.0/1.3
O ₃	0.7
CO	1.5
NMHC	0.04

SO₂: UV Fluorescent SO₂ Analyser

Thermo 43iTLE (S/N 1503764211): 01.01.-11.07.2018

(S/N 1021443379): 11.07-31.12.2018.

At first, the air flow is scrubbed to eliminate aromatic hydrocarbons. The sample is then directed to a chamber where it is irradiated at 214 nm (UV), a wavelength where SO₂ molecules absorb. The fluorescence signal emitted by the excited SO₂ molecules going back to the ground state is filtered between 300 and 400 nm (specific of SO₂) and amplified by a photomultiplier tube. A microprocessor receives the electrical zero and fluorescence reaction intensity signals and calculates SO₂ based on a linear calibration curve.

Calibration was performed with a certified SO₂ standard at a known concentration in air (around 40 ppb, Air Liquide). Zero check was done, using a zero air gas cylinder from Air Liquide, Alphagaz 1, CnHm < 0.5 ppm).

The specificity of the trace level Thermo instrument (TEI 43i-TLE) is that it uses a pulsed lamp. The 43i-TLE's detection limit is 0.05 ppbv (about 0.13 µg m⁻³) over 300 second averaging time, according to the technical specifications.

For more details about the instruments, manuals are available at \\ies.jrc.it\H02\Largefacilities\ABC-IS\Quality_management\Manuals

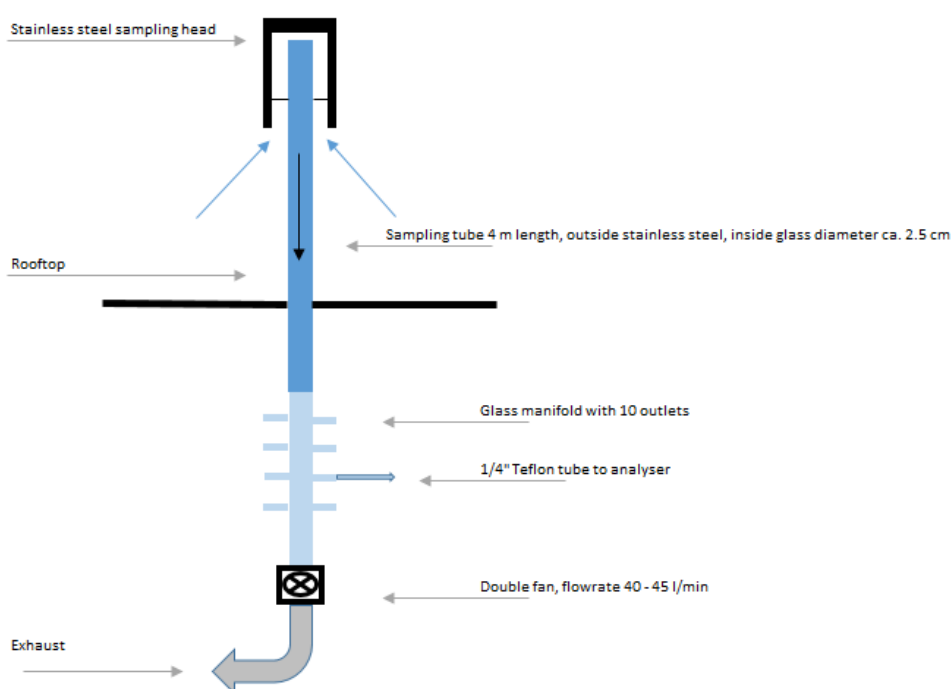


Fig. 18. Sampling inlet system for the gaseous air pollutant at the mobile lab. Inlet for the measurements is about 5 m above ground

NO + NO_x: Chemiluminescent Nitrogen Oxides Analyser (NO₂=NO_x-NO)

Thermo 42iTL (S/N 710820808): 01.01.-09.10.2018

(S/N 936539473): 09.010-31.12.2018.

This nitrogen oxide analyser is based on the principle that nitric oxide (NO) and ozone react to produce excited NO₂ molecules, which emit infrared photons when going back to lower energy states:



A stream of purified air (dried with a Nafion Dryer for 42iTL) passing through a silent discharge ozonator generates the ozone concentration needed for the chemiluminescent reaction. The specific luminescence signal intensity is therefore proportional to the NO concentration. A photomultiplier tube amplifies this signal.

NO₂ is detected as NO after reduction in a Mo converter heated at about 325 °C.

The ambient air sample is drawn into the analyser, flows through a capillary, and then to a valve, which routes the sample either straight to the reaction chamber (NO detection), or through the converter and then to the reaction chamber (NO_x detection). The calculated NO and NO_x concentrations are stored and used to calculate NO₂ concentrations (NO₂ = NO_x - NO), assuming that only NO₂ is reduced in the Mo converter. Detection limit was evaluated as 0.03 ppbv for NO and 0.05 ppbv for NO_x (own evaluations)

Calibration was performed using a zero air gas cylinder (Air Liquide, Alphagaz 1, CnHm<0.5 ppm) and a certified NO span gas (around 85 ppb NO in N₂, Air Liquide).

For more details about the instruments, the manuals are available on \\ies.jrc.it\H02\LargeFacilities\ABC-IS\Quality_management\Manuals

NO₂: Cavity attenuated shift down Nitrogen Dioxide Analyzer

Aerodyne CAPS NO₂ – S/N: 114002

The CAPS NO₂ monitor measures nitrogen dioxide directly by absorption of light at 450 nm. Thanks to the direct measurement it can be considered 'interferent - free' with a linear response. A laptop runs the analyser-software and stores the measured data. Once a day data are transferred automatically to UBIS4 database.

Baseline of the analyser is measured and corrected once per hour with NO₂ free air and the calibration is checked every three month.

Detection limit is <0.1 ppbv according to technical specifications.

O₃: UV Photometric Ambient Analyser

Thermo 49i (S/N 1150120006): 01.01.-11.07.2018

(S/N 1150120016): 11.07.-31.12.2018

The UV photometer determines ozone concentrations by measuring the absorption of O₃ molecules at a wavelength of 254 nm (UV light) in the absorption cell, followed by the use of Beer-Lambert law. The concentration of ozone is related to the magnitude of the absorption. The reference gas, generated by scrubbing ambient air, passes into one of the two absorption cells to establish a zero light intensity reading, I₀. Then the sample passes through the other absorption cell to establish a sample light intensity reading, I. This cycle is reproduced with inverted cells. The average ratio R=I/I₀ between 4 consecutive readings is directly related to the ozone concentration in the air sample through the Beer-Lambert law. Calibration is performed using externally generated zero air and external span gas. Zero air is produced by a JPAC zero air generator supplying a TEI 49C-PS transportable primary standard ozone calibrator (S/N 56676-309) to generate zero air and Span gas normally in the range 50 - 100 ppb. The TEI 49C-PS is calibrated/check by ERLAP (European Reference Laboratory of Air Pollution) against a NIST Standard Reference Photometer. A Nafion Dryer

system is connected to the O₃ instrument. Detection limit was evaluated as 0.3 ppbv (type approval)

For more details about the instruments, the manual is available on \\ies.jrc.it\H02\LargeFacilities\ABC-IS\Quality_management\Manuals

CO: Non-Dispersive Infrared Absorption CO Analyser

Horiba AMPA-370 (S/N: VM92B6WA) from 01.01.-25.09.2018 and from 19.-31.12.2018

(S/N WYHEOKSN) from 25.09.-17.12.2018.

In 2018, carbon monoxide (CO) has been continuously monitored using a commercial Horiba AMPA-370 CO monitor based on the principle of non-dispersive infrared absorption (NDIR). The Horiba APMA-370 uses solenoid valve cross flow modulation applying the same air for both the sample and the reference, instead of the conventional technique to apply an optical chopper to obtain modulation signals. With this method the reference air is generated by passing the sample air over a heated oxidation catalyst to selectively remove CO which is then directly compared to the signal of the untreated sample air at a 1 Hz frequency. The result is a very low zero-drift and stable signal over long periods of time.

To reduce the interference from water vapour to about 1% the sample air was dried to a constant low relative humidity level of around 30% applying a Nafion dryer (Permapure MD-070-24P) in the inlet stream. The detection limit of the Horiba AMPA-370 is ~30 ppbv for a one minute sampling interval.

Non-Methane Hydrocarbons (NMHC): Gas chromatograph with Flame Ionisation Detection

Agilent Technology, 7890A GC-System (S/N: CN13021054): 04.04.2018-19.12.2018

Markes International, Series 2 Unity Trap system (S/N: GB00U21897): idem

In 2018, about 30 NMHCs were measured using an on-line with GC-FID (Gas Chromatography – Flame Ionization Detection), associated with a cold 'trap' system and thermal desorption.

Outside ambient air is drawn through a glass inlet tube located about 6 m above ground level (building 77r) via a glass line with a 25 mm inner diameter and 4 m long borosilicate tube at a flow rate of about 3-5 m s⁻¹ (Fig. 18). The residence time for the sampled air in the tubes before arriving to the manifold is about 1 s. The air sample is drawn from the manifold to the sampling tube through a Nafion dryer at a flow rate of about 40 ml min⁻¹. The residence time in the Teflon line (about 2 m long and with an inner diameter of about 2 mm) is about 9 s. The Nafion dryer uses N₂ as a counter flow ("nominal" counter flow rate = 250 ml min⁻¹). NMHCs are collected below 0 °C in the cold trap (U-T503F-2S) suitable for ozone precursors from acetylene to trimethylbenzene and freons. The cold trap is desorbed to a sorbent tube (P/N U-T4WMT) containing three materials (Tenax TA backed by Carbograph 1TDTM backed by Carboxen 1000TM) each separated and supported by unsilanised glass wool plugs, optimised for focusing on compounds ranging from C₂ to C₂₄. This sorbent is normally stable for years, and should normally not be exchanged every year. Collected NMHCs are thermally desorbed at about 100 °C (using also a split tube) and injected through a heated valve to the GC. The sample tube and the cold trap then cool down and are purged with He at some ml min⁻¹ for about 10 min.

Desorbed NMHCs are carried to the splitter by the He carrier gas. The sample is injected in parallel in a polar column and a nonpolar column where NMHCs are separated. GC's thermal protocols starts at 30°C and terminates at about 100 °C within about 30 min. A flame ionizing detector (FID) is used to quantify the C atoms of each NMHC species. At the end of the analytical protocol, the oven temperature gets down to 30 °C after about 10 min.

The whole process (sampling + analyses) takes about 60 min. In 2018 measurements were usually performed for two 24 hr cycles per week (about one hour blank, 2 times one hour calibration, 24 times one hour outside air sampling and measurement, 2 times one hour calibration, about one hour blank).

NMHCs 2018 data are still undergoing ACTRIS-specific QA/QC procedures before being submitted to [EBAS](#).

For more details about the instruments, see the manual available from \\ies.jrc.it\H02\LargeFacilities\ABC-IS\Quality_management\Manuals

Atmospheric Particles

Sampling Conditions

Since 2008, all instruments for the physical characterisation of aerosols (Multi-Angle Absorption Photometer, Aethalometer, Nephelometer, Aerodynamic Particle Sizer, Differential Mobility Particle Sizer) sample isokinetically from an Aluminium inlet pipe (diameter = 15 cm, length of horizontal part ~280 cm and vertical part ~220 cm) described in Jensen et al., 2010. The Tapered Element Oscillating Micro-balances (FDMS-TEOMs) used their own inlet systems. The MAAP sampled from the main inlet through Nafion dryers at a flow rate of 480 L hr⁻¹ from Nov. 2016.

The size dependent particle losses along the pipe radius were determined by measuring the ambient aerosol size distribution with two DMPS at the sampling points P0 (close to the inlet) and P2 (close to the end of the pipe) for different radial positions relative to the tube centre (0, 40 and 52 mm) at P2 (Gruening et al., 2009). Data show a small loss of particles towards the rim of the tube can be observed, but it stays below 15 %. The bigger deviation for particles smaller than 20 nm is again a result of very small particle number concentrations in this diameter range and thus rather big counting errors.

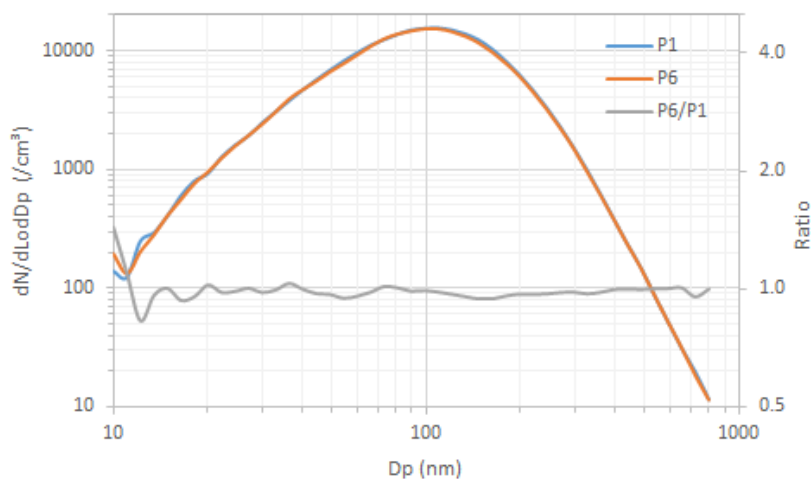


Fig. 19: particle number size distribution observed at both ends of the horizontal part of the aerosol manifold (Dec. 2017).

Particle losses in the aerosol manifold installed at the new Atmospheric Observatory have been measured using two inter-calibrated DMPS sampling close to the inlet (P1) and close to the outlet (P6) of the horizontal part of the manifold (Fig. 19). Losses at P6 compared to P1 were < 6% for all particle sizes between 20 and 800 nm (average 2%), which indicates no significant biases for the measurement of particle light absorption and scattering coefficient in the vicinity of P6.

PM₁₀ Mass Concentration: Tapered Element Oscillating Mass balance (TEOM), Series 1400a

Thermo FDMS – TEOM 1400 (233870012): 01 Jan. – 16 July 2018

Thermo TEOM - FDMS 1405-F (S/N 240401712): 17 July – 31 Dec. 2018.

The TEOM 1405 Monitor is composed of two major components, the sample inlet assembly and the TEOM 1405 unit. The user enters the system parameters into the TEOM 1405 unit using a color touchscreen that is located on the front of the unit. Additionally, the system is furnished with software for personal computers (a PC with an updated version of Windows XP is required to allow the user to download data and update instrument firmware. The instrument does not require a dedicated computer to function in the field.

The sensor unit contains a mass measurement hardware systems that monitors Particles that continuously accumulate on the system's exchangeable TEOM filters. By maintaining a flow rate of 3 l/min through the particulate channel, and measuring the total mass accumulated on the TEOM filter, the device can calculate the mass concentration in near realtime.

The Series 1400a TEOM® monitor incorporates an inertial balance patented by Rupprecht & Patashnick, now Thermo Scientific. It measures the mass collected on an exchangeable filter cartridge by monitoring the frequency changes of a tapered element. The sample flow passes through the filter, where particulate matter is collected, and then continues through the hollow tapered element on its way to an electronic flow control system and vacuum pump. As more mass collects on the exchangeable filter, the tube's natural frequency of oscillation decreases. A *direct* relationship exists between the tube's change in frequency and mass on the filter. The TEOM mass transducer does not require recalibration because it is designed and constructed from non-fatiguing materials. However, calibration was verified on Sept. 22nd, 2017 using a filter of known mass.

The instrument set-up includes a Sampling Equilibration System (SES) that allows a water strip-out without sample warm up by means of Nafion Dryers. In this way the air flow RH is reduced to < 30%, when TEOM® operates at 30°C only. The Filter Dynamic Measurement System (FDMS) is based on measuring changes of the TEOM filter mass when sampling alternatively ambient and filtered air. The changes in the TEOM filter mass while sampling filtered air is attributed to sampling (positive or negative) artefacts, and is used to correct changes in the TEOM filter mass observed while sampling ambient air.

Particle Number Size Distribution: Differential Mobility Particle Sizer (DMPS)

DMPS "B, DMA serial no. 158", CPC TSI 3772 (S/N 70847419 and 3772133103), neutraliser ⁸⁵Kr 10 mCi (2007)

The Differential Mobility Particle Sizer consists of a custom-made medium size (inner diameter 50 mm, outer diameter 67 mm and length 280 mm) Vienna-type Differential Mobility Analyser (DMA) and a Condensation Particle Counter (CPC), TSI 3772. Its setup follows the ACTRIS specifications for DMPS systems.

DMAs use the fact that electrically charged particles move in an electric field according to their electrical mobility. Electrical mobility depends mainly on particle size and electrical charge. Atmospheric particles are brought in the bipolar charge equilibrium in the bipolar diffusion charger (Eckert & Ziegler neutraliser with 370 MBq): a radioactive source (⁸⁵Kr) ionises the surrounding atmosphere into positive and negative ions. Particles carrying a high charge can discharge by capturing ions of opposite polarity. After a very short time, particles reach a charged equilibrium such that the aerosol carries the bipolar Fuchs-Boltzman charge distribution. A computer programme sets stepwise the voltage between the 2 DMA's electrodes (from 10 to 11500 V). Negatively charged particles are so selected according to their mobility. After a certain waiting time, the CPC measures the number concentration for each mobility bin. The result is a particle mobility distribution. The number size distribution is calculated from the mobility distribution by an inversion routine (from Stratmann and Wiedensohler, 1996) based on the bipolar charge distribution and the size dependent DMA transfer function. The DMPS measures aerosol particles in the range 10 - 800 nm with a 12 minute cycle. It records data using 45 size channels for high-resolution size information. This submicrometer particle sizer is capable of measuring concentrations in the range from 1 to

2.4×10^6 particles cm^{-3} . Instrumental parameters that are necessary for data evaluation such as flow rates, relative humidity, ambient pressure and temperature are measured and saved as well.

The CPC detection efficiency curve and the particle diffusion losses in the system are taken into account at the data processing stage.

Accessories include:

- FUG High voltage cassette power supplies Series HCN7E – 12500 Volts.
- Rotary vacuum pump vane-type (sampling aerosol at 1 LPM)
- Controlled blower (circulating dry sheath air)
- Nafion dryers for the sheath and sample air streams, implemented since October 2009.
- Mass flow meter and pressure transducer (to measure sheath air and sample flows).

Particle Number Size Distribution: Aerodynamic Particle Sizer (APS)

APS TSI 3321 (S/N 70535014 & S/N 1243)

The APS 3321 is a time-of-flight spectrometer that measures the velocity of particles in an accelerating air flow through a nozzle.

Ambient air is sampled at 1 L min^{-1} , sheath air (from the room) at 4 L min^{-1} . In the instrument, particles are confined to the centre-line of an accelerating flow by sheath air. They then pass through two broadly focused laser beams, scattering light as they do so. Side-scattered light is collected by an elliptical mirror that focuses the collected light onto a solid-state photodetector, which converts the light pulses to electrical pulses. By electronically timing the gap between the peaks of the pulses, the velocity can be calculated for each individual particle.

Velocity information is stored in 1024 time-of-flight bins. Using a polystyrene latex (PSL) sphere calibration, which is stored in non-volatile memory, the APS Model 3321 converts each time-of-flight measurement to an aerodynamic particle diameter. For convenience, this particle size is binned into 52 channels (on a logarithmic scale).

The particle range spanned by the APS is $0.5 - 20 \mu\text{m}$ in both aerodynamic size and light-scattering signal. Particles are also detected in the 0.3 to $0.5 \mu\text{m}$ range using light-scattering alone, and are binned together in one channel. The APS is also capable of storing correlated light-scattering-signal. $dN/d\text{Log}D_p$ data are averaged over 10 min.

Particle Scattering and Backscattering Coefficient

Integrating Nephelometer TSI 3563 (S/N 1081 & S/N 142101)

The integrating nephelometer is a high-sensitivity device capable of measuring the scattering properties of aerosol particles. The nephelometer measures the light scattered by the aerosol and then subtracts the light scattered by the walls of the measurement chamber, light scattered by the gas, and electronic noise inherent in the detectors.

Dried ambient air (since 18.11.2009) was sampled at 6.1 L min^{-1} from a PM10 inlet. .

The three-colour detection version of TSI nephelometer detects scattered light intensity at three wavelengths (450, 550, and 700 nm). Normally the scattered light is integrated over an angular range of $7-170^\circ$ from the forward direction, but with the addition of the backscatter shutter feature to the Nephelometer, this range can be adjusted to either $7-170^\circ$ or $90-170^\circ$ to give total scatter and backscatter signals. A 75 Watt quartz-halogen white lamp, with a built-in elliptical reflector, provides illumination for the aerosol. The reflector focuses the light onto one end of an optical pipe where the light is carried into the internal cavity of the instrument. The optical pipe is used to thermally isolate the lamp from the sensing volume. The output end of the optical light pipe is an opal glass diffuser that acts as a *quasi*-cosine (Lambertian) light source. Within the measuring volume, the first aperture on the detection side of the instrument limits the light integration to angles greater than 7° , measured from the horizontal at the opal glass. On the other side, a shadow plate

limits the light to angles less than 170°. The measurement volume is defined by the intersection of this light with a viewing volume cone defined by the second and fourth aperture plates on the detection side of the instrument. The fourth aperture plate incorporates a lens to collimate the light scattered by aerosol particles so that it can be split into separate wavelengths. The nephelometer uses a reference chopper to calibrate scattered signals. The chopper makes a full rotation 23 times per second. The chopper consists of three separate areas labelled "signal", "dark", and "calibrate". The "signal" section simply allows all light to pass through unaltered. The "dark" section is a very black background that blocks all light. This section provides a measurement of the photomultiplier tube (PMT) background noise. The third section is directly illuminated to provide a measure of lamp stability over time. To reduce the lamp intensity to a level that will not saturate the photomultiplier tubes, the "calibrate" section incorporates a neutral density filter that blocks approximately 99.9 % of the incident light. To subtract the light scattered by the gas portion of the aerosol, a high-efficiency particulate air (HEPA) filter is switched in line with the inlet for 300 s every day at 08:00 UTC. This allows compensation for changes in the background scattering of the nephelometer, and in gas composition that will affect Rayleigh scattering of air molecules with time. When the HEPA filter is not in line with the inlet, a small amount of filtered air leaks through the light trap to keep the apertures and light trap free of particles. A smaller HEPA filter allows a small amount of clean air to leak into the sensor end of the chamber between the lens and second aperture. This keeps the lens clean and confines the aerosol light scatter to the measurement volume only.

Nephelometer data are corrected for angular non-idealities and truncation errors according to Anderson and Ogren, 1998. A Nafion dryer has been installed (18.11.2009) at the inlet to measure light scattering by dry aerosols. Internal RH generally ranges from 0 to 40 % (average 24%, 97th percentile 40% in 2018). At 40% RH, aerosol scattering would be on average increased by about 15% compared to 0% RH in Ispra (Adam et al., 2012). However, aerosol particle scattering coefficients presented in this report are **not** corrected for RH effects, except when specified.

Particle Absorption Coefficient

Aethalometer Magee AE-31 ('A' S/N 408:0303 & 'B' S/N 740:0609)

The principle of the Aethalometer is to measure the attenuation of a beam of light transmitted through a filter, while the filter is continuously collecting an aerosol sample. Suction is provided by an internally-mounted pump. Attenuation measurements are made at successive regular intervals of a time-base period. The objectives of the Aethalometer hardware and software systems are as follows:

- (a) to collect the aerosol sample with as few losses as possible on a suitable filter material;
- (b) to measure the optical attenuation of the collected aerosol deposit as accurately as possible;
- (c) to calculate the rate of increase of the equivalent black carbon (EBC) component of the aerosol deposit and to interpret this as an EBC concentration in the air stream;
- (d) to display and record the data, and to perform necessary instrument control and diagnostic functions.

The optical attenuation of the aerosol deposit on the filter is measured by detecting the intensity of light transmitted through the spot on the filter. In the AE-31, light sources emitting at different wavelengths (370, 470, 520, 590, 660, 880 and 950 nm) are also installed in the source assembly. The light shines through the lucite aerosol inlet onto the aerosol deposit spot on the filter. The filter rests on a stainless steel mesh grid, through which the pumping suction is applied. Light penetrating the diffuse mat of filter fibres can also pass through the spaces in the support mesh. This light is then detected by a photodiode placed directly underneath the filter support mesh. As the EBC content of the aerosol spot increases, the amount of light detected by the photodiode will diminish.

For better accuracy, additional measurements are necessary: the amount of light penetrating the combination of filter and support mesh is relatively small, and a correction is needed for the 'dark response signal' of the overall system. This is the electronics' output when the

lamps are off: typically, it may be a fraction of a percent of the response when the lamps are on. To eliminate the effect of the dark response, we take 'zero' readings of the system response with the lamps turned off, and subtract this 'zero' level from the response when the lamps are on.

The other measurement necessary is a 'reference beam' measurement to correct for any small changes in the light intensity output of the source. This is achieved by a second photodiode placed under a different portion of the filter that is not collecting the aerosol, on the left-hand side where the fresh tape enters. This area is illuminated by the same lamps. If the light intensity output of the lamps changes slightly, the response of this detector is used to correct mathematically the 'sensing' signal. The reference signal is also corrected for the dark response 'zero' as described above.

The algorithm in the software (see below) can account for changes in the lamp intensity output by always using the ratio quantity [Sensing]/[Reference]. As the filter deposit accumulates EBC, this ratio will diminish.

In practice, the algorithm can account for lamp intensity fluctuations to first order, but we find a residual effect when operating at the highest sensitivities. To minimise this effect and to realise the full potential of the instrument, it is desirable for the lamps' light output intensity to remain as constant as possible from one cycle to the next, even though the lamps are turned on and off again. The software monitors the repeatability of the reference signal, and issues a warning message if the fluctuations are considered unacceptable. When operating properly, the system can achieve a reference beam repeatability of better than 1 part in 10000 from one cycle to the next. The electronics circuit board converts the optical signals directly from small photocurrents into digital data, and passes it to the computer for calculation. A mass flow meter monitors the sampled air flow rate. These data and the result of the EBC calculation are written to disk and displayed on the front panel of the instrument.

Aethalometer data can be corrected for the shadowing effect and for multiple-scattering in the filter to derive the aerosol absorption coefficient (Arnott et al., 2005) with a correction factor $C = 3.60, 3.65, \text{ and } 3.95$ for 470, 520 and 660 nm, respectively. Note that ACTRIS provisionally recommends the use of a constant conversion factor $C_0 = 3.5$ for all wavelengths (Mueller, 2015).

Multi Angle Absorption Photometer (S/N 4254515)

A Multi Angle Absorption Photometer (MAAP) model 5012 from [Thermo Scientific](#) was installed at the EMEP station in September 2008 and provides equivalent black carbon concentrations (EBC) and aerosol absorption (α) data at a nominal wavelength of 670 nm. Note that during a EUSAAR workshop (www.eusaar.org) in 2007 it has been observed that the operating wavelength of all MAAP instruments present at that workshop was 637 nm with a line width of 18 nm (full width at half maximum). The operating wavelength of this MAAP instrument has not been measured yet, therefore it is assumed to work at 670 nm as stated by the manufacturer.

The MAAP is based on the principle of aerosol-related light absorption and the corresponding atmospheric equivalent black carbon (EBC) mass concentration. Model 5012 uses a multi angle absorption photometer to analyse the modification of scattering and absorption in the forward and backward hemisphere of a glass-fibre filter caused by deposited particles. The internal data inversion algorithm of the instrument is based on a radiation transfer model and explicitly takes into account multiple scattering processes inside the deposited aerosol and between the aerosol layer and the filter matrix (see Petzold et al., 2004).

The sample air is drawn into the MAAP and aerosols are deposited onto the glass fibre filter tape. The filter tape accumulates the aerosol sample until a threshold value is reached, then the tape is automatically advanced. Inside the detection chamber (Fig. 20), a 670-nanometer light emitting diode is aimed towards the deposited aerosol and filter tape matrix. The light transmitted into the forward hemisphere and reflected into the back hemisphere is measured by a total of five photo-detectors. During sample accumulation, the light intensities at the different photo-detectors change compared to a clean filter spot. The reduction of light transmission, change in reflection intensities under different angles and the air sample volume are continuously measured during the sample period. With these data and using its

proprietary radiation transfer scheme, the MAAP calculates the equivalent black carbon concentration (EBC) as the instrument's measurement result.

Using the specific absorption cross section $\sigma_{BC} = 6.6 \text{ m}^2/\text{g}$ of equivalent black carbon at the operation wavelength of 670 nm, the aerosol absorption (α) at that wavelength can be readily calculated as:

$$\alpha = EBC \times \sigma_{BC} \quad \text{Eq. 1}$$

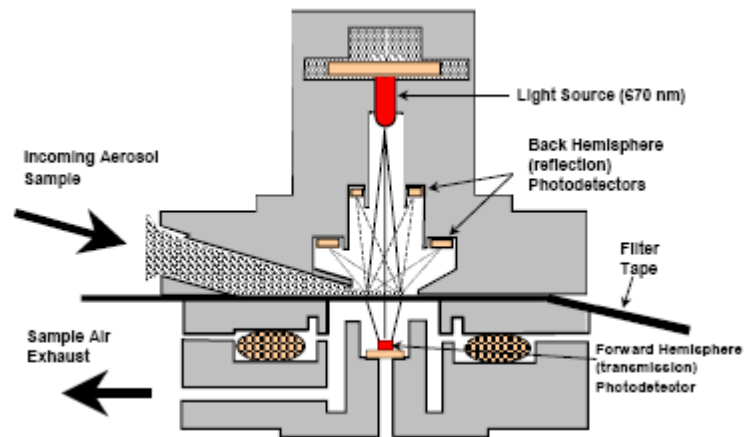


Fig. 20: MAAP detection chamber (sketch from the manual of the instrument).

Range-Resolved Aerosol Light Backscattering and Extinction

[Raymetrics Aerosol Raman Lidar \(S/N 400-1-12, QUANTEL Brilliant B Laser and cooler S/N 120059004 and S/N 120034401, LICEL Transient Recorder & Hi Voltage Supply S/N BS3245 and BS3245b, industrial PC S/N TPL-1571H-D3AE\)](#)

LiDAR measurements are based on the time-resolved detection of the backscattered signal of a short laser pulse that is sent to the atmosphere (for an introduction see Weitkamp, 2005). Using the speed of light, time is converted to the altitude where the backscattering takes place. Using the particle-free range of the atmosphere for calibration (where Rayleigh scattering from the air molecules is known), aerosol backscattering and extinction coefficients as well as aerosol optical thickness can be derived using the LiDAR equation. The received power P of the detector is therein given as a function of distance and wavelength by Eq. 2:

$$P(R, \lambda) = P_0 \frac{c\tau}{2} A \eta \frac{O(R)}{R^2} \beta(R, \lambda) \exp\left(-2 \int_0^R \alpha(r, \lambda) dr\right)$$

Eq. 2: P_0 : Power of the laser pulse, c : speed of light, τ : laser pulse length, A : area of the telescope, η : system efficiency, R : distance, O : overlap function (between laser beam and receiving optics field of view), λ : wavelength, β : backscatter coefficient, α : absorption coefficient

The instrument itself was installed on October 8-11th, 2012, and accessories (including radar) on December 11-13, 2012. This lidar emits at 3 wavelengths from IR to UV (1064 nm, polarised-532 nm, 355 nm) and records at 5 wavelengths, namely the emission wavelengths and two vibrational Raman channels at 387 and 607 nm. Measurements at 1064 nm, 532 nm, and 355 nm provide aerosol backscatter profiles, while measurements at 687 nm, and 387 nm provide aerosol extinction profiles during the dark hours of the day. The depolarisation of the 532 nm light beam is also measured. After the re-installation of the laser in Nov. 2015, the instrument has been run with a 5 min integration time according to the ACTRIS schedule (2 to 5 hr slots covering noon on Mondays and sunset on Mondays and Thursdays), and during Calipso overpasses (about once every 8 days at 01:40 or 12:30 UTC). The emission window was removed when the LiDAR was placed in a dedicated shelter on 28 May 2018. Data are inverted using the online Single Calculus Chain developed by

EARLINET, after pre-processing to cope with new requirements for submitting data to the ACTRIS-EARLINET data bank.

4.2.2.2 Sampling and off-line analyses

Particulate Matter

Particle sampler: Partisol 2025 S/N 2025B22156220203

Micro-balance: MC5 S/N 50208287

Ion Chromatographs: ICS 2000 S/N 07101404 and 07101405 and DX-120 (Jan.-Feb.)

OC-EC analyser: Sunset Lab OCEC analyser S/N 173.

PM_{2.5} was continuously sampled at 16.7 L min⁻¹ on quartz fibre filters with a Partisol sampler equipped with a carbon honeycomb denuder. The sampled area is 39 mm Ø. Filters were from PALL Life Sciences (type TISSUEQUARTZ 2500QAT-UP). Filter changes occurred daily at 08:00 UTC.

Filters were weighed at 20 % RH before and after sampling with a microbalance Sartorius MC5 placed in a controlled (dried or moisture added and scrubbed) atmosphere glove box. They were stored at 4°C until analysis.

Main ions (Cl⁻, NO₃⁻, SO₄²⁻, C₂O₄²⁻, Na⁺, NH₄⁺, K⁺, Mg²⁺, Ca²⁺) were analysed by ion chromatography with electrochemical eluent suppression (ICS2000) after extraction of the soluble species from an aliquot of 16 mm Ø in 10 ml of 18.2 MOhm cm resistivity water (Millipore mQ).

Organic and elemental carbon (OC+EC) were analysed using a Sunset Dual-optical Lab Thermal-Optical Carbon Aerosol Analyser (S/N 173-5). PM_{2.5} samples were analysed using the EUSAAR-2 thermal protocol according to EN 16909. It has been developed to minimise biases inherent to thermo-optical analysis of OC and EC (Cavalli et al., 2010), and is described in Table 5 below.

No measurement of PM₁₀ or PM_{coarse} was performed in 2018.

Table 5: Parameters of the EUSAAR-2 analytical protocol

Fraction Name	Plateau Temperature (°C)	Duration (s)	Carrier Gas
OC 1	200	120	He 100%
OC 2	300	150	He 100%
OC 3	450	180	He 100%
OC 4	650	180	He 100%
cool down		30	He 100%
EC1	500	120	He:O ₂ 98:2
EC2	550	120	He:O ₂ 98:2
EC3	700	70	He:O ₂ 98:2
EC4	850	110	He:O ₂ 98:2

Wet-only deposition

Precipitation sampler: Eigenbrodt Model NSA 181/KS S/N 3313 and 3312

Conductimeter and pH-meter: Sartorius Professional Meter PP-50 S/N 16350322.

Ion Chromatographs: ICS 2000 S/N 07101404 and 07101405

For precipitation collection, two wet-only samplers were used that automatically collect the rainfall in a 1 L polyethylene container. The collection surface is 550 cm². 24-hr integrated precipitation samples (if any) are collected every day starting at 8:00 UTC. All collected precipitation samples were stored at 4 °C until analyses (ca. every 3 months). Analyses include the determinations of pH and conductivity at 25 °C and principal ion concentrations

(Cl⁻, NO₃⁻, SO₄²⁻, C₂O₄²⁻, Na⁺, NH₄⁺, K⁺, Mg²⁺, Ca²⁺) by ion chromatography with electrochemical eluent suppression.

4.2.3 On-line data acquisition system/data management

4.2.3.1. DAQ for PM and meteorological parameters

The JRC EMEP-GAW station Data Acquisition System (DAS) is a specifically tailored set of hardware and software developed by the Air and Climate unit (initially in collaboration with F. Grassi and NOS s.r.l.), and designed to operate instruments, acquire both analogue and digital output from instruments and store pre-processed measurement data into a database for further off-line evaluation. The DAS operated and controlled the instrumentation during 2018. The new FDMS-TEOM (1405-F) was inserted in the DAS in 2018.

The software environment of the DAS is Labview 2014 v14.0.1 from [National Instruments](#) and the database engine for data storage is Microsoft SQL Server v17.9.1.

The DAS is designed to continuously run the following tasks:

- Start of the data acquisition at a defined time (must be full hour);
- Choose the instruments that have to be handled;
- Define the database path where data will be stored primary in LAKE3 and secondary locally on the acquisition machine;
- Define the period (10 minutes currently used) for storing averaged data, this is the data acquisition cycle time;
- Obtain data (every 10 seconds currently set) for all selected instruments within the data acquisition cycle:
 - o Send commands to query instruments for data or keep listening to the ports for instruments that have self-defined output timing (Aethalometer and DMPS);
 - o Scan instruments outputs to pick out the necessary data;
- Calculate average values and standard deviations for the cycle period;
- Query instruments for diagnostic data (when available), once every 10 minutes;
 - o Store all data in a database with the timestamp of their respective measurement for Aethalometer and DMPS
 - o And with the DAS time stamp for all other instruments.

The following instruments are managed with the DAS (Fig. 21), using 3 PCs (currently called EMEP DMPS-A, Emepacq5 and MeteoPrecipitation):

- EMEP DMPS-A
 - Number size distribution for particles diameter <0.800 µm
- Emepacq5:
 - Number size distribution for particles diameter >0.500 µm, APS
 - On-line FDMS-TEOMs
 - Aerosol light absorption, Aethalometer
 - Aerosol light absorption, MAAP
 - Aerosol light scattering, Nephelometer
- MeteoPrecipitation:
 - Solar radiation
 - Weather transmitter (temperature, pressure, relative humidity, wind speed and direction, precipitation)
 - Precipitation data.

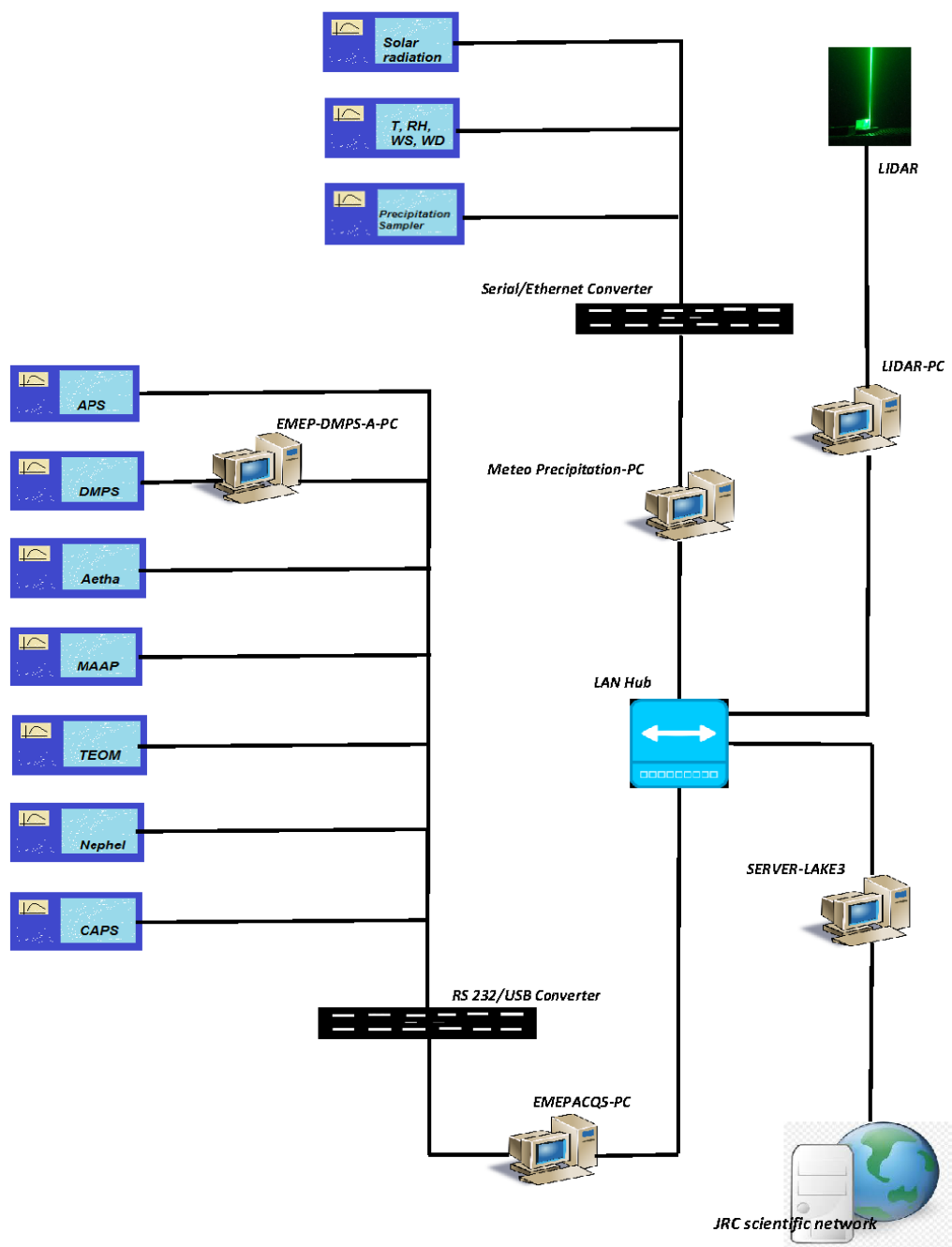


Fig. 21: Set-up of the Data Acquisition System.
 (a) Aerosol Physics Laboratory

The data acquired are stored in a Microsoft SQL Server database on the central database *abc-is_db* hosted on the pc Lake3. If the local network is not available, data are stored in a local database on the acquisition pc itself. Each pc also has software for the synchronisation of *abc-is_db* with *local db*.

The acquisition time is manually synchronised for all PCs and is kept at UTC, without adjustment for summer/winter time. Data are collected in a data base called *abc-is_db* that runs on the acquisition DB server Lake3.

The station web site (<https://abc-is.jrc.ec.europa.eu/>), runs over three machines, the acquisition DB server Lake3, the production DB server and the Web server in the DMZ (demilitarized zone).

Lake3 receives the data from the laboratory network container and performs a real time Data Base Replica of the relevant data on the production DB server.

The production Web server hosts the site <https://abc-is.jrc.ec.europa.eu> and makes the data in the production DB server available on the internet. In the web site the projects to which ABC-IS contributes and contact persons can also be retrieved.

The Life cycle data sheets are currently in the network share driver Laboratories, the data in this network storage is backup protected.

4.2.3.2. DAQ for reactive gases:

All analysers measuring reactive gases connect via serial or analogue signals to a data logger and data are transmitted via router to a database operated by AIP (UBIS4). Online access to the database allows data verification, correction, reporting and/or downloading. Further, the database launches automatic daily zero/span checks (Fig. 21b).

4.2.4 Data evaluation

The structured data evaluation system (EMEP_Main.m) with a graphic user interface (see Fig. 22) has been used with Matlab Release R2016a (www.mathworks.com) as the programming environment.

The data evaluation is now done with the "EMEP_Data_Handling L0 to L2" v. 1.9.9.8 - Nov 2017. Not evaluated 10 min data (flagged 3) is now exported to several excel sheets.

After a preliminary data analysis, these data are flagged according to the flags listed below. These files including flags are then imported into the database (level 1 data, 10 min corrected). Finally the hourly and the daily data averages are calculated taking into account the flagging.

0	Good data - used
1	Good data - not used
2	Calibration
3	Not evaluated
5	questionable
6	Local contamination
7	Erroneous data
9	No data

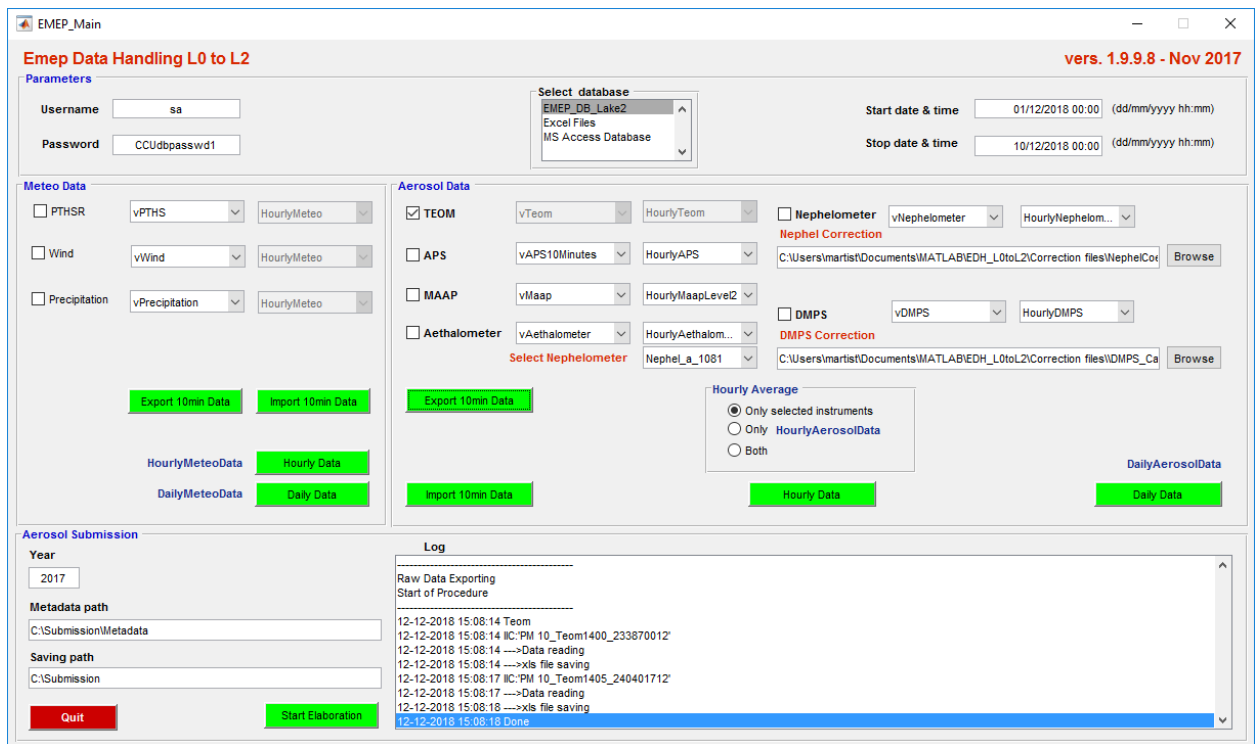


Fig. 22: Graphic user interface of the EMEP-GAW station data evaluation.

To check these data and to exclude outliers for all other measurements, a visual inspection of the 10 min data needs to be performed.

All database connections are implemented via ODBC calls (Open DataBase Connectivity) to the corresponding Microsoft SQL Server v17.9.1s.

Daily averages ($8:00 < t \leq 8:00 + 1 \text{ day}$) of all variables and parameters stored in the hourly averages database can be calculated and are subsequently stored in a separate Microsoft SQL Server v17.9.1. database.

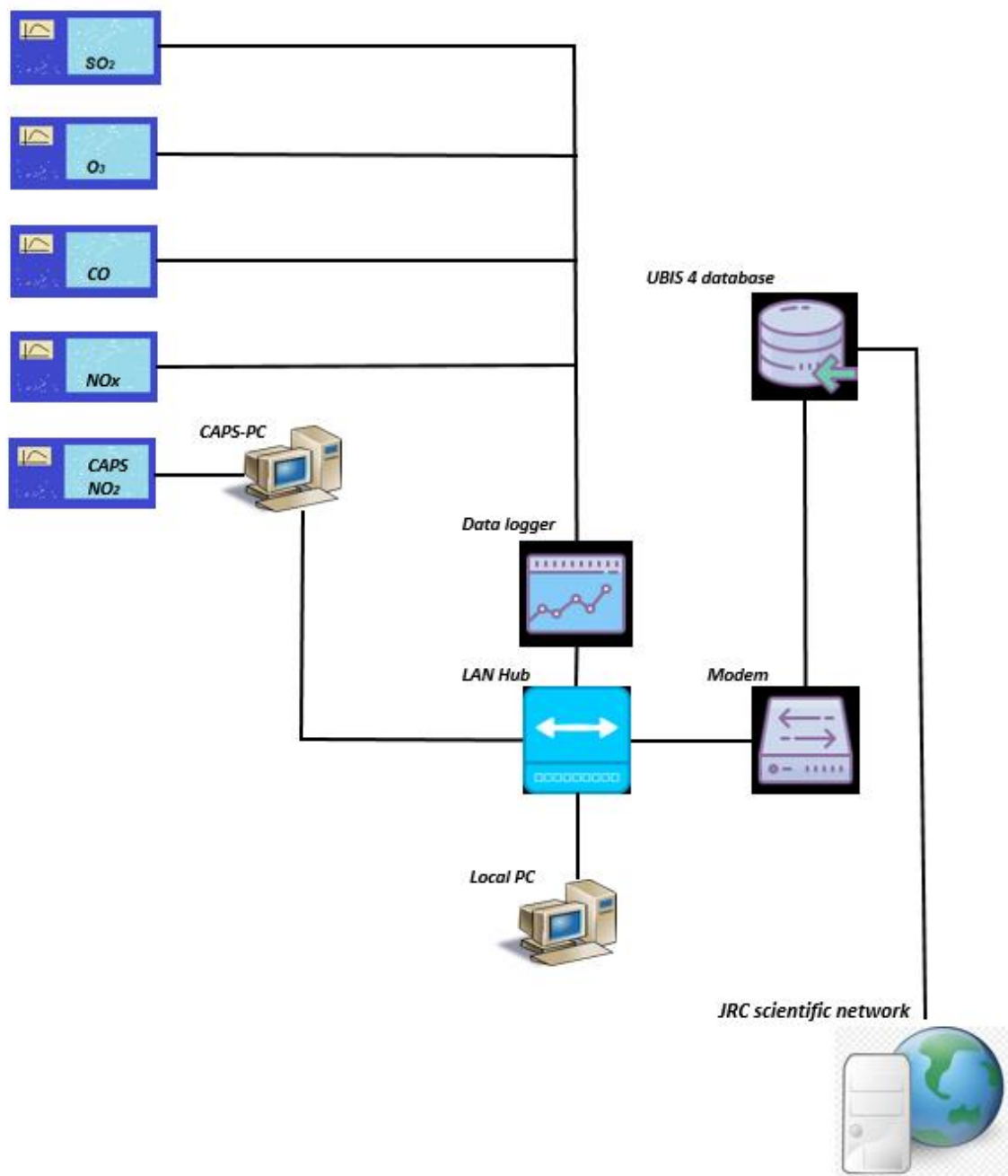


Fig. 21: Set-up of the Data Acquisition System.
 (b) Reactive Gases Laboratory

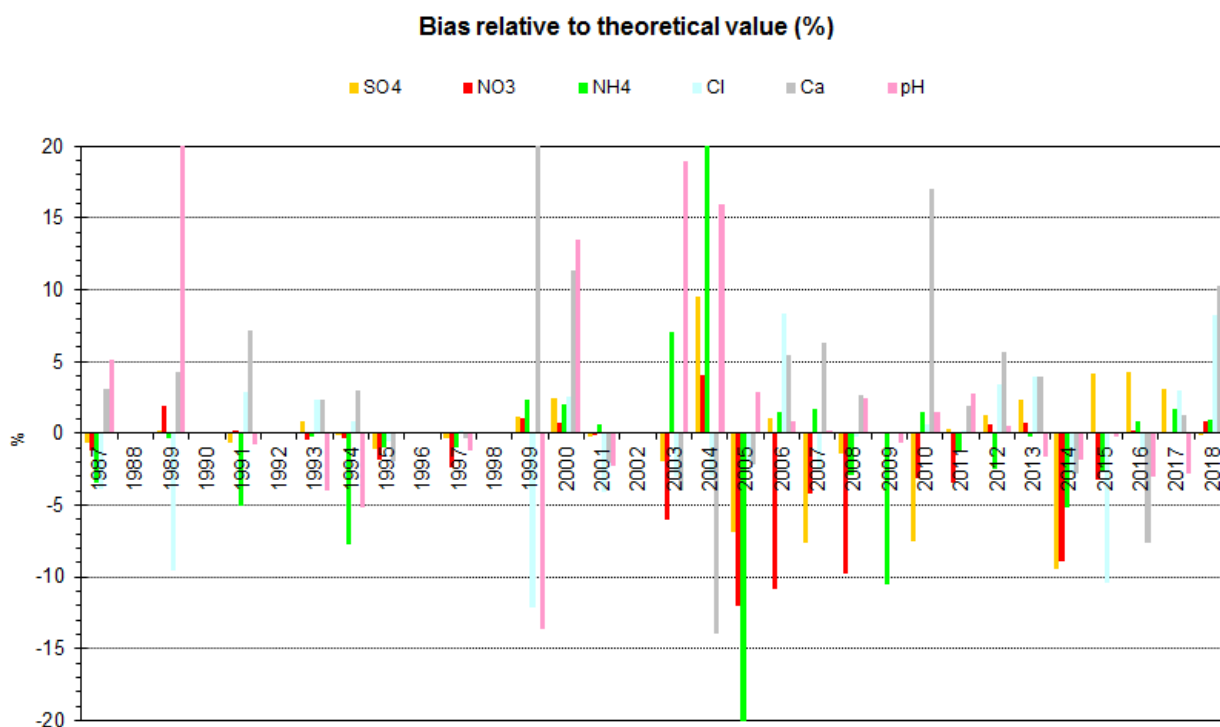


Fig. 23. EMEP inter-laboratory comparisons for rainwater analyses (1987-2018): JRC-Ispra results.

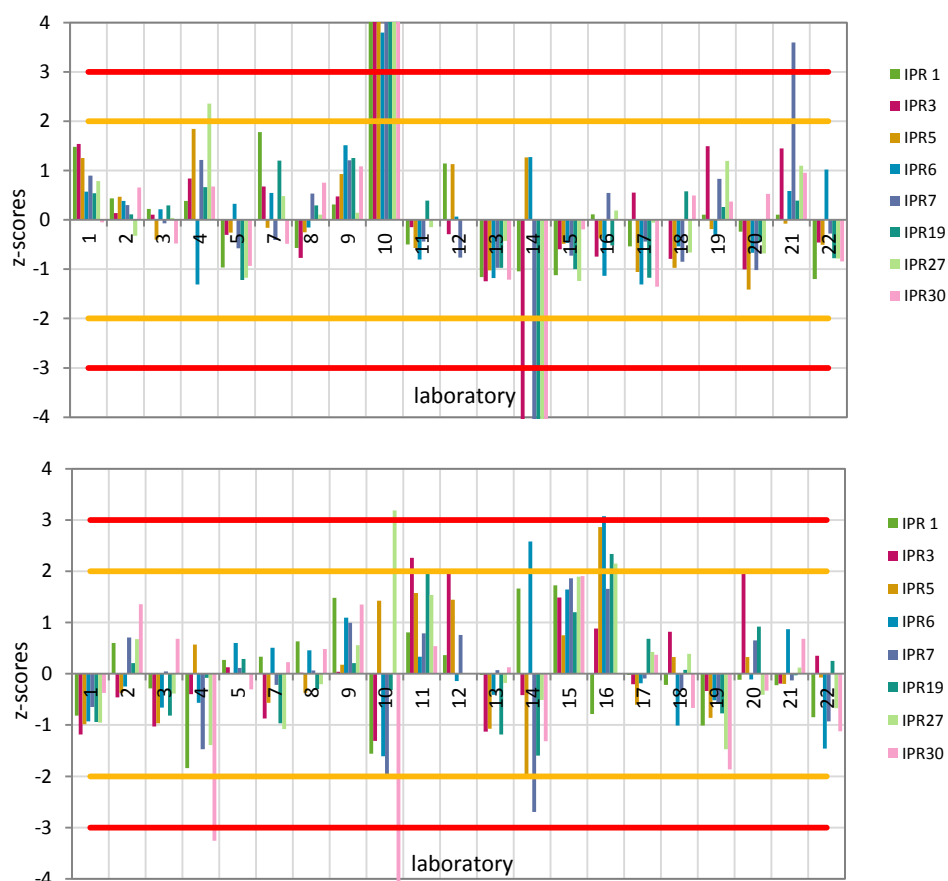


Fig. 24. JRC-Ispra instrument's (#22) performance for the determination of (top) total carbon (TC) and (bottom) elemental carbon (EC/TC ratio) during the ACTRIS inter-laboratory comparison 2018-1.

4.3 Quality assurance

At JRC level the quality system is based on the Total Quality Management philosophy, the implementation of which started at the Air and Climate Unit in December 1999. We have been working under ISO 9001 and ISO 14001 since 2010 (more information about our QMS system can also be found in the chapter "Quality management system").

Lacking personnel to specifically follow this business, the JRC-Ispra station for atmospheric research did not renew the accreditation for the monitoring of SO₂, NO, NO₂ and O₃ under EN 45001 obtained in 1999. However, measurements and standardised operating procedures are based on recommendations of the EMEP manual (1995, revised 1996; 2001; 2002; 2014), WMO/GAW 227, ISO and CEN standards. Moreover, the JRC-Ispra gas monitors and standards are checked by the European Reference Laboratory for Air Pollution (ERLAP) regularly. This includes, next to annual preventive maintenance, linearity check and Gas Phase Titration (for NO_x) the re-certification of working – standards with primary reference material (PRM) allowing full traceability to SI units. ERLAP's accreditation (ISO 17025) was achieved in 2013 and is still valid.

For on-line aerosol measurements, [ACTRIS](#) Standard Operating Procedures and QA/QC requirements are followed. Those involve station audits, side by side instrument comparisons at the world calibration centre for aerosol physics (WCCAP) in Leipzig (DE), and specific QC measurements. The station was favourably audited by Dr. T. Tuch (WCCAP) on 22-24 March 2010 under the EUSAAR project (www.eusaar.net), as described in a specific [report](#). JRC's integrating nephelometer (see [report](#)) and absorption spectrometers (see [reports](#)) successfully took part in side by side comparisons at the World Calibration Centre for Atmospheric Physics in Leipzig in Sept. 2017. The two Condensation Particle Counters used as part of our Differential Mobility Particle Sizer were both successfully checked at the WCCAP in April and September 2018 (see [report 1](#) and [report 2](#) at the [ACTRIS-ECAC web site](#)).

The aerosol LiDAR was successfully audited and on-site compared with an ACTRIS reference instrument during the period 17 – 27 July 2018. The system alignment is checked for each measurement through its calibration in a particle –free region of the atmosphere. Quality check measurements are reported at least once a year to the ACTRIS Lidar Calibration Centre, which produces a detailed report on the instrument performance.

Ion analysis quality was checked as part of the 36th annual EMEP inter-laboratory comparison (Fig. 23). In this exercise, all ion measurements in the rain water synthetic samples provided by NILU passed the quality test. The data quality objective within EMEP is 10% accuracy or better for NO₃⁻ and SO₄²⁻ and 15% accuracy or better for other components for each sample. pH measurements were on average accurate but the deviation to the assigned value ranged between -0.16 and +0.01.

The inter-laboratory comparison for organic and elemental carbon analyses organised under the competitive project ACTRIS-2 in 2018 indicates no systematic bias for the determination of total carbon and elemental carbon compared to the robust average among the participants (Fig. 24). Data quality for all measurements is also checked whenever possible through comparison among different instruments, mass closure (for PM) and ion balance (for precipitation) exercises (see specific sections).

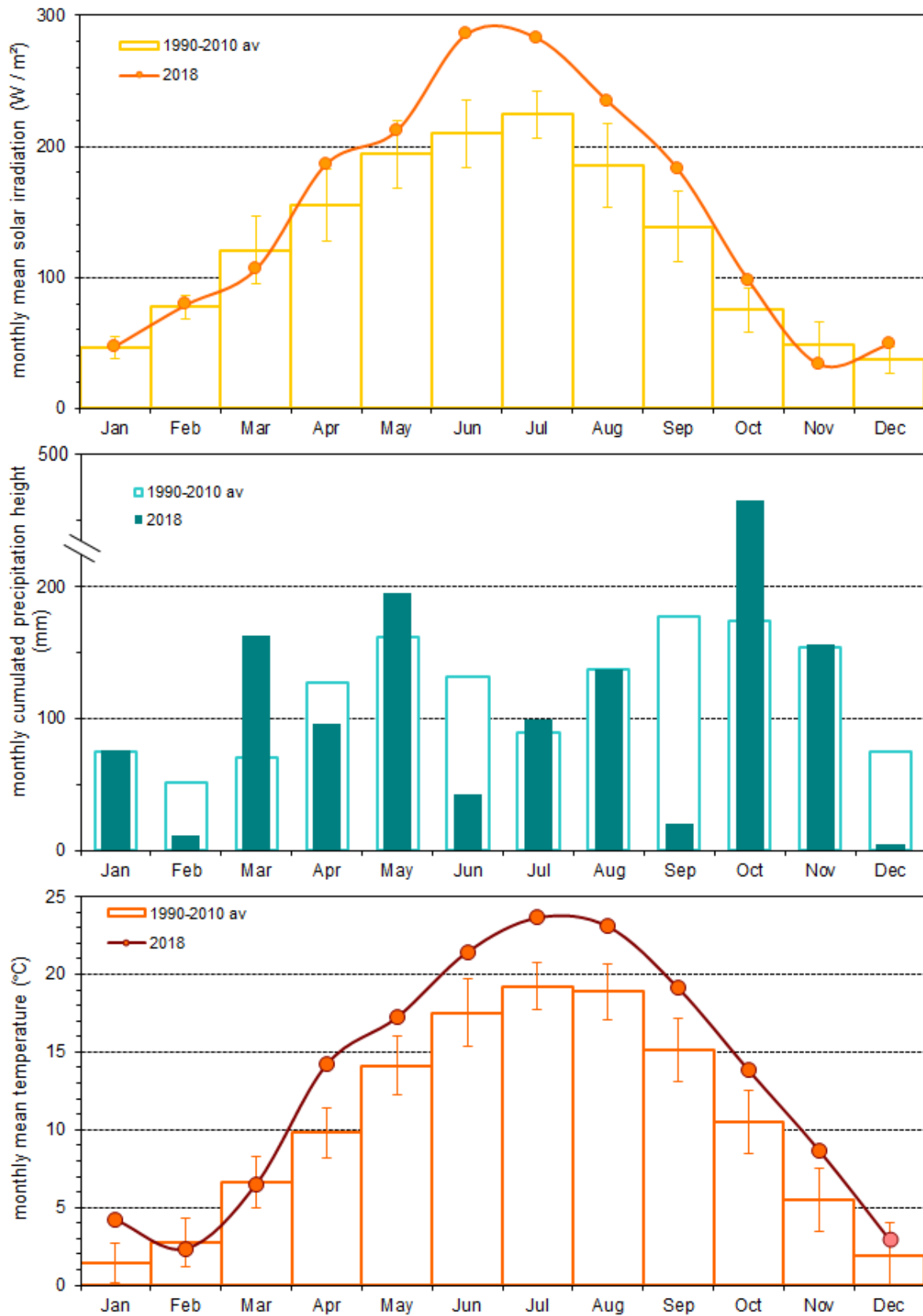


Fig. 25: Solar global irradiation, precipitation amount, and temperature monthly values observed at the Observatory in Ispra in 2018, compared to the 1990-2010 period \pm standard deviations.

4.4 Results for the year 2018

4.4.1 Meteorology

Meteorological data were acquired at using a Pyranometer (solar radiation) and a weather transmitter (T, P, RH, precipitation) located at 9 m above the ground at the atmospheric observatory, respectively. Meteorological data cover the whole of 2018. In Fig. 25, monthly values of these meteorological variables for 2018 are compared to the 1990-2010 average used as reference period.

The monthly mean solar radiation was significantly greater than average in June – September. Year 2018 was also warmer compared to the reference period in January and from April to November. February, September and December were particularly dry, while October was exceptionally wet. The total yearly rainfall was 1470 mm, i.e. very similar to the 1990-2010 average (1423 mm).

4.4.2 Gas phase air pollutants

SO₂, CO, NO_x and O₃ were measured continuously at the atmospheric observatory during the year 2018, except for NO_x on 1 day in September and CO on 2 days in December due to repair works on analysers (annual data coverage > 99 %). Expanded uncertainties for the measured concentrations were calculated to be 5.5% + 0.7 ppb for SO₂, 6% + 0.07 ppm for CO, 7% + 1.2 ppb for NO, 7.5% +1.5 ppb for NO₂ and 6% +0.7 ppb for O₃, which is in line with the *European Directive 2008/50/EC* (less than 15 % at the limit value). To render the time series more representative of regional background conditions, *10 min SO₂, NO_x and CO data were flagged for local contamination (0.5-4% of the data points), and hourly (and daily) averages were computed excluding the data points for which local contamination was identified.*

In 2018, the seasonal variations in SO₂, NO, NO₂, NO_x and O₃ were similar to those observed over the 1990-2010 period (Fig. 26). Concentrations are generally highest during wintertime for primary pollutants (SO₂, CO, NO_x), and in summertime for O₃. Higher concentrations of SO₂, CO, NO_x in winter result mainly from a least dispersion of pollutant during cold months (low boundary layer height and stagnant conditions), whereas the high concentration of O₃ during summer is due to enhanced photochemical production.

SO₂ concentrations (average = 0.6 µg/m³) were slightly less than 2016 and 2017 values, and about 5 times less compared to the reference period (1990-2010).

Daily mean CO concentrations ranged from 0.13 to 1.1 mg m⁻³ (0.1 – 0.9 ppmv), which are typical values in a regional background station like the atmospheric observatory in Ispra, and less than half the values observed in the 1990-2000's. The lowest values were observed in very clean air masses during Föhn events and windy summer days, and the highest values during cold winter nights.

NO concentrations (annual average = 4.1 µg m⁻³) were 10% less than in 2017, and 35% less than in 2016. Due to the short atmospheric lifetime of NO, its average concentrations are much sensitive to the filtering for local contamination.

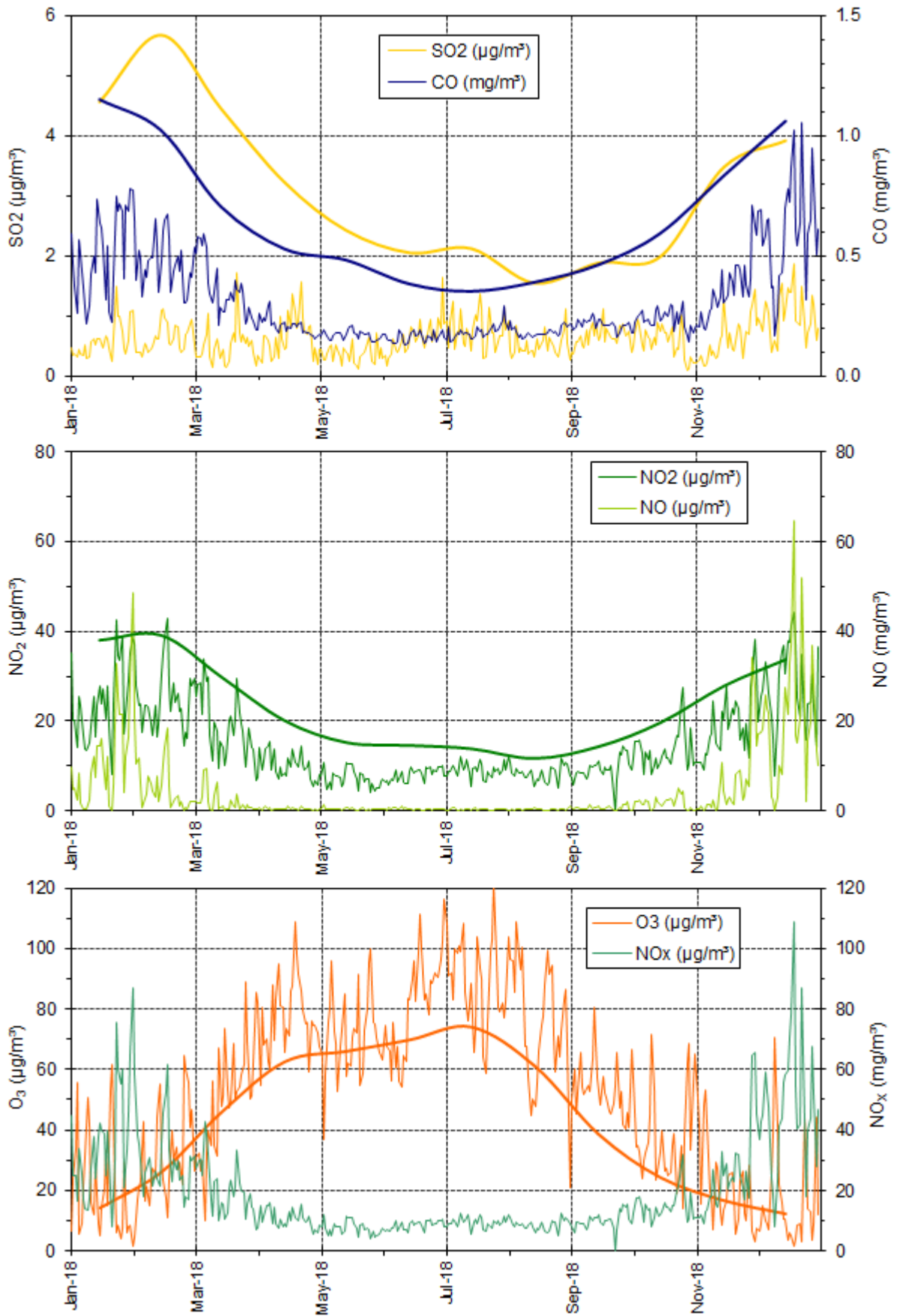


Fig. 26. Seasonal variations of the 24 hr averaged concentrations of SO_2 , CO , NO_2 , NO , O_3 and NO_x in 2018 (thin lines) and 1990-2010 monthly averages (thick lines: yellow= SO_2 , blue= CO , green= NO_2 , orange= O_3). Concentrations are in EMEP standard conditions (1013 hPa, 293K).

NO₂ concentrations (annual average = 15 µg m⁻³) were less than during previous years (18 µg m⁻³ in 2016 and 19.5 µg m⁻³ in 2017), and on average 35% less than during 1990-2010.

The temporal coverage for O₃ measurements was close to 100% in 2018. The O₃ indices for 2018 were therefore calculated without need for gap filling. The annual average O₃ concentration in 2018 (52 µg m⁻³, 26 ppb) was not significantly lower than in 2017, and 10% greater than in 2016, which confirms the relatively high O₃ concentrations observed since the early 2010's. The high O₃ mean concentration can probably be partly explained by both the average insolation and temperature being much greater than average from spring to autumn in 2018.

The vegetation exposure to above the ozone threshold of 40 ppb (AOT 40 = Accumulated dose of ozone Over a Threshold of 40 ppb, normally used for "crops exposure to ozone") was 34300 ppb h (Fig. 27), i.e. 20% more than in 2017 and 50% more than in 2016.

For quantification of the health impacts (population exposure), the World Health Organisation uses the SOMO35 indicator (Sum of Ozone Means over 35 ppb, where means stands for maximum 8-hour mean over day), i.e. the accumulated ozone concentrations dose over a threshold of 35 ppb (WHO, 2008). In 2018, SOMO35 was 4645 ppb day (Fig. 27), i.e. 20% less than in 2017 (5940), but 40% more than in 2016 (3360), and 15% more than in 2015 (4030). As much as 11 extreme O₃ concentration events (>180 µg m⁻³ over 1 hour) were observed in 2018, to be compared to 0, 8, and 17 extreme events in 2017, 2016, and 2015, respectively. The value 180 µg m⁻³ over 1 hour corresponds to the threshold above which authorities have to inform the public (European Directive 2008/50/EC on ambient air quality and cleaner air for Europe).

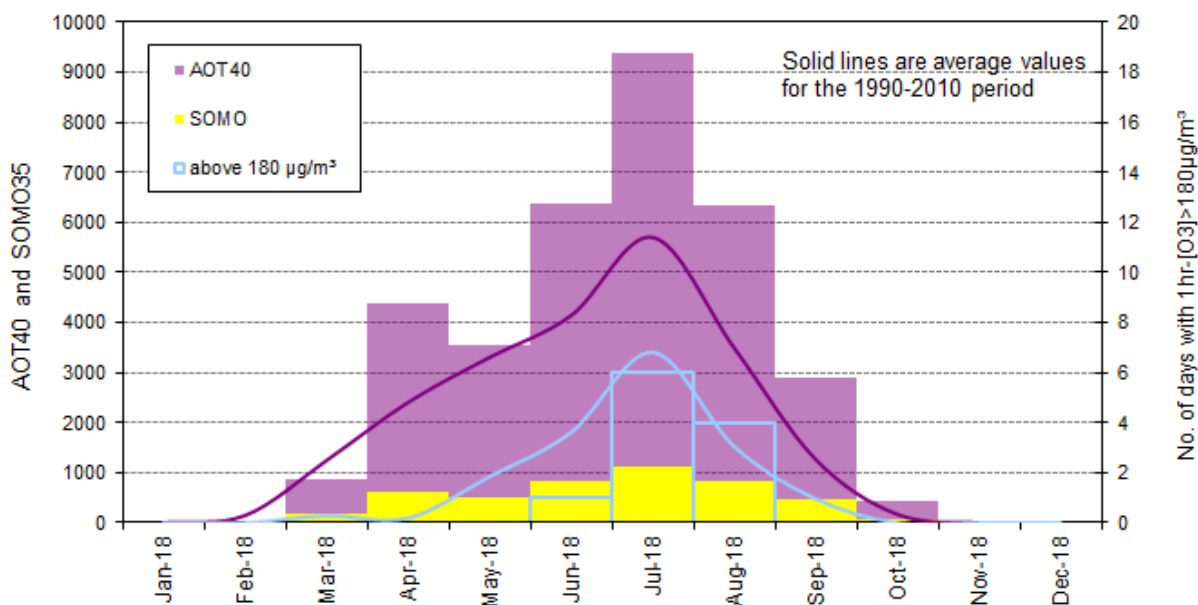


Fig. 27: AOT 40 (ppb h), SOMO35 (ppb day) and number of exceedances of the 1hr-averaged 180 µg/m³ threshold in 2018 (bars). Lines show values for the reference period 1990-2010.

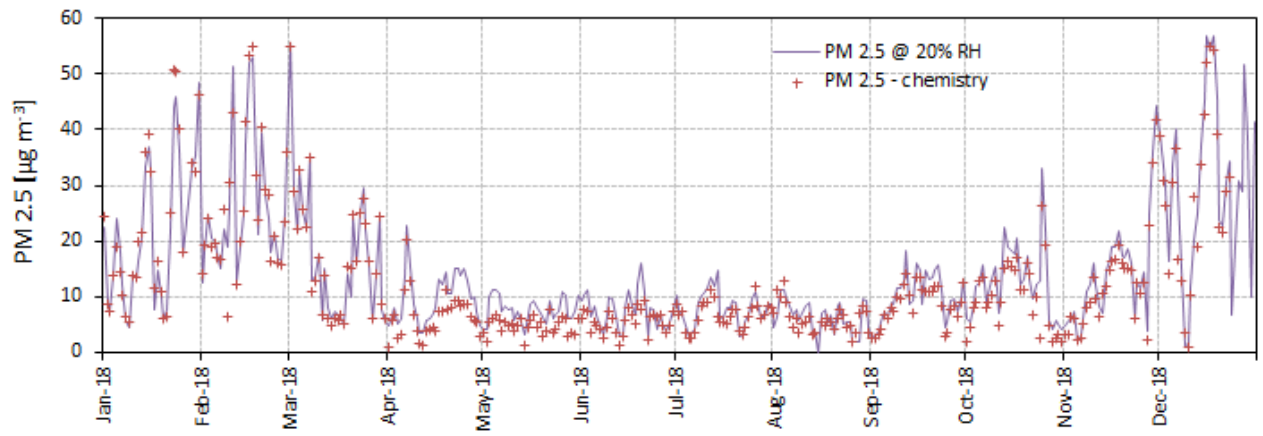


Fig. 28: 24hr-integrated $PM_{2.5}$ mass concentrations from off-line gravimetric measurements at 20 % RH and chemical determination of main constituents in 2018.

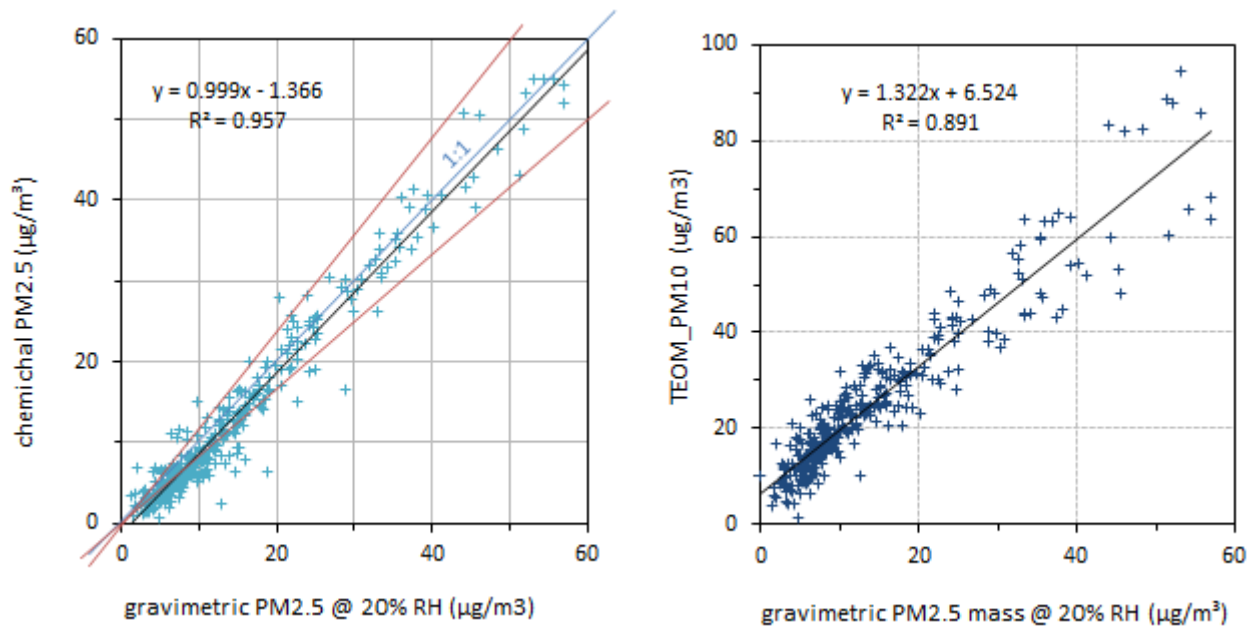


Fig. 29. Regressions between the gravimetric $PM_{2.5}$ measurements at 20 % RH and the sum of $PM_{2.5}$ chemical constituents (left), and the FDMS-TEOM PM_{10} measurements (right) in 2018.

During the reference period 1990-2010, the information level of $180 \mu\text{g m}^{-3}$ had been exceeded 17 times per year on average. The other “protection of human health factor” mentioned by the European Directive 2008/50/EC ($120 \mu\text{g m}^{-3}$ as maximum daily 8-hour average) was exceeded 117 times in 2018 (vs 5 times in 2017 and 77 times in 2016), leading to a 3-year average of 66 exceedances per year, well above the Directive limit value (25 exceedances per year).

Non-Methane Hydrocarbons (ethane, ethene, propane, propene, acetylene, iso-butane, n-butane, trans-2-butene, 1-butene, cis-2-butene, 2-methylbutane, n-pentane, 1,3-butadiene, trans-2-pentene, 1-pentene, 2-methylpentane, isoprene, n-hexane, benzene, n-heptane, 2,2,4-trimethylpentane, toluene, ethylbenzene, m-xylene, o-xylene, p-xylene, 1,3,5-trimethylbenzene, 1,2,4-tri-methylbenzene, 1,2,3-tri-methylbenzene) were measured usually for two 24 h cycles per week (24 samples of about one hour duration per cycle) in the period 04.04.2018-19.12.2018. Expanded uncertainties were estimated to be about 15 %. Isoprene (biogenic compound) concentrations were about 2 ppb in the summertime and close to the detection limit of about 0.05 ppb during wintertime, as expected (see e.g. Jensen et al., 2018). In contrast, benzene and toluene (anthropogenic compounds) concentrations were significantly higher in winter (0.7 and 0.8 ppb, respectively) than in summer (0.1 and 0.3 ppb, respectively). European benzene annual average limit value is 1.5 ppb (European Directive 2008/50/EC). Compared to 1999, isoprene concentrations have not significantly changed, while toluene concentrations have decreased by about a factor of two (for summer-time and winter-time), and benzene concentrations have decreased by about a factor of two (for summer-time only).

4.4.3 Particulate phase

4.4.3.1 Particulate matter mass concentrations

PM_{2.5} concentrations (Fig. 28) measured gravimetrically at 20 % relative humidity (RH) averaged $14.1 \mu\text{g m}^{-3}$ in 2018, i.e. 10% less than in 2017 ($15.5 \mu\text{g m}^{-3}$). This was amongst the lowest values observed since this measurement was started in 2002 (lowest = $13.1 \mu\text{g m}^{-3}$ in 2014), well below the European annual limit value of $25 \mu\text{g m}^{-3}$ to be reached by 2015 ([European directive 2008/50/EC](#)). Gravimetric measurements of PM_{2.5} mass at 20% RH and the sum of PM_{2.5} mass constituents determined from chemical analyses are well correlated (Fig. 29), with relative differences below 20% for mass concentrations $> 30 \mu\text{g/m}^3$. However, mass closure is not reached for many data points below $30 \mu\text{g/m}^3$, and the intercept is significantly negative, which was not observed for the previous years.

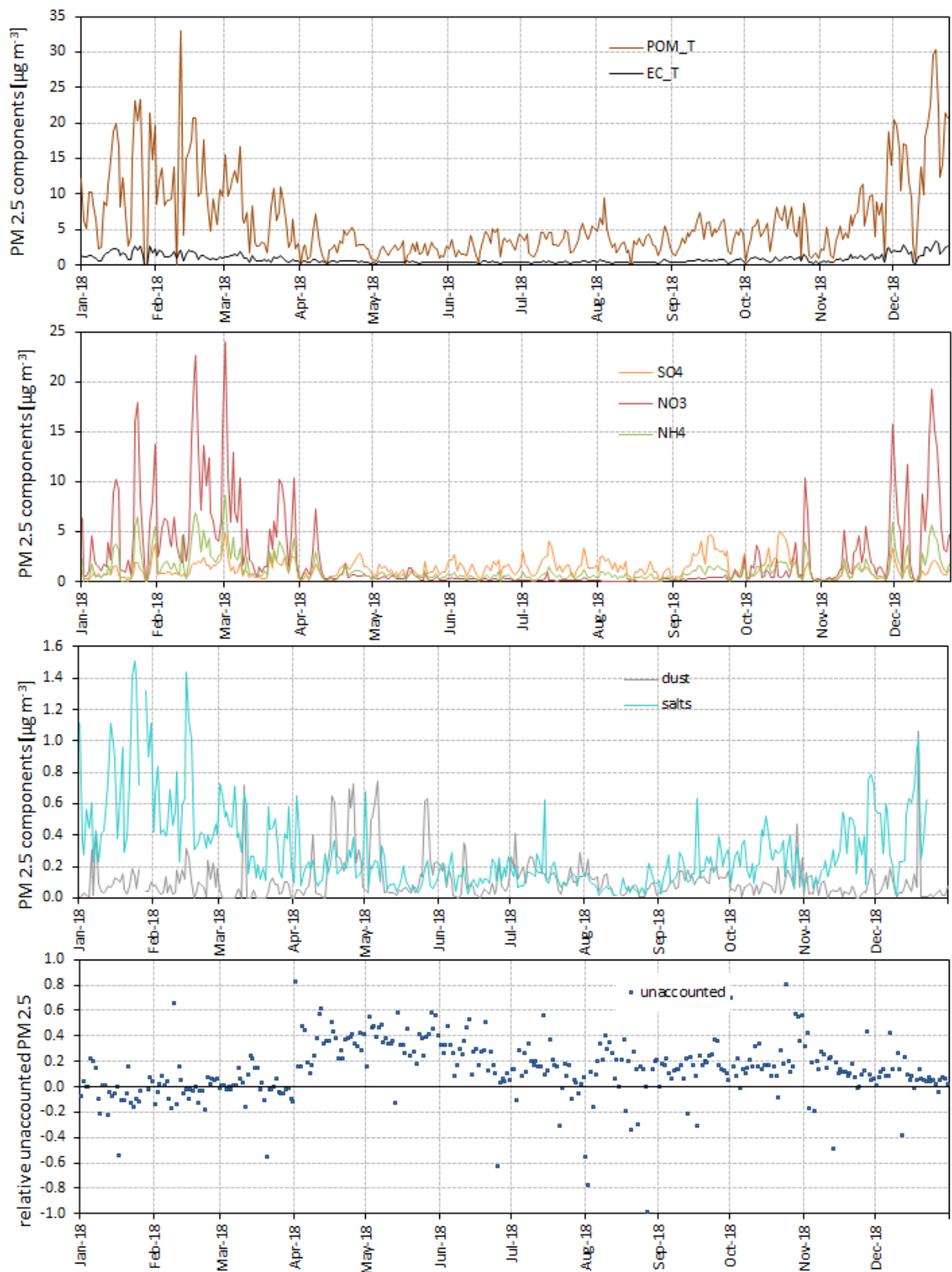


Fig. 30 24-hr integrated concentrations of the main PM_{2.5} constituents in 2018, and the relative unaccounted mass

The correlation between PM₁₀ FDMS-TEOM and gravimetric PM_{2.5} measurements for 2018 (Fig. 29) is similar to that observed in 2017 in terms of slope, intercept and regression coefficient (and worse than in 2016), partly due to the variability in the PM_{coarse} fraction. The intercept of 6.5 µg/m³ suggests an offset in FDMS-TEOM measurements, negative sampling artefacts related to the quartz fibre filters used to collect PM_{2.5}, or a combination of both. In 2018, the annual data coverage for the FDMS-TEOM measurements of PM₁₀ was 97%. The number of exceedances of the 24-hr limit value (50 µg m⁻³) observed in 2018 (28) was less than the threshold (35) indicated in the [European directive 2008/50/EC](#). This was much less than in 2017 (43), but larger than the 21 and 16 exceedances observed in 2015 and 2014, respectively.

The 2018 annual PM₁₀ average (25.2 µg m⁻³) was 10% less than in 2017, and well below the annual limit value of 40 µg/m³ of the [European directive 2008/50/EC](#).

4.4.3.2 PM_{2.5} chemical composition

Main ions (Cl⁻, NO₃⁻, SO₄²⁻, C₂O₄²⁻, Na⁺, NH₄⁺, K⁺, Mg²⁺, and Ca²⁺), OC and EC were determined from the quartz fibre filters collected for PM mass concentration measurements for the whole of 2018 (data coverage = 99%).

Fig. 30 shows the temporal variations in the PM_{2.5} main components derived from these measurements. Particulate organic matter (POM) is calculated by multiplying OC (organic carbon) values by the 1.4 conversion factor to account for non-C atoms contained in POM (Russell et al., 2003). "Salts" include Na⁺, K⁺, Mg²⁺, and Ca²⁺. Dust is calculated from Ca²⁺ concentrations and the regression (slope = 4.5) found between ash and Ca²⁺ in the analyses of ash-less cellulose filters (Whatman 40) in previous years. Most components show seasonal variations with higher concentrations in autumn and winter, and lower concentrations in summer, like PM_{2.5} mass concentration. This is mainly due to changes in pollutant horizontal and vertical dispersion, related to seasonal variations in meteorology (e.g. lower boundary layer in winter). The magnitude of the POM, NH₄⁺ and NO₃⁻ seasonal cycles may be enhanced due to equilibrium shifts towards the gas phase, and/or to enhanced losses (negative sampling artefact) from quartz fibre filters during warmer months. Indeed, historical data (May – Sept. 2013) show that the concentration of NH₄NO₃ in PM_{2.5} determined from filters can be 1/5 of the concentration measured in the submicron aerosol with an ACSM (see 2013 annual report).

NH₄⁺ and NO₃⁻ + SO₄²⁻ were very well as correlated as indicated by the regression shown in Fig. 31. This correlation results from the atmospheric reaction between NH₃ and the secondary pollutants H₂SO₄ and HNO₃ produced from the oxidation of SO₂ and NO_x, respectively. The ratio between NO₃⁻ + SO₄²⁻ and NH₄⁺ was close to 1 (which means that sufficient NH₃ was available in the atmosphere to neutralise both H₂SO₄ and HNO₃), except for 1 outlier. These measurements suggest that on average PM_{2.5} aerosol was probably not acidic.

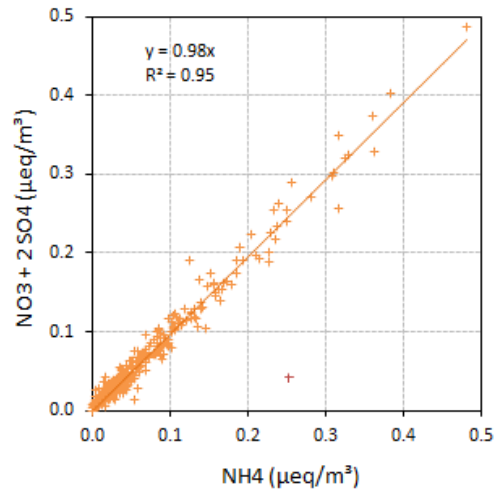


Fig. 31. $SO_4^{2-} + NO_3^-$ vs. NH_4^+ ($\mu\text{eq}/\text{m}^3$) in $PM_{2.5}$ for 2018

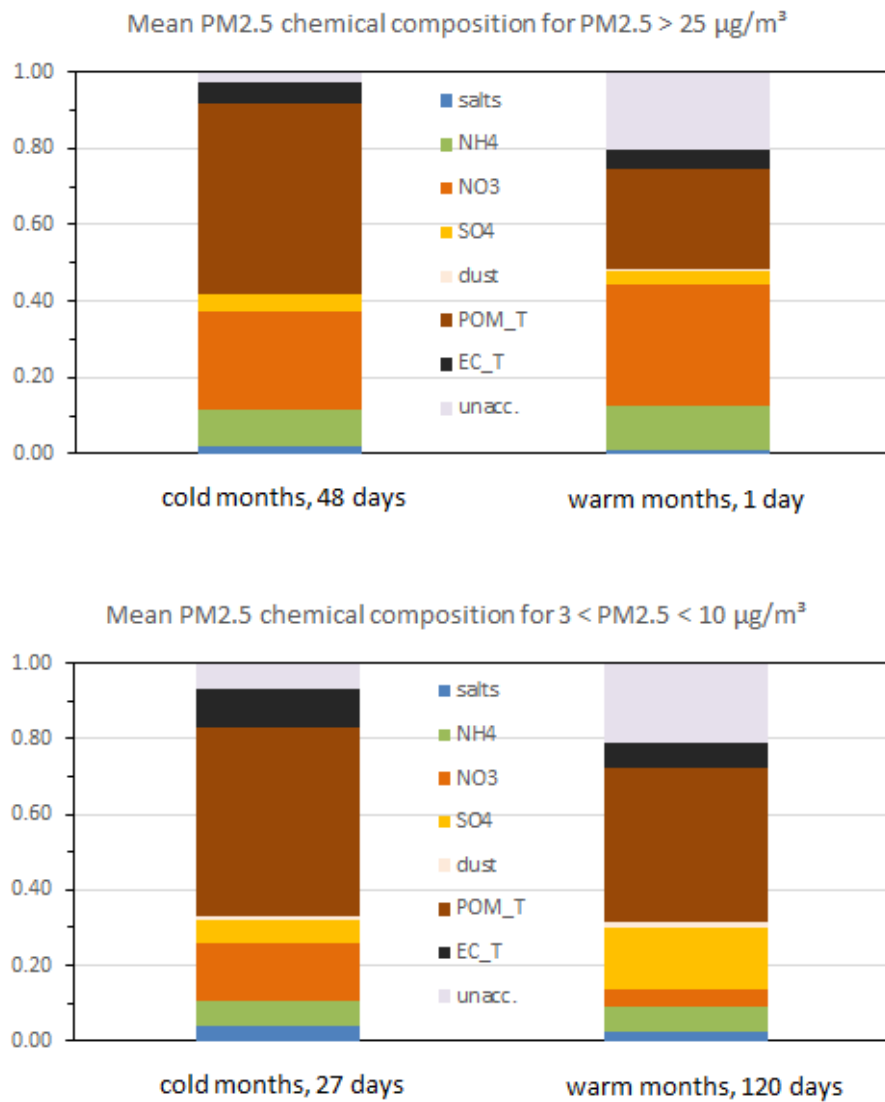


Fig. 32: Average composition of $PM_{2.5}$ in 2018 for days on which $PM_{2.5} > 25 \mu\text{g}/\text{m}^3$ (top) and $3 < PM_{2.5} < 10 \mu\text{g}/\text{m}^3$ (bottom), over cold (Jan., Feb., Mar., Nov., Dec.) and warm (Apr. – Oct.) months.

4.4.3.3 Contribution of the main aerosol constituents to PM_{2.5}

The contributions of the main aerosol components to PM_{2.5} are presented in Table 6 (annual averages) and in Fig. 32 (a) for days on which the “24-hr limit value for PM_{2.5} of >25 µg/m³ was exceeded” during the cold months (Jan., Feb., March, Nov. and Dec., 48 cases) and the warm months (Apr. to Oct, 1 case only) and (b) for days on which 24-hr integrated PM_{2.5} concentration was below 10 µg / m³ but above 3 µg / m³ during cold (27 cases) and warm months (120 cases).

These PM_{2.5} compositions may not always represent accurately the actual composition of particulate matter in the atmosphere (mainly due to possible negative sampling artefacts), but are useful to assess which components contributed to the PM_{2.5} mass collected by a quartz fibre filter downstream of a 20 cm-long carbon monolith denuder.

Over the whole year 2018, carbonaceous species accounted for 51% of PM_{2.5} (EC: 6%, POM: 44%), and secondary inorganics for 32% (NH₄: 8%, NO₃: 12%, and SO₄: 12%). In both the cold and the warm seasons, particulate air pollution days are characterised by a strong increase in NO₃⁻ contribution. Considering low PM_{2.5} concentration days, summertime is characterised by higher SO₄²⁻ concentrations (faster SO₂ photochemical conversion) and lower NO₃⁻ concentrations (equilibrium shifted towards the gas phase as temperatures increase). Dust and salts do not contribute significantly to the PM_{2.5} mass, but their contribution is larger on cleanest days compared to most polluted days.

Table 6: Annual mean concentrations and contributions of major PM_{2.5} constituents in 2018

constituent	salts	NH ₄ ⁺	NO ₃ ⁻	SO ₄ ²⁻	POM	EC	dust	unaccounted
	Cl ⁻ , Na ⁺ , K ⁺ , Mg ²⁺ , and Ca ²⁺							
Mean concentration (µg m ⁻³)	0.3	1.2	2.5	1.3	6.5	0.9	0.1	
Mean contribution (%)	2.3	8.0	12.3	11.9	44.3	6.4	1.1	13.7

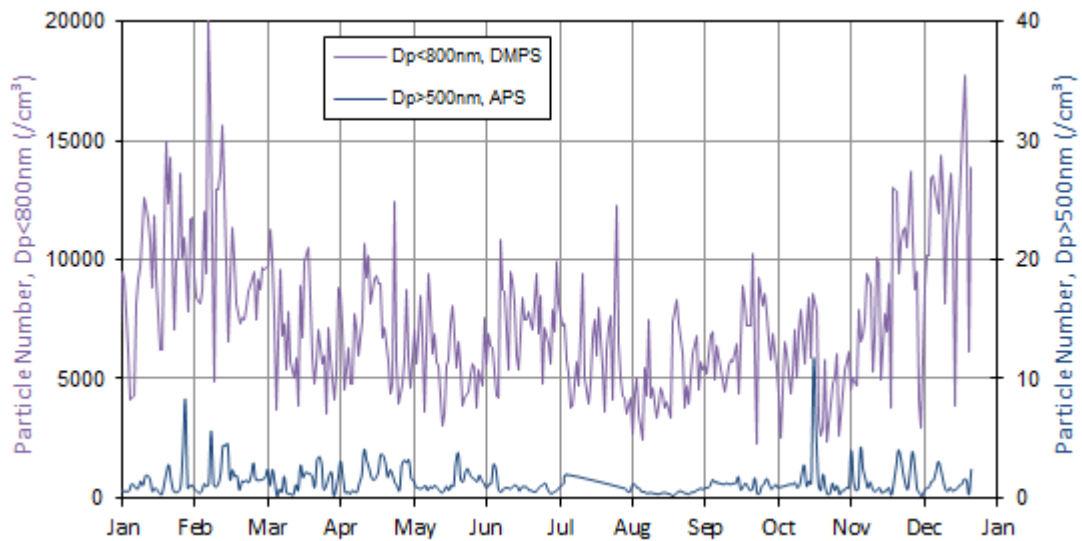


Fig. 33. 24 hr - averaged particle number concentrations for $D_p < 800 \text{ nm}$ and $D_p > 500 \text{ nm}$.

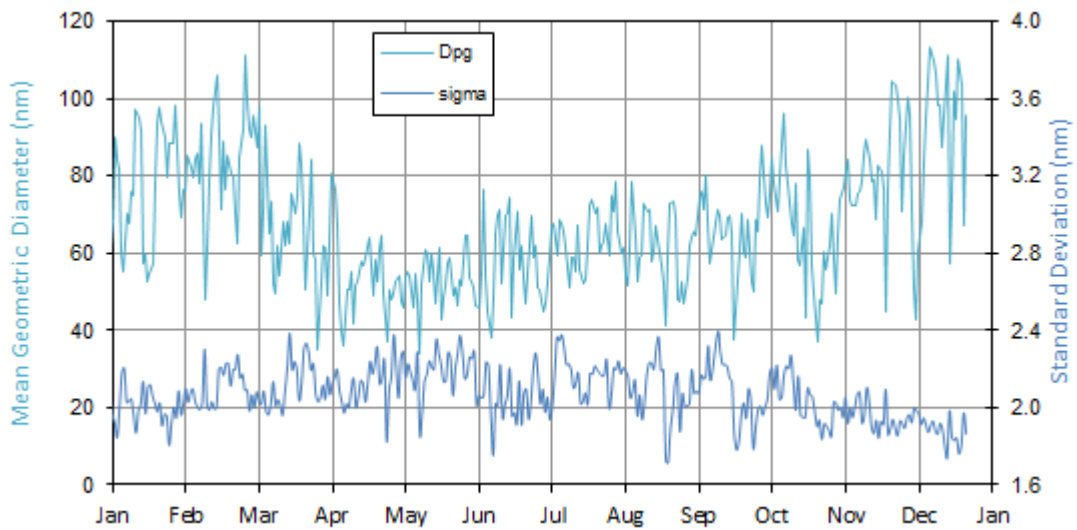


Fig. 34. 24 hr - averaged particle geometric mean mobility diameter (from DMPS) and standard deviation

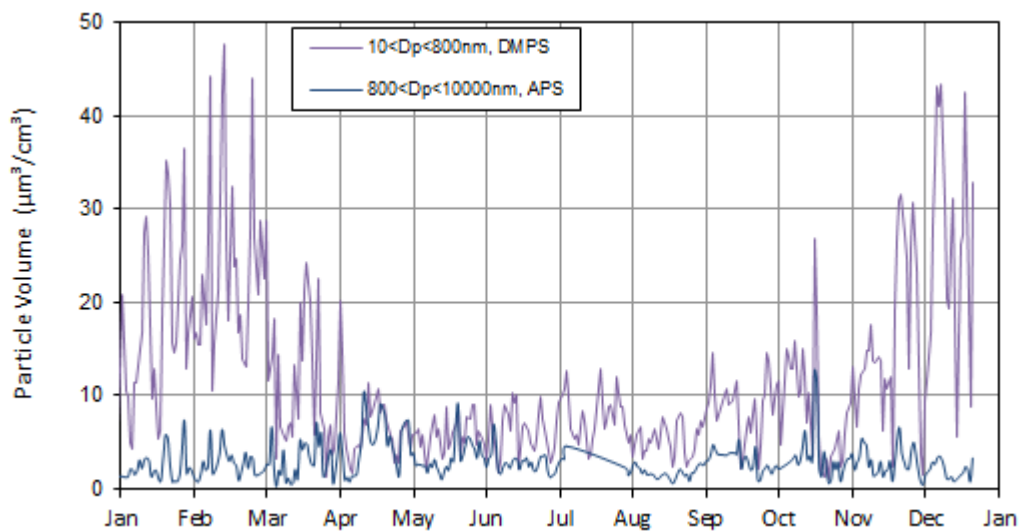


Fig. 35. 24 hr - averaged particle volume concentrations for $D_p < 800 \text{ nm}$ and $D_p > 800 \text{ nm}$.

4.4.3.4 Aerosol micro-physical properties

Measurements of the number size distribution of particles smaller than 800 nm diameter were carried out using a Differential Mobility Particle Sizer almost continuously in 2018, except for a 2-day gap in September for corrective maintenance, resulting in a data coverage of 99%. The DMPS data presented here have been corrected for inlet diffusion losses and CPC efficiency.

Particle number concentrations averaged over 24 hr (from 08:00 to 08:00 UTC) ranged from 2300 to 20100 cm⁻³ (average: 7300 cm⁻³) and followed a seasonal cycle similar to that of PM mass concentrations, with maxima in winter and minima in summer (Fig. 33). Episodes of local contamination were flagged during the data analysis process. Excluding the data points affected by local contamination (4% of the data), the annual mean particle number drops by 8%.

The mean mode diameter at RH < 40 % ranged between 34 and 113 nm (average = 68 nm) in 2018. These metrics are rather constant from year to year. However, the variations in particle size distribution characteristics (Fig. 34) show seasonal patterns as well: the mean geometric diameter is generally larger in winter (about 60-110 nm) than in summer (about 40- 80 nm), whereas the standard deviation of the distribution follows an opposite trend (with a larger variability in summer compared to winter).

The size distribution of particles larger than 500 nm was measured using an Aerodynamic Particle Sizer almost continuously over 2018 except for a 25-day gap in July-August (corrective maintenance at the manufacturer's) and five 2 to 4 day gaps (on-site corrective maintenance), resulting in a data coverage of 90%. Aerodynamic diameters were converted to geometric diameter assuming a particle density of 1.40. As previously observed, particles larger than 500 nm generally (90th percentile) accounted for <0.04% of the total particle number only (Fig. 33), but for 24 % of the total particle volume on average (Fig. 35). The seasonal variations in particle volume concentration reflect the changes in particle number and mean geometric diameter, with larger concentrations in winter than in summer.

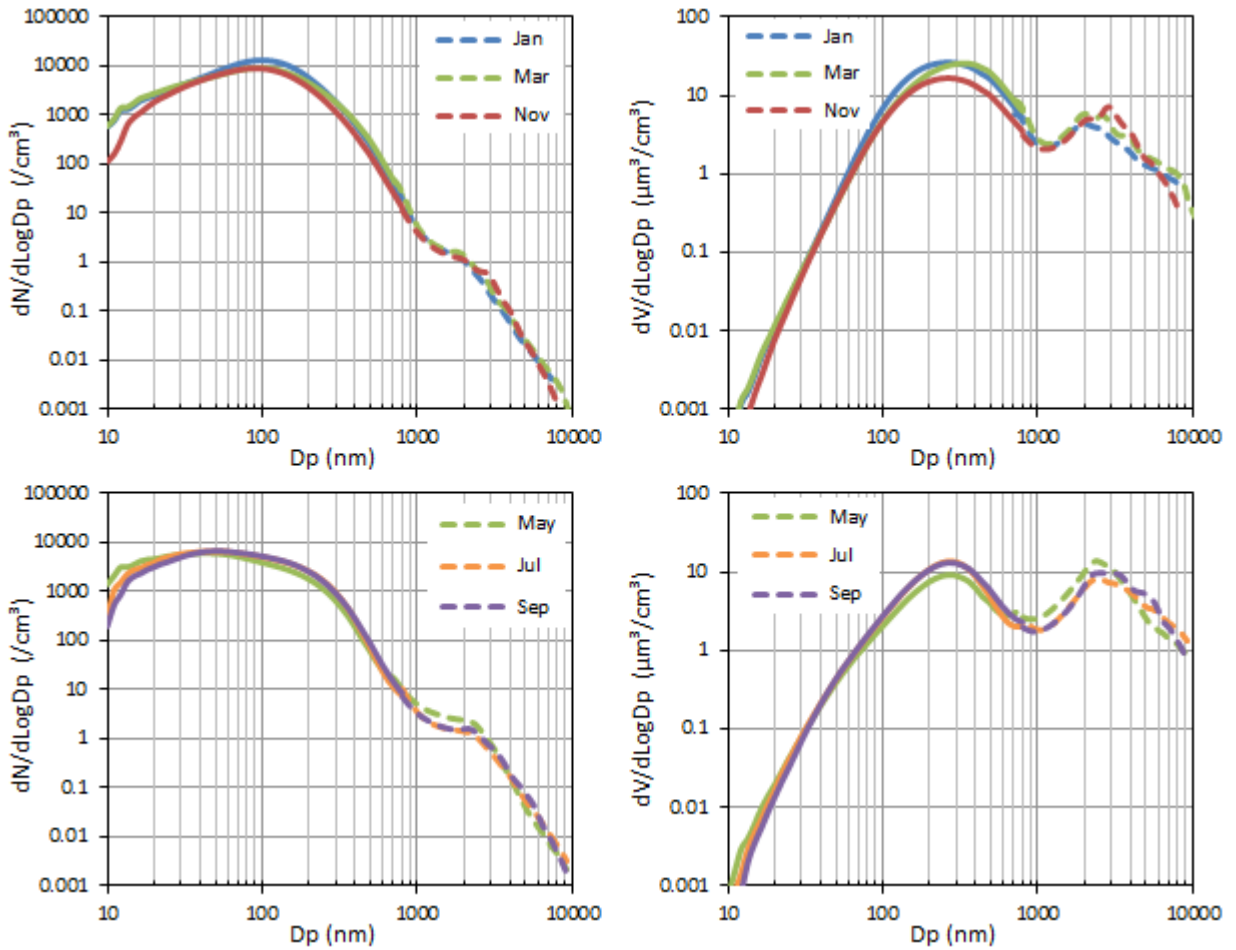


Fig. 36. Monthly mean particle number (left) and volume (right) size distributions measured in 2018 with a DMPS (10-800 nm, solid lines) and an APS (0.85-10 μm , dashed lines). Particle densities of **1.4 g cm⁻³** for cold months and **1.1 g cm⁻³** for warm months (May -Oct.) were used to convert aerodynamic to geometric diameters.

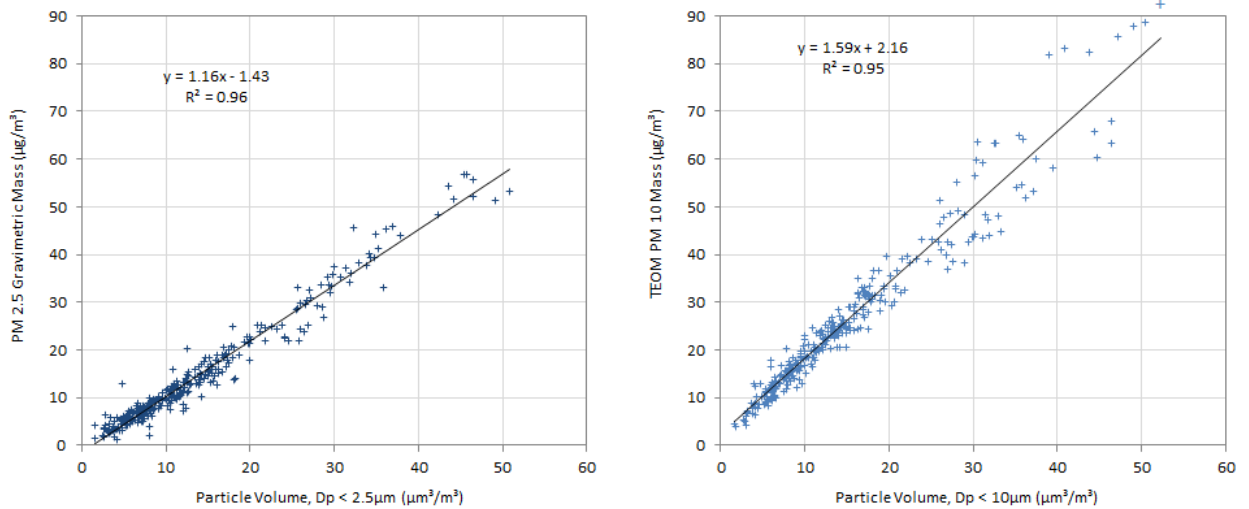


Fig. 37. 2018 regressions between (left) $\text{PM}_{2.5}$ mass concentrations determined from gravimetric measurements at 20% RH and particle volume ($D_p < 2.5 \mu\text{m}$) calculated from DMPS and APS measurements (<40% RH), and (right) between PM_{10} mass concentrations measured with the TEOM-FDMS at 30% RH and particle volume ($D_p < 10 \mu\text{m}$) at <40% RH.

Fig. 36 illustrates the large domination of sub- μm particles in the particle number size distribution. Even particle volume (and therefore PM mass) is dominated by sub- μm particles (almost half of the particle volume actually sits in particles < 300 nm). The apparent good agreement between particle number size distributions (Fig. 36) measured with the DMPS and the APS was obtained by using an aerosol density of 1.4 g cm^{-3} to convert aerodynamic diameters (measured by the APS) to mobility diameters (measured by the DMPS) for all months, except May-Oct. and Dec., where 1.1 fits better, to be compared with the range ($1.6 \pm 0.1 \text{ g cm}^{-3}$) expected for atmospheric particles (McMurry et al., 2002). Assuming that the DMSP is as accurate as it was during the calibration workshop in Jan. 2016 at the WCCAP (see [report](#)), this could be explained only by variations in the APS counting and/or sizing accuracy.

Both comparisons between PM mass and aerosol particle volume concentrations show a good correlation (Fig. 37), considering that possible variations in the aerosol density play a role in such regressions. The slope of the regression between $\text{PM}_{2.5}$ at 20 % RH and particle volume suggests a mean aerosol density of 1.16 (to be compared to 1.13, 1.12, 1.16, 1.24, 1.20, 1.31, 1.38 and 1.37 in 2017, 2016, 2015, 2014, 2013, 2012, 2011 and 2010, respectively), while the regression between PM_{10} mass and aerosol volume concentration (for $D_p < 10 \mu\text{m}$) suggests a density of 1.59, in good agreement with the nominal value of 1.5 g cm^{-3} assumed to convert aerodynamic diameters to mobility diameters for particle volume calculations. This might indicate that $\text{PM}_{2.5}$ gravimetric measurements were underestimated.

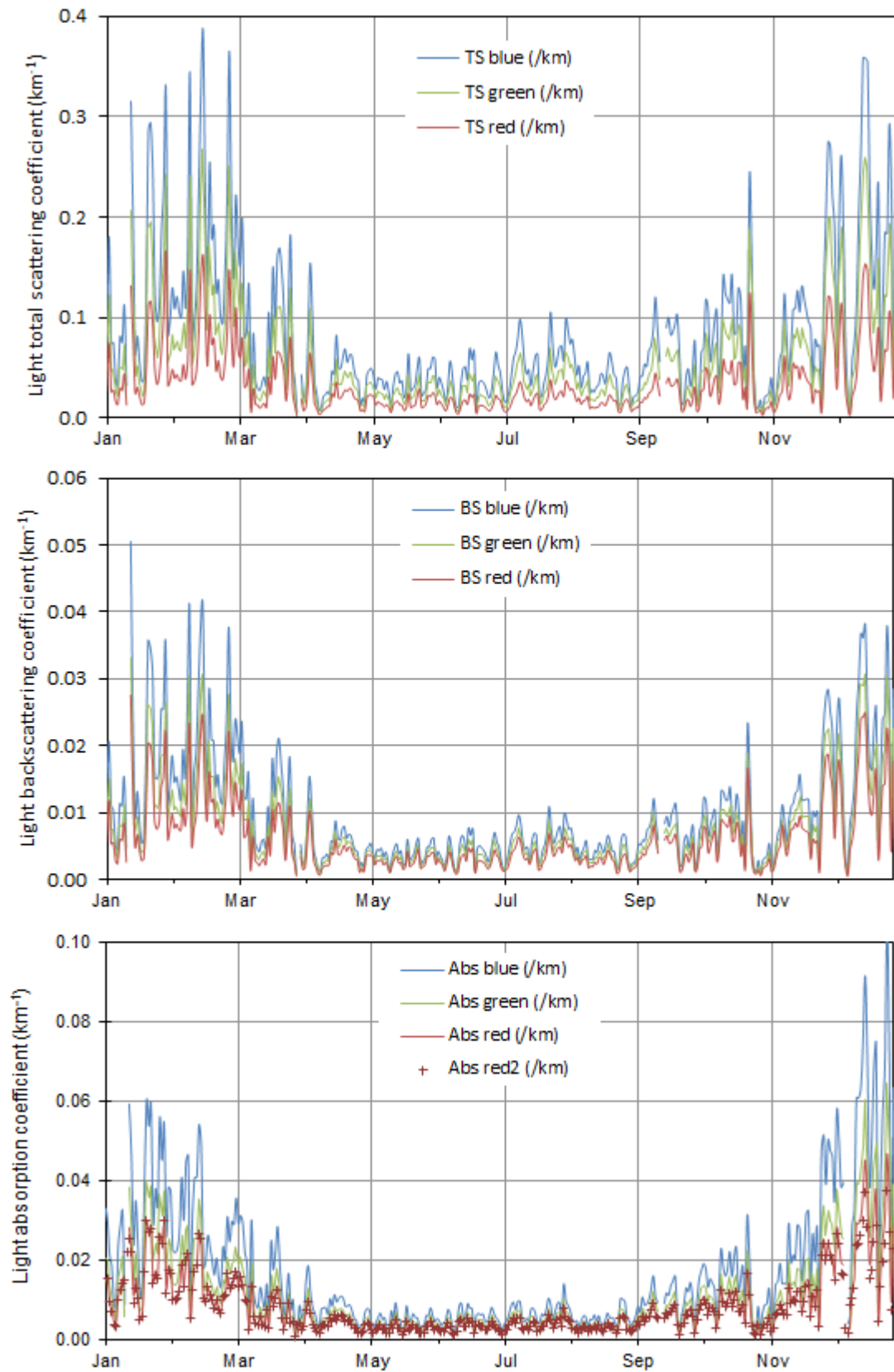


Fig. 38. Daily mean atmospheric particle light scattering (top), backscattering (middle), and absorption (bottom) coefficients at three wavelengths, derived from Nephelometer, Aethalometer and MAAP measurements (not corrected for RH) performed in 2018.

4.4.3.5 Aerosol optical properties

Aerosol particle optical properties have been monitored continuously during 2018 (data coverage = 99% for both light scattering and absorption measurements). Data from the Nephelometer (Fig. 38 a and b) have been corrected for angular non-idealities (truncation to 7 – 170°, slightly not cosine-weighted distribution of illumination) according to Anderson and Ogren (1998), but not for RH effects. Thanks to the use of a Nafion dryer and the reduction of the sampling flow rate to 6-12 L min⁻¹, the Nephelometer internal RH was maintained below 40% for 97% of the time, with exceptions (up to 47% only) occurring between May and July. At 40% RH, aerosol scattering is on average increased by about 20 % compared to 0% RH in Ispra (Adam et al., 2012).

Atmospheric particle absorption coefficients at 7 wavelengths were derived from the Aethalometer AE-31 data corrected for the shadowing and multiple scattering effects when Nephelometer data were available, according to Weingartner et al. (2003), making use of coefficients derived from Schmid et al. (2006), i.e. 3.60, 3.65 and 3.95 at 470, 520, and 660 nm, respectively (Fig. 38 c).

Both scattering and absorption coefficients follow seasonal variations (Fig. 38) in line with PM mass variations, mainly controlled by the dispersion rate of particulate pollution.

The uncertainty in the multiple scattering correction factor may introduce a quite large uncertainty in the aerosol absorption coefficient values, since correction factors ranging from 2 to 4 have been proposed (Weingartner et al., 2003; Arnott et al., 2005). The use of the correction factors listed above leads to an aerosol absorption coefficient at 660 nm slightly larger than the absorption coefficient obtained from the Multi Angle Absorption Photometer (MAAP) for 670 nm, which cannot be explained by the difference in wavelengths only (Fig. 39).

NB: in December 2015, it was recommended by ACTRIS that the coefficient 3.5 should be used for all wavelengths without any correction for the filter loading.

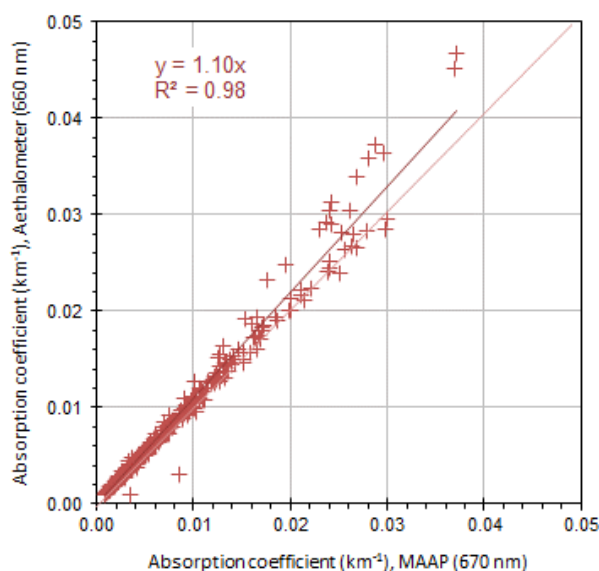


Fig. 39. Comparison between the Aethalometer and MAAP derived light absorption coefficients at 660 and 670 nm, respectively. Data points are daily averages (360) from 2018.

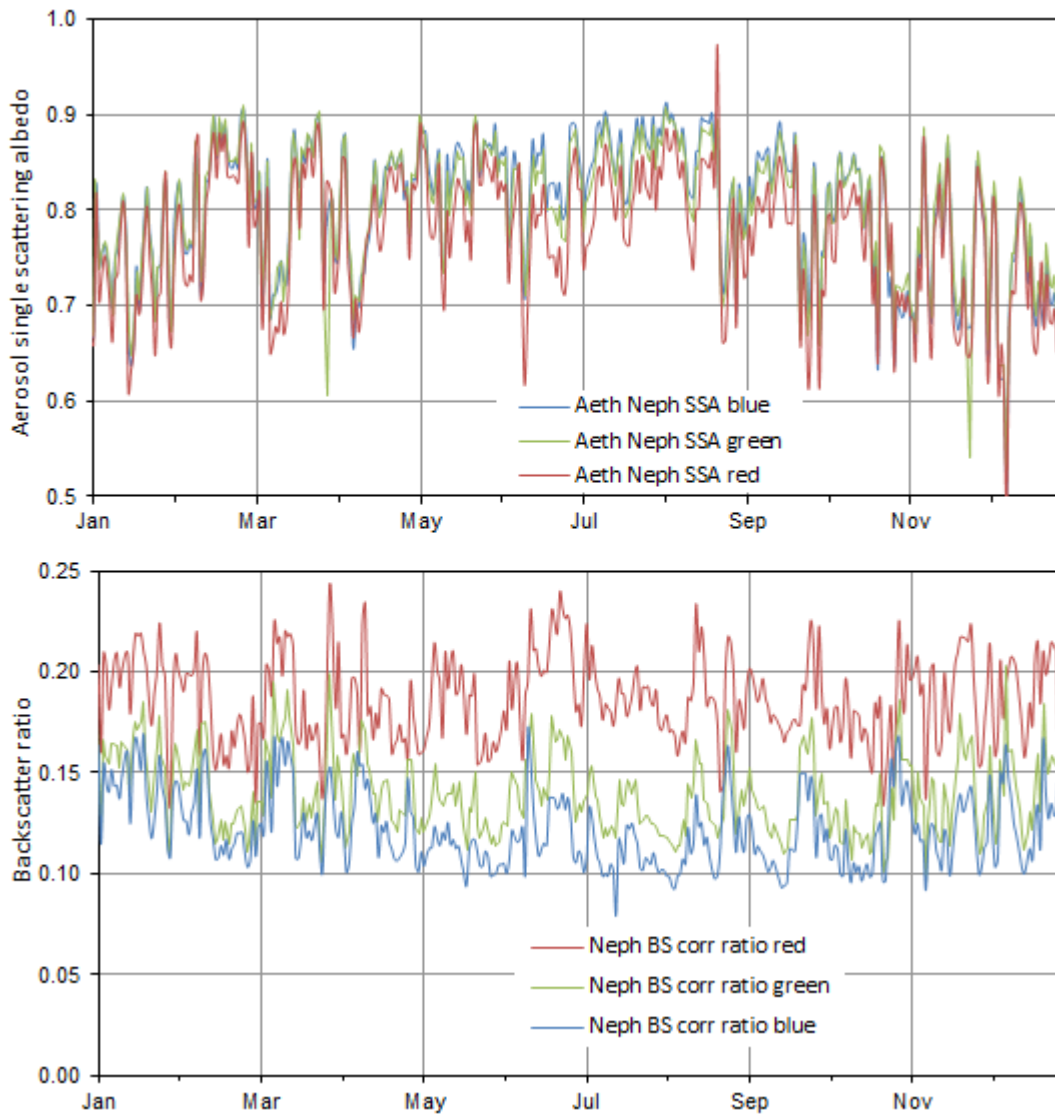


Fig. 40. Aerosol 24-hr averaged single scattering albedo and backscatter to total scatter ratio at three wavelengths corresponding to blue, green and red light, as calculated for 2018 (RH < 40%).

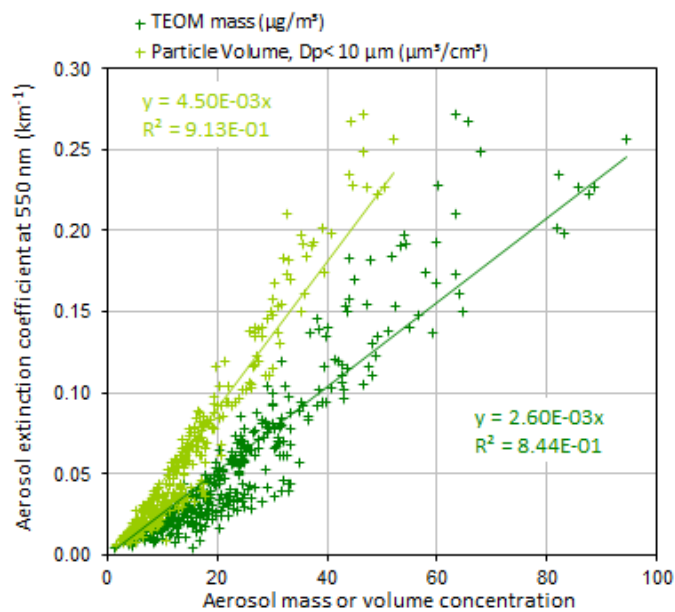


Fig. 41. Regression between the aerosol extinction coefficient and PM₁₀ mass (FDMS-TEOM) and volume (DMPS + APS) concentrations in 2018.

The 24 hr-averaged aerosol single scattering albedo (SSA) at $\lambda = 550$ nm (at RH generally < 40 %) ranged from 0.52 to 0.91 (annual average 0.80), with generally lower values in autumn and winter compared to spring and summer (Fig. 40, top). The mean SSA was higher than in 2017 (0.78), and reached similar values to 2010-2013 (0.75-0.79), when measurements were performed at the same site (Fig. 1). Excluding the values clearly affected by local influences, the mean single scattering albedo was 2% greater. The absorption coefficients were flagged for local contamination before submission to the WDCA data bank (EBAS).

The backscatter / total scatter ratio at 550 nm (Fig. 40, bottom) ranged from 0.10 to 0.20 (average 0.14), i.e. about 10% greater than in 2017, and similar to 2016 values.

The aerosol extinction coefficient and particle mass or volume concentrations are rather well correlated, although 2 branches can be observed in the regression plot (Fig. 41). The slope of the regression between extinction and mass shows that the mass extinction cross section was on average $2.6 \text{ m}^2 \text{ g}^{-1}$ in 2017 (vs 2.7 in 2017, 3.1 in 2016, 2.5 in 2015, 2.8 in 2014, and 3.4 in 2012 and 2013), i.e. very low compared with $4.6 \text{ m}^2 \text{ g}^{-1}$, the value calculated based on the aerosol mean chemical composition during 2018, and mass cross section coefficients for the various constituents found in the literature (see Table 7). Based on the particle volume determination, and assuming a mean aerosol density of 1.5 g cm^{-3} , the mass extinction cross section would be greater ($3.0 \text{ m}^2 \text{ g}^{-1}$). The agreement between these two estimates of the aerosol extinction cross section has deteriorated since 2010 – 2012, which underlines the necessity of implementing urgently new independent measurements of the light extinction (started in 2019).

Table 7: Mean aerosol chemical composition (PM_{2.5}) in 2017 and extinction cross section.

	2018 PM _{2.5} comp. (%)	σ_{ext} (m ² /g)	Reference (for σ_{ext})
“sea salt”	3	1.3	Hess et al., 1998
NH ₄ ⁺ , NO ₃ ⁻ and SO ₄ ²⁻	37	5.0	Kiehl et al., 2000
organic matter	51	3.6	Cooke et al., 1999
elemental carbon	7	11	Cooke et al., 1999
Dust	1	0.6	Hess et al., 1998
Total	100	4.6	

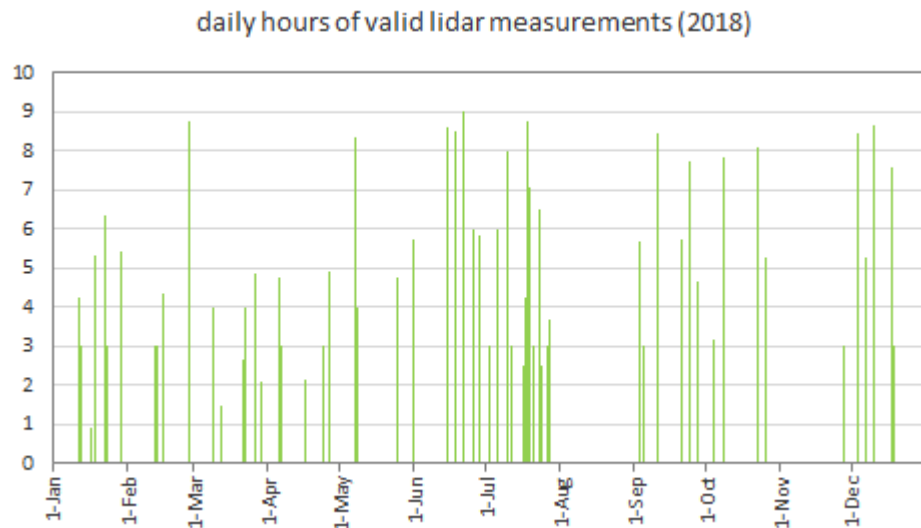


Fig. 42. Aerosol vertical profile measurements performed daily with the Raman Lidar in 2018.

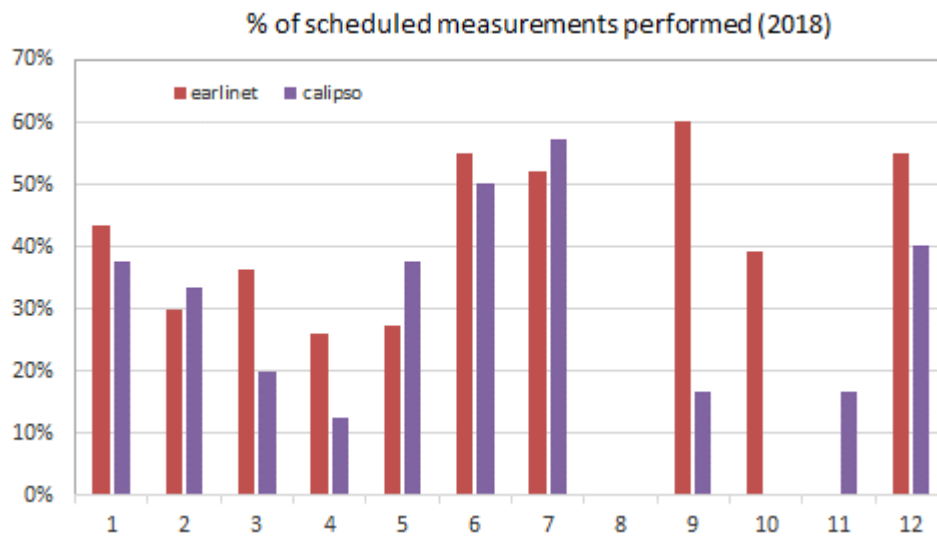


Fig. 43. Scheduled aerosol vertical profiling measurements performed monthly during the EARLINET climatology and Calipso overpass time slots in 2018.

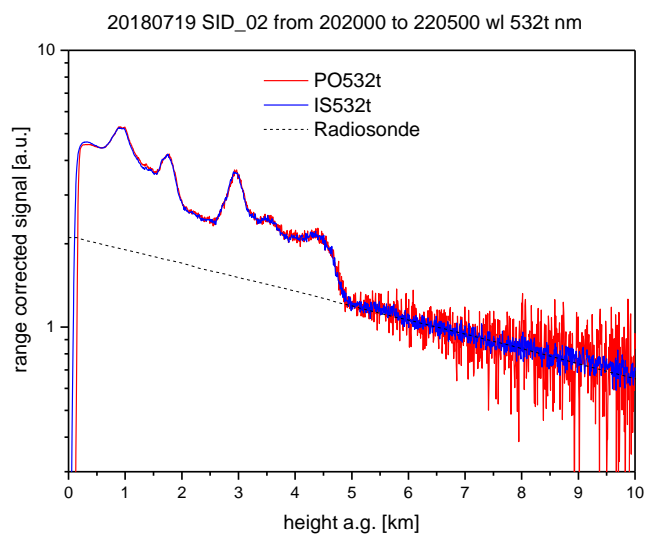


Fig. 44: Examples of results of the inter-comparison with an ACTRIS-reference LiDAR (red).

4.4.3.6 Aerosol vertical profiles

The Raman LiDAR from Raymetrics was operated for measuring aerosol vertical profiles from the atmospheric observatory (in a dedicated shelter from May 28th) during the whole of 2018, weather and staff availability permitting. It has been running since 23 May 2017 with a new reception window, and since 28 May 2018 without emission window.

In 2018, the LiDAR was operated for 302 hours (Fig. 42) vs 320 hours in 2017 and 177 hours in 2016 to fulfil the ACTRIS requirements: at noon (2 hr) and sunset (4-5 hr) on Mondays, and at sunset (4-5 hr) on Thursdays (EARLINET climatology), plus during the ESA satellite Calipso overpasses ± 1 hr (every ~ 9 days at 01:40 and 12:35 UTC). The scheduled EARLINET and CALIPSO measurements were thus covered at 35% and 27% (Fig. 43), respectively, i.e. somewhat below ACTRIS' target of 50%. This is mainly due the fact that the LiDAR cannot be run automatically and currently only 1 operator is qualified to operate it.

Measurements' quality has certainly improved since the emission window has been removed (28 May 2018), and data since then at least could be processed using the ACTRIS-EARLINET Single Calculus Chain (SCC) without further instrument characterisation needs. However, due to expected improvements in the SCC, and in the process for submitting data to the EARLINET data base (completed in October 2019), only a limited amount of 2018 data were processed, and none was submitted yet.

The LiDAR was compared with a reference ACTRIS instrument at the atmospheric observatory in Ispra during the period 17-27 July 2018. This inter-comparison demonstrated the good performance of our LiDAR, and the need for checking operational parameters (like the "zero bins" and the depolarisation calibration constant). Fig. 44 shows an example of the inter-comparison results showing the good agreement with the reference instrument (PO) for the elastic signal (532t), an overestimation of the depolarisation (532c), and an underestimation of the Raman signal (387) below 1 km.

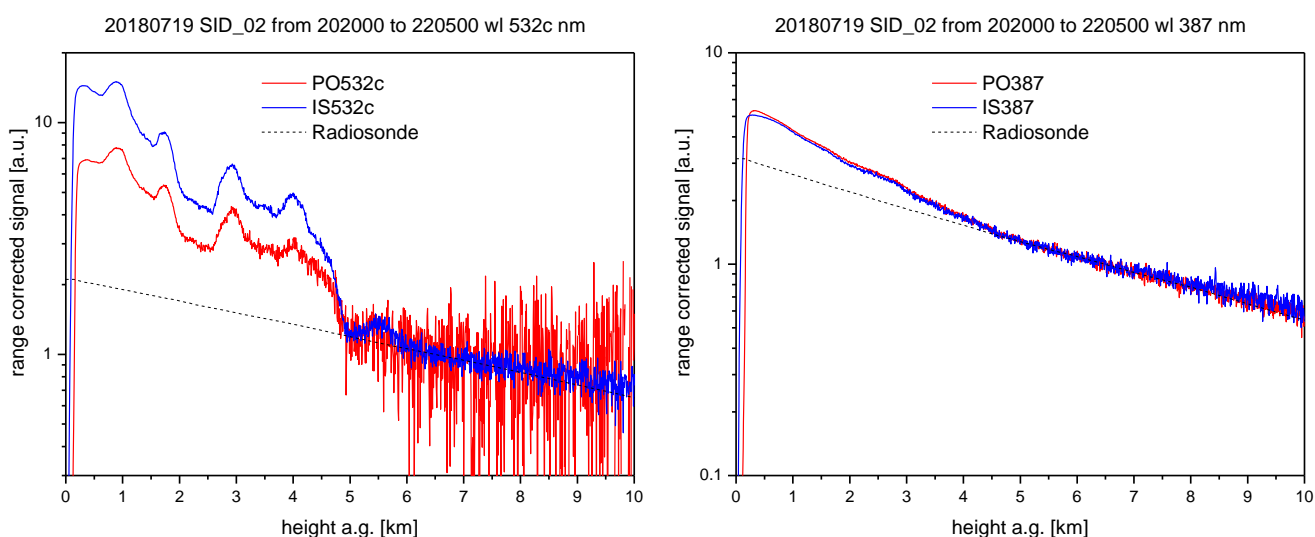


Fig.44: (cont'd): Examples of results of the inter-comparison with an ACTRIS-reference LiDAR (red) on 19 July 2018 (20:20-22:05 UTC).

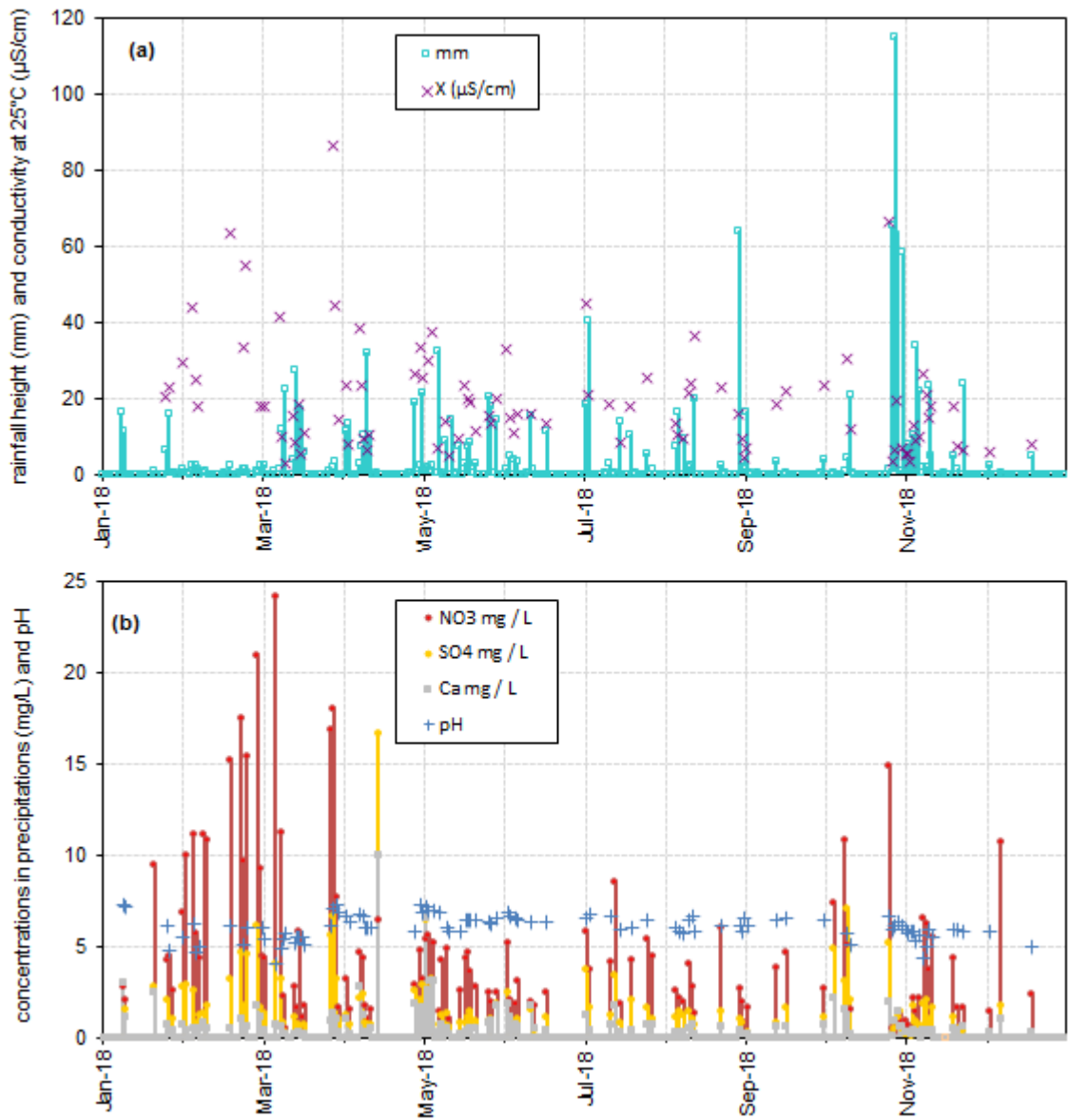


Fig. 45 (a) Precipitation amount, conductivity and (b) concentrations of 3 major ions in precipitation (bars) and pH (crosses) in 2018, and during the 1990-99 period (line).

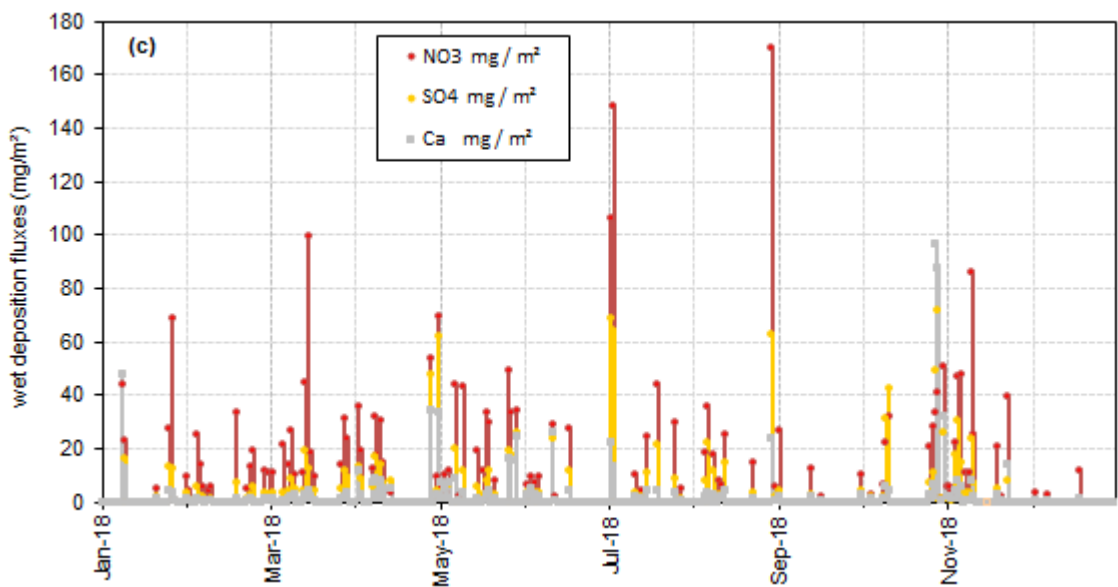


Fig. 46. Wet deposition fluxes of 3 main ions measured in rain water in 2018.

4.4.4 Wet deposition chemistry

In 2018, 135 precipitation samples were collected, i.e. 50 more than in 2017 (dry year) but similar to previous years. The ionic content, acidity (pH) and conductivity were measured in 117, 98 and 95 of these samples (those where the water volume was sufficient minus 3 major events). The precipitation height measured during the collected events ranged from 0.05 to 115 mm (Fig. 45a) for a total of 2400 mm (top record since 1986).

The ranges of concentrations measured in these samples are indicated in Table 8. Volume weighted mean concentrations of the anthropogenic species NO_3^- and SO_4^{2-} were lower in 2018 than the 1990-2010 averages in 2018, the concentration of and NH_4^+ was equal, while concentrations of all the marine and crustal components were similar to the long-term average. Fig. 45b shows that all but 7 precipitation samples collected in 2018 were acidic (pH < 7.0), and 21 had a pH < 5.6 (equilibrium with atmospheric CO_2), compared to 24 in 2017, 25 in 2016, 43 in 2015, and 58 in 2014. Amongst those, only 2 samples had a pH < 4.6 (compared to 9 in 2017, 3 in 2016, 18 in 2015, and 9 in 2014 and 2013).

Wet deposition was quite evenly distributed over the year, but almost no wet deposition occurred in January while November was extremely wet (Fig. 45). In 2018, the annual wet deposition flux of the main acidifying and eutrophying species was 1.3, 2.7 and 1.3 g m^{-2} for SO_4^{2-} , NO_3^- , and NH_4^+ , respectively, i.e. about 10% less than in 2017 but 10% more than in 2016 (see also section 4.6 next page).

Table 8: Statistics relative to the precipitation samples collected in 2018 (averages are volume weighted), compared to long-term averages.

	pH	cond. $\mu\text{S cm}^{-1}$	Cl ⁻ mg l^{-1}	NO_3^- mg l^{-1}	SO_4^{2-} mg l^{-1}	Na ⁺ mg l^{-1}	NH_4^+ mg l^{-1}	K ⁺ mg l^{-1}	Mg ²⁺ mg l^{-1}	Ca ²⁺ mg l^{-1}
Average	5.64	13.8	0.35	2.85	1.01	0.22	1.28	0.06	0.05	0.48
Min	4.06	2.73	0.05	0.29	0.09	0.02	0.06	0.00	0.01	0.09
Max	7.28	86.4	8.1	24.1	16.6	4.9	8.4	0.83	0.59	10.0
1990-2010	4.58	24.7	0.40	3.75	2.44	0.25	1.28	0.09	0.06	0.40

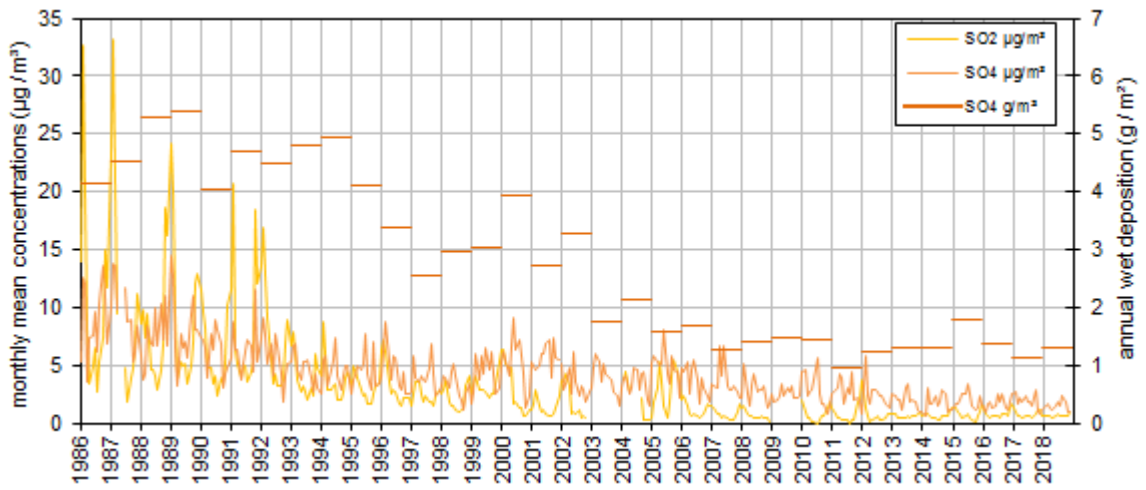


Fig. 47. Oxidised sulphur species monthly mean concentrations and yearly wet deposition.

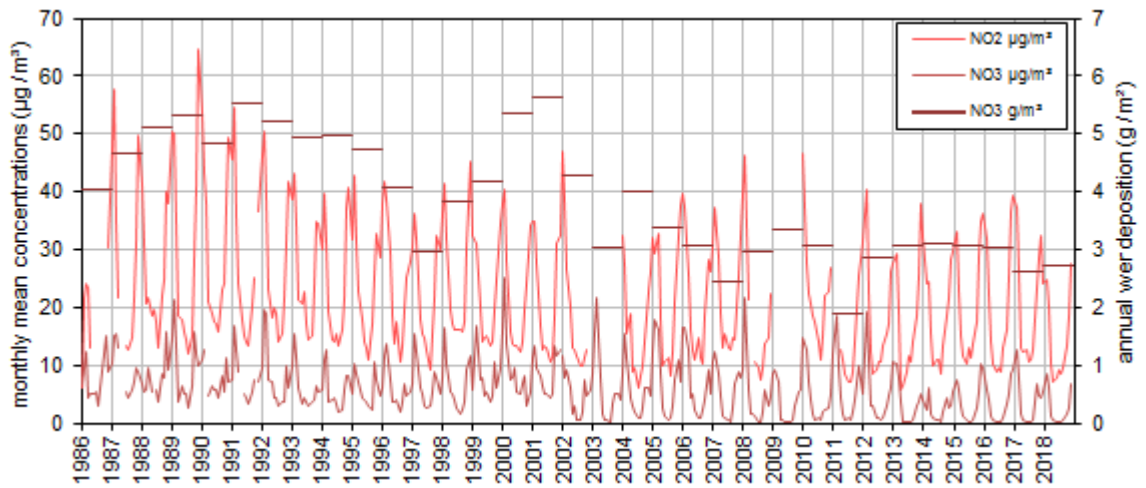


Fig. 48. Oxidised nitrogen species monthly mean concentrations and yearly wet deposition.

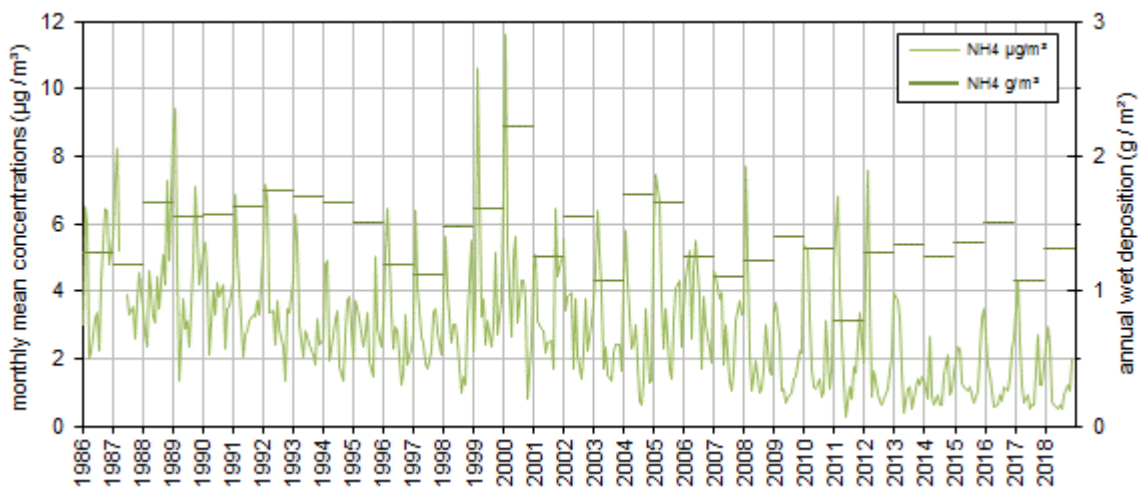


Fig. 49. Reduced nitrogen species monthly mean concentration and yearly wet deposition.

4.5 Results of year 2018 in relation to 30+ years of measurements

4.5.1 Sulphur and nitrogen compounds

The annual mean SO₂ concentration in 2018 (0.6 µg/m³) was slightly 25% lower than in 2017, but still in line with the range of values (0.6 – 0.8 µg/m³) observed at our station in the 2010's. SO₂ concentrations are nowadays ~10 times smaller than in the 90's, and less than half compared to the 2000's (Fig. 47). The annual mean particulate SO₄²⁻ concentration (1.5 µg/m³) reached a historical minimum in 2018, 20% less than the average observed over the 3 previous years, 60% less compared to the 2000's. It should be kept in mind that SO₄²⁻ concentrations were measured in PM₁₀ or in PM_{2.5} from 2002 onwards, whereas it was measured in TSP (Total Suspended Particulate) from 1986 to 2001. However, simultaneous sampling of PM₁₀ and TSP over 14 months showed that SO₄²⁻ in PM₁₀ is generally less than 5 % lower than in TSP. SO₄²⁻ is mainly present in the PM_{2.5} fraction at our site (see Fig. 24 of the ABC-IS annual report 2010). From 2005 onwards the calculations were as follows:

$$\text{SO}_4^{2-}(\text{PM}_{10}) = \text{SO}_4^{2-}(\text{PM}_{2.5}) \times \langle \text{SO}_4^{2-}(\text{PM}_{10}) / \text{SO}_4^{2-}(\text{PM}_{2.5}) \rangle$$

the average $\langle \text{SO}_4^{2-}(\text{PM}_{10}) / \text{SO}_4^{2-}(\text{PM}_{2.5}) \rangle$ being calculated based on the simultaneous PM₁₀ and PM_{2.5} samples collected in 2010-2012.

Particulate SO₄²⁻ concentrations decreased much less than SO₂ concentrations, which suggests that locally produced SO₂ decreased much more than possibly long-range transported SO₄²⁻ over the past 25-30 years. SO₄²⁻ wet deposition in 2018 was amongst the 6 lowest on record despite rainfalls larger than usual, and 10% less than over the past 3 years (Fig. 47). The low SO₂ and SO₄²⁻ concentrations and the not that low SO₄²⁻ wet deposition can be related to the high precipitation amount observed in 2018.

In 2018, the annual mean NO₂ concentration was amongst the 3 lowest observed since 1986, and 20% less compared to the 2000's (Fig. 48). Both wintertime maxima and summertime minimum were amongst the lowest measured over the past decade. However, monthly mean concentrations of nitrogen dioxide (NO₂) do not show as much of a pronounced decreasing trend as seen for SO₂ over the past 30 years (Fig. 47), and do not reflect the abatement in NO_x emissions reported in the emission inventories for this period. The particulate NO₃⁻ annual mean concentration observed in 2018 was also 20% less than during the past 3 years, and 50% less than in the 2000's. It should be noted that since October 2000, NH₄⁺ and NO₃⁻ have been measured from quartz fibre filters, which are known to lose NH₄NO₃ at temperatures > 20 °C, as demonstrated e.g. by the comparison with the ACSM measurements we performed in Ispra in 2013. This might contribute significantly to the low summertime minima NO₃⁻ seen since 2002. Furthermore, NO₃⁻ was measured from PM₁₀ or in PM_{2.5} from 2002, and no more from TSP, as over the 1986 to 2001 period. However, simultaneous sampling of PM₁₀ and TSP over 14 months showed that NO₃⁻ in PM₁₀ is generally less than 5 % lower than in TSP, like SO₄²⁻. From 2005 and onwards the calculations were as follows

$$\text{NO}_3^-(\text{PM}_{10}) = \text{NO}_3^-(\text{PM}_{2.5}) \times \langle \text{NO}_3^-(\text{PM}_{10}) / \text{NO}_3^-(\text{PM}_{2.5}) \rangle$$

the average $\langle \text{NO}_3^-(\text{PM}_{10}) / \text{NO}_3^-(\text{PM}_{2.5}) \rangle$ being calculated based on the simultaneous PM₁₀ and PM_{2.5} samples collected in 2010-2012. The NO₃⁻ wet deposition annual flux observed in 2018 was the 3rd lowest recorded since 1986 in Ispra (despite the large amount of precipitation), and 6% less than the average over the 3 past years (Fig. 47).

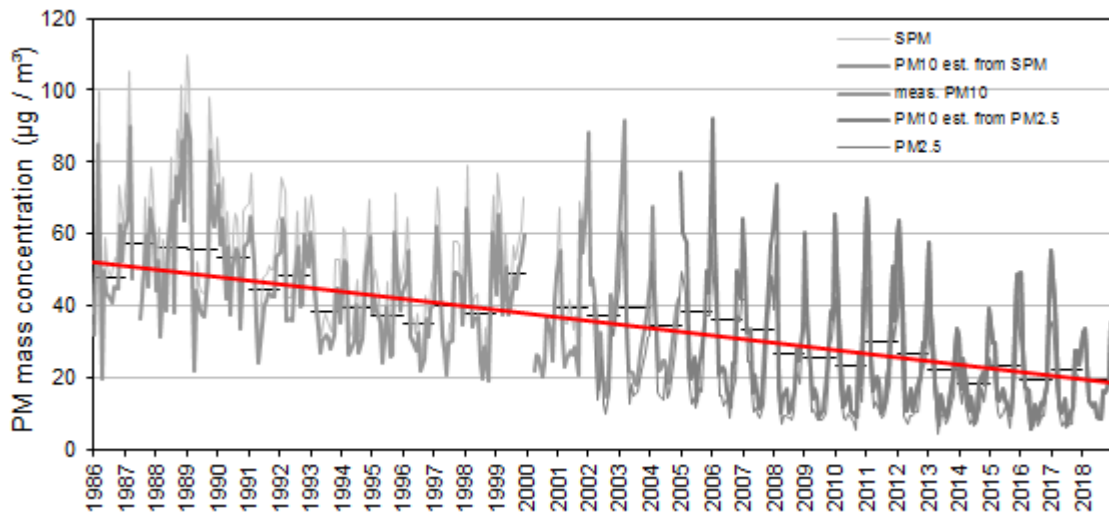


Fig. 50. Particulate matter mass concentration monthly (grey) and annual (black) averages. The red line is the long term trend over annual averages. All values are gravimetric measurements or estimates from gravimetric measurements.

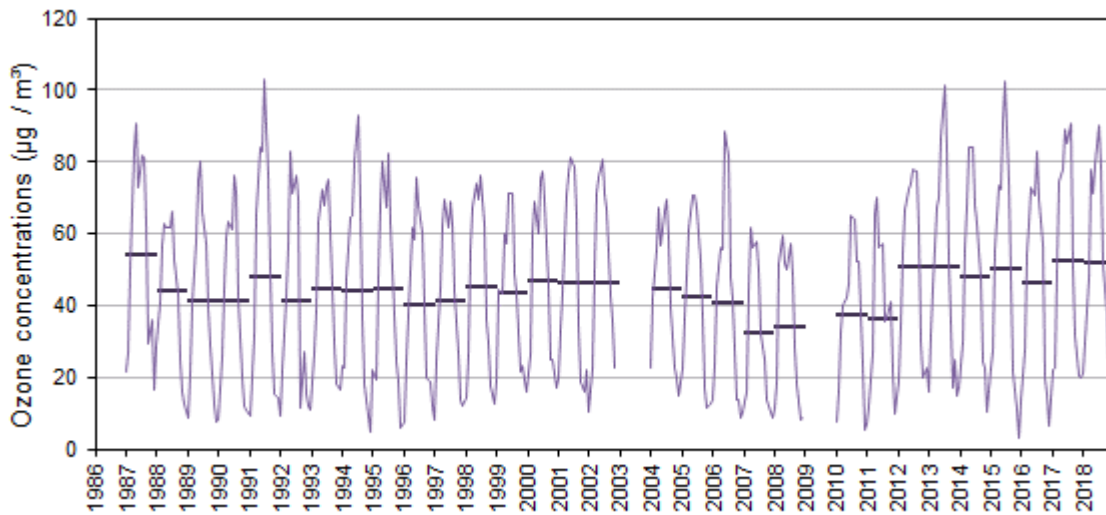


Fig. 51. Ozone yearly and monthly mean concentrations.

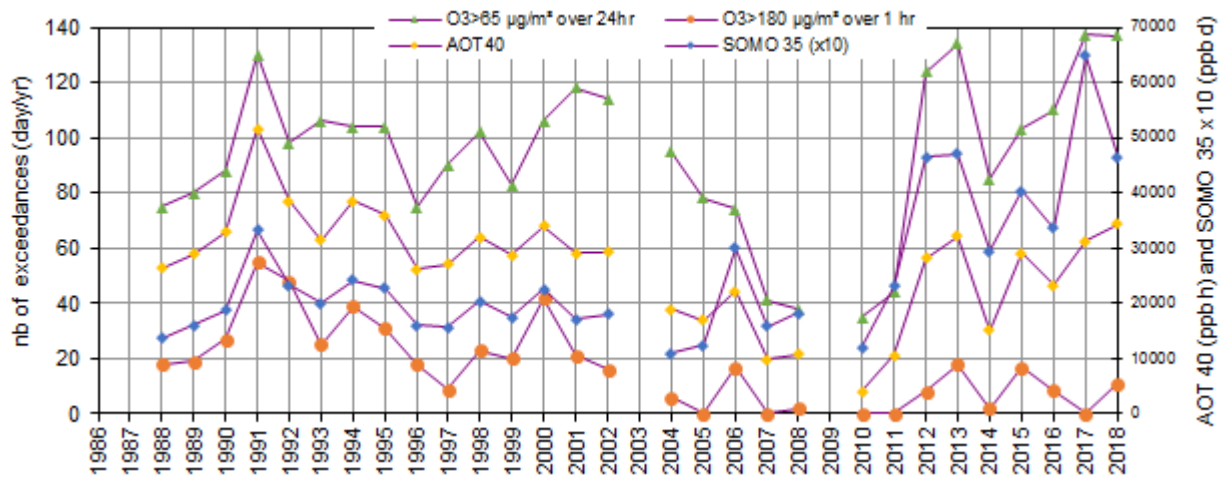


Fig. 52. Number of O₃ limit value exceedances (days) and AOT40 and SOMO35 values.

The annual mean concentration of NH_4^+ in particulate matter was in 2018 also 20% less than the average over the 3 past years in (Fig. 49), and 60% less compared to the previous decade. It should be noted that from the year 2002, NH_4^+ was measured in the PM_{10} or in the $\text{PM}_{2.5}$ fraction. From 2005 and onwards, NH_4^+ concentrations in PM_{10} were calculated as follows:

$$\text{NH}_4^+(\text{PM}_{10}) = \text{NH}_4^+(\text{PM}_{2.5}) \times \langle \text{NH}_4^+(\text{PM}_{10}) / \text{NH}_4^+(\text{PM}_{2.5}) \rangle$$

where the average $\langle \text{NH}_4^+(\text{PM}_{10}) / \text{NH}_4^+(\text{PM}_{2.5}) \rangle$ is calculated based on simultaneous PM_{10} and $\text{PM}_{2.5}$ measurements performed in 2010-2012. On average, NH_4^+ can neutralise nearly 100% of the acidity associated with NO_3^- and SO_4^{2-} in the particulate phase (see Fig. 31). NH_4^+ is also quite well correlated with $\text{NO}_3^- + \text{SO}_4^{2-}$ in rainwater. NH_4^+ annual wet deposition in 2018 was equal to the previous 3 year-average, and close to 10% less than the average recorded in Ispra in the 2000's (Fig. 49).

4.5.2 Particulate matter mass

The 2018 annual mean $\text{PM}_{2.5}$ concentration measured at 20% RH ($14.2 \mu\text{g}/\text{m}^3$) reached the second lowest value after 2014 ($13.1 \mu\text{g}/\text{m}^3$), and was 40% less than in the 2000's. The annual value for PM_{10} at 50% RH estimated from $\text{PM}_{2.5}$ measurements is therefore in line with the general decreasing trend of $-1.0 \mu\text{g m}^{-3} \text{ yr}^{-1}$ over the 3 last decades (Fig. 50). It should however be kept in mind that PM_{10} concentrations were estimated from TSP mass concentration measurements (carried out by weighing at 60 % RH and 20 °C cellulose acetate filters sampled without any particle size cut-off and "dried" at 60 °C before and after sampling) over 1986-2000, based on a comparison between TSP and PM_{10} over the Oct. 2000 - Dec. 2001 period ($R^2 = 0.93$, slope = 0.85), and derived from measured $\text{PM}_{2.5}$ values for years 2005-2018. The increasing trend in winter concentrations observed since 2015 (at least partly due to the exceptionally dry Dec. 2015, Jan. and Dec 2016, and Jan. 2017) have stopped in 2018. Summertime PM minima showed a clear decreasing trend over 1986 – 2013, but have remained fairly constant since then.

4.5.3 Ozone

Fig. 51 shows monthly and yearly mean O_3 concentrations observed since 1987. Ozone was not measured in 2009 and there was a major data acquisition breakdown in 2003. Annual average O_3 concentrations have been consistently high from 2012. In 2018, the annual mean O_3 concentration only slightly decreased compared to 2017, and reached the 3rd highest record since the measurements started in 1987. This high annual average was due to high wintertime background values and only moderately high summer values, like in 2017. Ozone indicators for 2018 (Fig. 52) show a comeback of extreme O_3 pollution events (11 days with O_3 1hr-peak concentration above the limit value of $180 \mu\text{g}/\text{m}^3$), and numerous occurrences of concentrations greater than 35-40 ppb ($70\text{-}80 \mu\text{g}/\text{m}^3$).

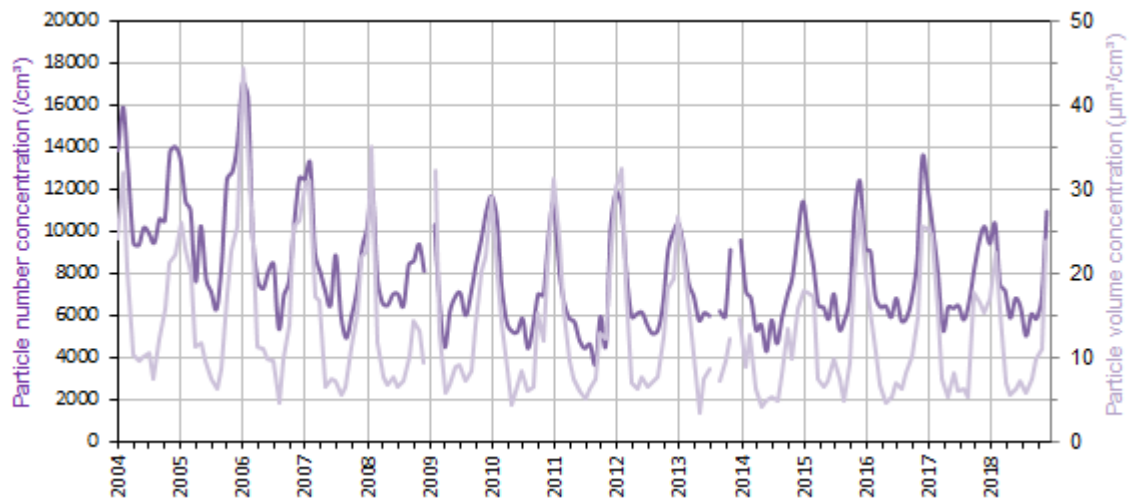


Fig. 53. Particle number (left) and volume (right) monthly mean concentrations.

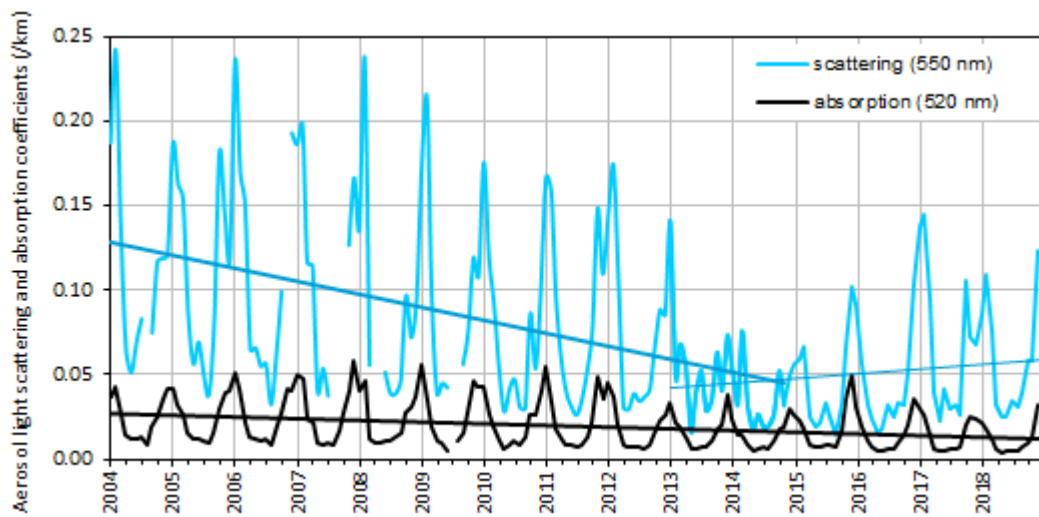


Fig. 54. Aerosol green light scattering and absorption monthly mean coefficients

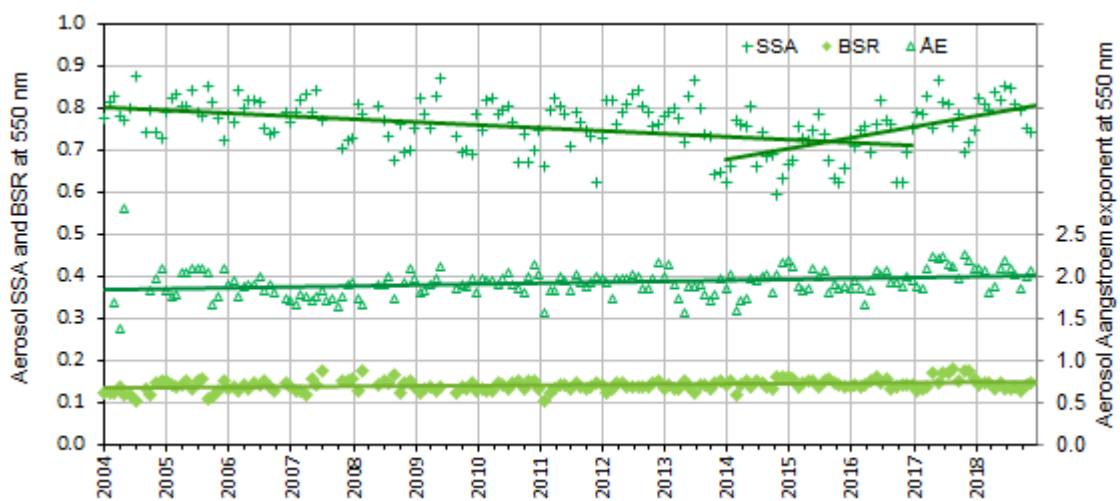


Fig. 55. Aerosol optical characteristics at 550 nm (monthly means): single scattering albedo and backscatter ratio (left hand axis) and scattering Ångström exponent (right hand axis).

Both indicators for the vegetation protection (number of days with a 24-hour mean O₃ concentration > 65 µg/m³, vegetation protection limit, and the AOT40, Accumulated Ozone exposure over a Threshold of 40 ppb) have generally been increasing during the 2010's and now reached levels similar or greater than the values observed in the 1990's after the minimum observed in the 2000's (Fig. 52). The population exposure indicator SOMO 35 (Sum of Ozone Means Over 35 ppb, where means stands for maximum 8-hour mean over day) was less than in 2017, but still comparable to the highest levels ever observed since 1987 (Fig. 52).

4.5.4 Aerosol micro-physical and optical properties

Measurements of aerosol microphysical properties started at the atmospheric research station of the JRC-Ispira in 2004, which represents one of the longest time series for this kind of measurements across Europe.

After the decreasing trend observed in sub-µm aerosol particle number and volume concentrations observed between 2004 and 2011, the annual average of both variables had started to increase since 2014, but 2018 concentrations dropped to reach values close to their historical minimum (Fig. 53), specially for wintertime values.

These trends are reflected in the long-term variations of the aerosol light scattering coefficient (Fig. 54), which is sensitive to both the number and size of atmospheric particles. In contrast, the aerosol light absorption coefficient still decreases slowly, both in summer and winter. As a consequence, the aerosol single scattering albedo (SSA = scattering/(scattering + absorption)) significantly decreased between 2004 and 2015, and seems to be increasing again since then. The Ångström exponent (which increases with decreasing particle diameters) has perhaps been increasing faster since 2015 (Fig. 55), but longer time series are needed to confirm this trend or not. The aerosol backscatter ratio also seems to increase, but this trend is significantly affected by the high values observed in 2017. These variations are good for climate change mitigation since the impact of these recent changes is an increase of the direct cooling effect by atmospheric particles at the top of the atmosphere, in contrast to what we observed between 2004 and 2012 (Putaud et al., 2014).

4.6 Conclusions

Measurement of short-lived pollutants and climate forcers were carried out continuously in 2018 at 9 m agl at the new atmospheric observatory (Fig. 1). Data coverage was better than 97% for all instruments measuring near surface variables but one (the APS measuring aerosol particle size distributions above 800 nm). The remote aerosol vertical profiler was operated for the whole year, weather and staff availability permitting, and covered close to 35% of the scheduled measurement slots.

2018 as a whole was warmer and sunnier compared to the reference period (1990 – 2010), specially from April to October, but also very wet, due to exceptional rainfalls in November. Inter-annual variations in weather conditions can significantly affect trends in short-lived atmospheric species.

However, the warm and sunny conditions occurring from spring to autumn are probably not sufficient to explain the high O₃ concentrations and exposure indicators observed in 2018, which generally did not improve, in line with the trend observed since 2010. It would be worth investigating if such a feature can be observed in the time series obtained at air monitoring stations in our area.

In contrast, the annual mean concentrations of SO₂, NO₂ and CO were less than during the previous years, and confirm the general trend of improvement in these air quality indicators over the last 3 decades.

Daily PM_{2.5} aerosol sampling on quartz fibre filter through a carbon monolith denuder, and subsequent gravimetric and chemical analyses, showed that the concentration of PM_{2.5} mass and of most of its components (SO₄²⁻, NO₃⁻, NH₄⁺, POM and EC) significantly decreased in 2018 compared to 2017, and reached levels close to their historical minima. PM_{2.5} average chemical composition was dominated by carbonaceous species (POM: 44%, EC: 6%), followed by secondary inorganics (NH₄⁺: 8%, NO₃⁻: 12%, SO₄²⁻: 12%). It is worth mentioning that in 2018 the unaccounted mass averaged 14%. This value mainly comes from days where PM mass concentrations are low, but excludes days where PM_{2.5} concentration was less than 3 µg / m³, for which uncertainties are too big. As previously observed, there was a clear increase of NO₃⁻ contribution to PM_{2.5} when shifting from cleaner (3 < PM_{2.5} < 10 µg/m³) to more polluted periods (PM_{2.5} > 25 µg/m³) during both cold and warmer months. PM_{2.5} (from gravimetric analyses at 20% RH) annual mean mass concentrations (14 µg/m³) was well below the EU annual limit value (25 µg/m³). In contrast, PM₁₀ measurements performed with the FDMS-TEOM led to 28 exceedances of the daily limit value (50 µg/m³), while the annual average (25 µg/m³) stayed below the annual PM₁₀ limit value (40 µg/m³). The long-term time series of PM concentrations still suggests a decreasing trend of - 1.0 µg m⁻³ yr⁻¹ over the last 3 decades.

Particle number size distributions were in 2018, as usual, generally broadly bimodal, with a submicron mode at ca. 100 nm (dry) and a less pronounced coarse mode around 2 µm. The annual mean particle number concentration (average: 7300 cm⁻³) was less than during the 3 previous years. The increase in particle number concentration observed since 2014 (following a net decrease till 2011) therefore stopped. These trends are reflected in several other variables like the aerosol light scattering coefficient, and as a consequence, the aerosol single scattering albedo (0.80 in 2018, 0.78 in 2017 vs 0.72 in 2016 and 0.70 in 2015). It can also be observed in PM mass concentrations, of which wintertime maxima have stopped to increase in 2018.

All the aerosol extensive variables measured at the atmospheric observatory of Ispra (a few meters above ground level) have similar seasonal variations with summer minima. These variables are generally well correlated and lead to variable degrees of chemical, physical, and optical closure. In 2018, a reasonable overlap between the particle size distributions as measured with the DMPS and the APS was obtained for a particle density ranging between 1.1 and 1.4 g/cm³. These values are reasonably consistent with the average sub-2.5 µm aerosol

density of 1.16 g/cm^3 determined from the regression between the gravimetric $\text{PM}_{2.5}$ mass and the DMPS + APS volume. However, such a density is low compared to literature values (1.6 ± 0.1), and is also low compared to 2010 - 2012 values ($1.3 - 1.4 \text{ g/cm}^3$). In contrast, the ratio between the PM_{10} mass concentration measured with the FDMS-TEOM and the aerosol volume DMPS + APS volume leads to a density of 1.6 g/cm^3 . It is unlikely that the density of PM_{10} and $\text{PM}_{2.5}$ are so different from each other. This difference might indicate a systematic bias in one of these measurements in 2018, as during previous years. Similarly, the mean mass extinction cross section (i.e., the extinction-to-mass ratio) of 2.6 to $3.0 \text{ m}^2 \text{ g}^{-1}$ (depending on the measurements used to calculate this variable) obtained in 2018 is low compared to the value that can be calculated from the mean $\text{PM}_{2.5}$ chemical composition ($4.6 \text{ m}^2 \text{ g}^{-1}$), which suggests that either the aerosol volume and PM_{10} concentrations were overestimated, or the extinction coefficient calculated as scattering + absorption was underestimated. The measurement of light scattering and absorption by atmospheric particles remain challenging and prone to uncertainties. The direct measurement of the aerosol light extinction started in 2019 will be very useful to address this issue.

Aerosol vertical profiles were obtained with the Raymetrics Raman LiDAR for the whole of 2018. Mainly due to unsuitable meteorological conditions and staff unavailability, about 35% only of the profiles scheduled by ACTRIS could be measured. Data have been only partially processed using the ACTRIS Single Calculus Chain due to the need for re-determining some of the instrument characteristics. Therefore no optical products have been submitted to the ACTRIS/EARLINET data bank for 2018.

The concentrations of the ions measured in rainwater (Cl^- , NO_3^- , SO_4^{2-} , Na^+ , NH_4^+ , K^+ , Mg^{2+} , and Ca^{2+}) were in 2018 all less than in 2017, at least partly due to the amount of precipitation (2400 mm) much larger than in 2017 (804 mm). Indeed, the annual wet deposition fluxes of the main acidifying and eutrophying species (1.3 , 2.7 , and 1.3 g m^{-2} for SO_4^{2-} , NO_3^- , and NH_4^+ , respectively) was larger than in 2017, but 10 to 40% less than during the 2000's. Only 2 rain samples with $\text{pH} < 4.6$ (i.e. 10 times more acidic than due to the equilibrium with atmospheric CO_2) were collected in 2018 (historical low record). Rainwater acidity has indeed drastically dropped over the past 3 decades.

In-situ 2018' data listed by [EMEP](#) and [ACTRIS](#) as core variables have all been reported to [EBAS](#) by July 2019. They can be freely downloaded from these data centres.



Fig. 56: the flux tower of 24 m at the Pinus pinea site in San Rossore

5. Atmosphere – Biosphere flux monitoring at the forest station of San Rossore

5.1 Location and site description

The measurement site 'San Rossore' (43°43.9205'N, 10°17.45817' E, 4 m a.s.l.), operated by the Air and Climate Unit, is located in the Tenuta di San Rossore, inside the Parco Regionale Migliarino, San Rossore, Massaciuccoli (www.parcosanrossore.org), approximately 9 km west of Pisa and 1200 m east of the seashore in a Mediterranean forest ecosystem. The Climate Change and Air Quality Unit began to operate the predecessor site in the Parco San Rossore in 1999; the present location is running since 2013 in the same area, few hundreds of meters NorthEastward compared to the initial location.

The measurement site is situated in an almost flat area with a morphology characterised by the presence of sandy dunes. The vegetation in the direct vicinity is a pinewood plantation established in 1921 following artificial seeding. It is dominated by the evergreen species stone pine (*Pinus pinea* L.), with very sparse presence of black alder (*Alnus glutinosa* L.), white poplar (*Populus alba* L.), field elm (*Ulmus minor* Mill.), narrow-leaved ash (*Fraxinus angustifolia* L.) and holm oak (*Quercus ilex* L.), also known as evergreen oak. The average canopy height is approximately 19m, whereas the needles start at about 16.5 m. The understory vegetation is confined to the forest edges or canopy gaps and is very sparse. A remarkable feature of the plantation is the presence of narrow and long bands of soils with well watered conditions, mostly stretched from North to South and at their very far end hedging Southwestward, toward the shore. They're called "lame" and they're markedly different from the rest of the pinewood forest for flora, fauna and edaphic properties. Almost all the secondary species are indeed confined in these relatively quite small portions of the forest.

The area has a Mediterranean – type climate within the sub-humid zone, with a mean annual rainfall of 876 mm yr⁻¹ and a range of 534 – 1270 mm for the period 1980 – 2005. The long-term data were obtained from a meteorological station located at a distance of approximately 10 km and managed by the Regional Hydrologic Service of Tuscany. Rain falls mainly during autumn and winter with about 50% occurring between September and November, while the driest months are July and August. Water table is normally shallow compared to most of the ecosystem in the same climatic zone and, together with the presence of the above mentioned "lame", makes the water availability to the tree roots higher than in common Mediterranean forests. The average annual temperature is approximately 14.2 °C with the average temperature of the coldest month (January) being 7 °C and that one of the warmest month (August) being 25 °C. The wind regime is characterized by a sea – land breeze circulation, i.e. the air flows quite predictably from the west (sea) during the day and from east (land) during the night.

Table 9: ICOS class 2 Ecosystem Station core parameters.

Core variables continuous	Core variables daily to monthly	Core variables yearly
CO ₂ , H ₂ O and energy fluxes	leaf area index	biomass (above ground)
wind speed and direction		soil carbon
CO ₂ concentration vertical profile, normal precision		stem diameter
net radiation: <ul style="list-style-type: none"> incoming/reflected global radiation incoming/outgoing longwave radiation Albedo 		above-ground Net Primary Production (NPP)
diffuse global radiation		litter fall
incoming / reflected under canopy Photosynthetic Active Radiation (PAR)		land-use history
temperature and relative humidity vertical profile		managements and natural disturbances
air pressure		C and N import and export on managed sites
precipitation, through-fall, snow depth		
soil heat flux		
ground water level		
soil temperature profile		
water content profile		

Table 10: ICOS variables measured continuously during 2018 in San Rossore

FLUXES	CO ₂ , latent heat, sensible heat
METEOROLOGY	3D wind speed, temperature, relative humidity, pressure, precipitation
RADIATION	short & long wave incoming & outgoing, direct & diffuse photosynthetic active radiation
SOIL	temperature profile, water content profile, heat flux, water table height

The scientific activities at the site are embedded into the ICOS initiative. ICOS (Integrated Carbon Observation System, www.icos-ri.eu) is one of the pan-European research infrastructure projects identified by the European Strategy Forum on Research Infrastructures (ESFRI) for implementation. After its preparatory phase planned for 2008 until 2013 with an extension towards 2015, during which monitoring infrastructure and technical procedures are developed, its operational phase will run for 20 years and started 2016.

Once in operational mode, greenhouse gas concentrations and fluxes will be monitored on a routine basis following a quality controlled protocol, both in terms of measurement instrumentations and procedures. The JRC plans to contribute with a Class2 Atmospheric Station (AS) for the high precision monitoring of greenhouse gas concentrations and a Class2 Ecosystem Stations (ES), the San Rossore forest flux tower, for the monitoring of ecosystem fluxes. Class2 stations provide data for less parameter compared to Class1 stations and thus require less investment for instrumentation and have lower running costs in terms of instruments and staff. The mandatory variables to be monitored at the Class2 Ecosystem Station are shown in Table 9.

With regards to data reporting, similar to the previous years, quality checked data for 2018 have been submitted for the measurement site under the station name IT-SR2 to the Fluxnet database at the European Fluxes Database Cluster at www.europe-fluxdata.eu. The only difference with previous years is that in this case the subsequent data products delivery has been managed by the ICOS Carbon Portal platform in the framework of the ICOS initiative called "ICOS 2018 drought Task Force", aiming at providing quick scientific analysis of the 2018 summer dry and hot spell that affected Europe, especially in its central and northern territories. Data are publicly accessible through this platform <https://www.icos-cp.eu/>.

5.2 Measurements in 2018

Despite being still in the upgrading phase of the measurement site to comply with ICOS Class2 requirements, the monitoring program at the new *Pinus pinea* L. plantation site continued well. The main variables measured are summarised in Table 10.

Fluxes of CO₂, H₂O and sensible heat were measured with the eddy covariance technique using EddyMeas (Olaf Kolle, www.bgc-jena.mpg.de) for data acquisition and evaluated with the EdiRe software package from the University of Edinburgh (www.geos.ed.ac.uk/abs/research/micromet). The ancillary parameters (meteorology, radiation and soil) were obtained with their respective sensors and the data quality checked for instrument malfunctioning, obvious outliers and consistency. In the following chapters, the instruments used are described and then some basic analysis and plots of the main variables measured during the course of 2018 are presented.

5.3 Description of the instruments

5.3.1 Infrastructural

5.3.1.1 Sensor location

The instruments for eddy covariance flux system, i.e. sonic anemometer and fast gas analyser, solar radiation and meteorological parameters are mounted on the top of the guided wire tower at a height of 24 m above ground, 5 m above the canopy top at 19 m.

Soil parameters are measured at an undisturbed soil plot approximately 20 m west of the tower.

A wooden hut complements the installation hosting IT and communication equipment, a UPS system and is also used for storage.

5.3.1.2 Data acquisition

Eddy covariance flux data are stored with high frequency, i.e. 10 Hz, as chunks of 30 minutes on a local laptop connected to the sonic anemometer. In October this data acquisition system has been replaced by a Smartflux2 system from Licor (www.licor.com) that acquires all eddy covariance data digitally.

Data from the sensors located on the tower top are read every 10 s and averaged and stored every 30 minutes by a CR3000 data logger from Campbell (www.campbellsci.co.uk) also installed on the tower top. Soil measurements are handled the very same way by a CR1000 installed on the ground.

For eddy covariance flux data, the start time of every 30 minutes measurement period is saved as the reference time, whereas for all other data, the end of the 30 minutes measuring period is used. The time reference used for all San Rossore measurements is local solar time (UTC+1) to comply with ICOS requirements.

5.3.1.3 Power supply, IT & communication infrastructure

The fixed line power supply of 4 kW is locally backed up by an UPS system MSM 10 from Riello (www.riello-ups.de) to protect the system from transient power outages and provide an autonomous running time of approx. 19 hours for the installation. Computers and data loggers are connected via a local TCP/IP network. In addition, two cellular routers, one OnCell G3470A-LTE from Moxa and (www.moxa.com) one TK704U from Welotec as backup(www.welotec.com) provides internet access via the mobile 3G / 4G network. For safety reason at the remote site, a 3G repeater provides mobile phone coverage also on the forest ground in the vicinity of the site.

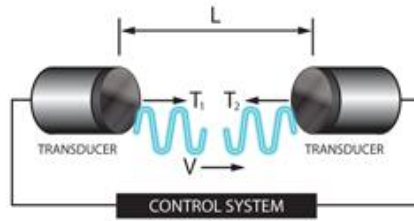
Measurement data is automatically transferred from San Rossore via ftp to a server (sanrosso@ftp-ccu.jrc.it) in Ispra at 06:00 local solar time. Remote connection to a computer at the site can be established as well.

5.3.2 Ecosystem fluxes

5.3.2.1 Sonic Anemometer for 3D wind direction Gill HS-50

Sonic anemometers determine the three dimensional wind vectors at high frequency using the speed of sound. The Gill HS-50 (www.gill.co.uk) emits ultrasonic pulses between its pairs of transducers, measures the flight time of the pulses to the paired transducer and calculates the wind speed in the direction of the transducer pair (see Fig. 57). Combining the results from the three transducer pairs, the 3 dimensional wind speed is calculated at a frequency of 10 Hertz. After a rotation of the coordinate system during the data processing to align it to north, horizontal and vertical wind speeds and the wind direction are calculated besides their use for flux calculations. As the speed of sound measured with the anemometer depends on the temperature, the so-called sonic temperature is reported by the instrument as well.

Due to the absence of moving parts and the fact that no calibration is required, the instrument is very robust and reliable. Instrument servicing is done at the manufacturer.



$$T_2 = \frac{L}{C - V} \quad \text{and} \quad T_1 = \frac{L}{C + V}$$

therefore

$$V = \frac{L}{2} \left\{ \frac{1}{T_1} - \frac{1}{T_2} \right\} \quad C = \frac{L}{2} \left\{ \frac{1}{T_1} + \frac{1}{T_2} \right\}$$

Fig. 57: Measurement principle of sonic anemometers, sketch from www.gill.co.uk
(T : travelling time of sound pulses, L : distance between transducers, C : speed of sound, V : wind speed in direction of transducers)

5.3.2.2 Fast infrared gas analyser (IRGA) for CO_2 & H_2O concentration LI-7200 FM from Licor

For the determination of CO_2 and H_2O fluxes with the eddy covariance technique, fast analysers (10 to 20 Hertz) for concentration measurements of the gases of interest are obligatory. At the San Rossore forest flux tower, a LI-7200 FM system from LI-COR (www.licor.com) has been installed, consisting of the LI-7200 enclosed $\text{CO}_2/\text{H}_2\text{O}$ analyser, the LI-7550 analyser interface unit and the LI-7200-101 flow module. In October 2017 the system has been upgraded with a 2 μm stainless steel particle filter and a heated tube at the inlet.

The LI-7200 is a high performance, non-dispersive, enclosed open path infrared $\text{CO}_2/\text{H}_2\text{O}$ analyser based on the infrared absorption of CO_2 and H_2O at ambient conditions that provides concentration measurements at a frequency of up to 20 Hertz. With the flow module, ambient air is drawn into to analyser through the sample inlet at a set flow rate of 15 l/min. In the sample volume of 16.09 cm^3 (see Fig. 58), light from the infrared source is absorbed at characteristic wavelengths for CO_2 and H_2O . This specific absorption is a function of the gas concentration in the sample volume. Using the absorption measurements at the CO_2 & H_2O wavelengths, at a non-absorbing wavelength plus calibration factors and measured temperature and pressure, the LI-7200 reports molar densities, mass densities or mole fraction of the two gases.

Zero and span checks and calibrations are done regularly using zero gas from a cylinder plus a dew point generator (RH CAL from EdgeTech) and a CO_2 standard from a cylinder.

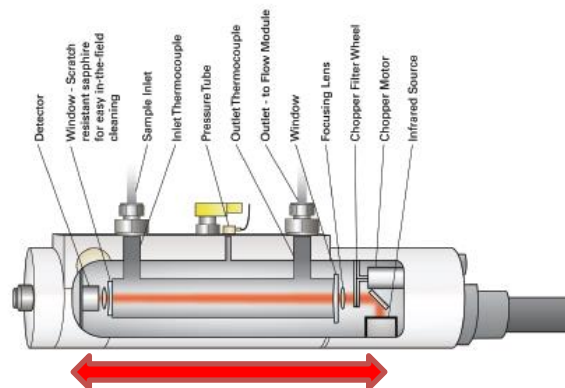


Fig. 58: LI-7200 analyser head (from www.licor.com), arrow indicates sampling volume

5.3.3 Radiation instruments

5.3.3.1 Net radiometer Kipp & Zonen CNR4

The net radiometer CNR 4 from Kipp & Zonen (www.kippzonen.com) measures the energy balance between incoming and reflected radiation in the short (305 – 2800 nm) and long (5-50 μ m) wavelength range to obtain the net radiation at the earth's surface. The short wavelength range is measured with two CM3 pyranometers, one facing upwards and one downwards. For the long range, two CG3 pyrgeometers facing opposite directions are used. The design of the instrument ensures a field of view of 180° upwards and downwards for the respective sensors. The CNR 4 features a blower and heating system to minimise the influence of dew and frost on the radiation measurements.

The energy E_{short} of the short wave or so-called global (solar) radiation is calculated from the voltages provided by the CM3's using their sensitivity C_{CM3} : $E_{short} = V / C_{CM3}$. To calculate the energy E_{long} of the long wave radiation from the reported voltages, besides the sensitivities of the CG3's C_{CG3} , also the sensor temperature T measured with a PT-100 is needed: $E_{long} = V / C_{CG3} + 5.67 \cdot 10^{-8} \cdot T^4$. The net radiation over all wavelengths is then easily calculated by adding the respective energies: $E_{net} = E_{short}^{up} + E_{long}^{up} - E_{short}^{down} - E_{long}^{down}$. In addition, the Albedo of the earth's surface defined as the ratio of outgoing to incoming solar radiation can be obtained with the instrument as well: $Albedo = E_{short}^{down} / E_{short}^{up}$.

Calibration and instrument checks at the factory are recommended every two years according to the manufacturer.

5.3.3.2 Photosynthetic active radiation Delta-T BF5

With the Sunshine Sensor BF5 from Delta-T (www.delta-t.co.uk), total (in the sense of direct plus diffuse) solar radiation, diffuse radiation and the sunshine state is measured as photosynthetic active radiation (PAR) of the solar spectrum, i.e. from 400-700 nm. The BF5 features a heating system to prevent condensation. To distinguish between direct and diffuse radiation, a set of seven photodiodes (PD) is arranged under a patterned hemispherical dome with 50% black bands such that at any position of the sun in the sky at least one photodiode is completely in the shade and at least one is fully exposed to direct sunlight. This design eliminates the necessity of frequent alignment of the shading parts to the position of the sun. The diffuse radiation is then given by $PAR_{diffuse} = 2 \cdot PD_{min}$ and the direct by

$$PAR_{direct} = PD_{max} - PD_{min}.$$

The instrument reports $PAR_{diffuse}$, $PAR_{total} = PAR_{diffuse} + PAR_{direct}$ and sunshine state.

The latter one indicates sunshine if $PAR_{total} / PAR_{diffuse} > 1.25$ and $PAR_{total} > 50 \mu\text{mol} \cdot \text{m}^{-2} \cdot \text{s}^{-1}$.

5.3.4 Meteorological sensors

5.3.4.1 Temperature & relative humidity UMS KPK1/5-ME

Ambient temperature is measured with a PAA-41 capacitive pressure sensor from Keller Druckmesstechnik (www.keller-druck.com) using a ceramic measurement cell for enhanced reliability. It has been replaced in October by a PTB110 pressure sensor from Vaisala (www.vaisala.com).

5.3.4.2 Ambient air pressure Keller Druckmesstechnik PAA-41

Ambient air pressure is measured with a PAA-41 capacitive pressure sensor from Keller Druckmesstechnik (www.keller-druck.com) using a ceramic measurement cell for enhanced reliability.

5.3.4.3 Rain sensor UMS ARG 100/std

The ARG 100/std from UMS (www.ums-muc.de) is a tipping bucket type of rain gauge. It features a collecting funnel with a surface area of 500 cm² and a resulting resolution of 0.2 mm of rain fall per tip.

5.3.5 Soil instruments

5.3.5.1 Soil heat flux sensors HFP01 from Hukseflux

Three thermal sensors HFP01 from Hukseflux (www.hukseflux.com) have been buried ten centimetres underground in the undisturbed soil around the tower to obtain a good spatial averaging of the soil

heat flux. The determination of the heat flux is based on measuring the temperature difference of two sides of a plate that is exposed to a heat flow using a number of thermocouples connected in series (see Fig. 59) with the convention that positive values indicate a heat flux into the soil, a negative one heat flux out of the soil. Ignoring possible errors, the temperature difference between the hot and cold side of the sensor is proportional to the heat flow. As the thermocouples provide a voltage proportional to the temperature, the voltage output of the sensor is proportional to the heat flow across the sensor.

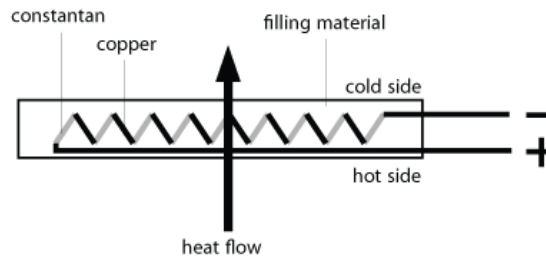


Fig. 59: Sketch of a soil heat flux sensor (drawing from www.wikipedia.org)

5.3.5.2 Soil water content vertical profile with TRIME-TDR from IMKO

Profile measurements of soil water content are performed using the TRIME-TDR (Time domain Reflectometry with Intelligent MicroElements) from IMKO (www.imko.de). Based on Time-Domain-Reflectometry, the sensor generates high frequency electromagnetic pulses that propagate along a wave guide and reflect back into the sensor. Depending on the dielectric constant of the material surrounding the waveguide, the round trip time of the hf-pulses varies between some tens and thousand picoseconds. As the dielectric constant of soil and thus the round trip time strongly depends on the soil moisture content, measuring this time gives the water content of the soil surrounding the sensor. Burying several sensors at depths of 5, 15, 25, 45, and 90 cm below ground provides the soil humidity profile.

5.3.5.3 Soil temperature profile with Th3-v probe from UMS

For the measurement of soil temperatures at different depths, a Th3-v probe from UMS (www.ums-muc.de) is used. This probe features a convenient set of 6 temperature probes in a profile system buried at 0, 5, 15, 25, 45, and 95 cm below the transition of organic and mineral soil at approx. 5 cm below the surface.

5.3.5.4 Ground water level CS456-SA from Campbell Scientific

The ground water level is monitored with a Diver from Campbell Scientific (www.campbellsci.co.uk). The device is placed in a water filled hole, 2.6 m below ground, and measures directly the difference between water and atmospheric pressure ($p_{Diff} = p_{Diver} - p_{baro}$). This gives the water column above the sensor and together with the known sensor depth below ground, the water table height can be easily calculated (see also Fig. 60):

$$WL = TOC - CL - WC \text{ with } WC = 9806.65 \cdot \frac{(p_{Diver} - p_{baro})}{\rho \cdot g};$$

$$g = 9.81 \text{ m/s}^2, \rho = 1.00 \text{ kg/m}^3$$

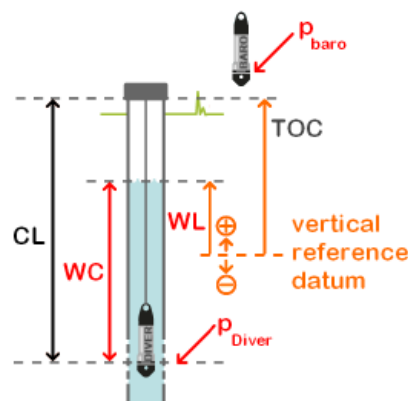


Fig. 60: Principle of water level calculation using the Diver (sketch from www.swstechnology.com).
CL: cable length, TOC: top of container, WC: water column, WL: water level relative to a reference, p: pressure.

Table 11: Processing steps for flux calculations using the EdiRe Software package.

EdiRe Process	brief description
Preprocessed Files	data from input file, gas concentrations as molar densities
Extract	all high speed data
Despike	all high speed data
Linear	conversion of raw data from voltages into physical variables
1 chn statistics	averages of 3D wind, sonic temperature and gas concentration
Gas conversion	conversion of molar densities to molar fraction
Filter – detrend	linear detrending of gas concentrations
Wind direction	align with geographic direction
Rotation coefficients	perform 3D coordinate rotation
Cross Correlate	gas concentrations with vertical wind speed
Remove Lag	remove time lag between anemometer and gas analyser
Friction Velocity	calculate u^*
Sensible heat flux coefficient	
Latent heat of evaporation	
2 chn statistics	calculate covariances, i.e. uncorrected fluxes
Sonic T - heat flux correction	
Stability - Monin Obhukov	calculate z/L stability parameter
Frequency response	calculate high frequency correction for all fluxes
Webb correction	calculate water density fluctuation correction for all fluxes
Stationarity	perform stationarity test
Integral Turbulence	calculate integral turbulence
Cospectra	calculate co-spectra for all fluxes
Storage	calculate storage term
User defined	determine quality flag (0,1,2) for all flux data according to Carboeurope methodology

5.3.6 Flux data processing

Data processing for flux estimates is done using the free EdiRe software package developed at the micrometeorology group from the University of Edinburgh. (www.geos.ed.ac.uk/abs/research/micromet/EdiRe/). As input data, EdiRe uses the 30 min raw flux data files in the binary *.slt format plus 30 minute averaged pressure, temperature and relative humidity data in ASCII format. As time convention, the start of the measurement period has to be assigned to the input data, the middle of the measurement period is assigned to the output data.

The main processing steps used within EdiRe to arrive at final, 30 minute averaged flux data that are corrected for various effects are listed in Table 11. In order to obtain budgets from e.g. annual datasets that unavoidably contain gaps in the data, a gap filling procedure must be established to calculate the missing values based on drivers for the respective parameter. In addition, partitioning of the measured CO₂ flux (that is the Net Ecosystem Exchange, NEE), into Gross Primary Production (GPP, the gross carbon uptake) and respiration of the Ecosystem (Reco) enables a better understanding of the underlying ecosystem exchange processes..

Gap-filling and partitioning of the data is done with the online tool at:

www.bgc-jena.mpg.de/bgi/index.php/Services/REddyProcWeb.

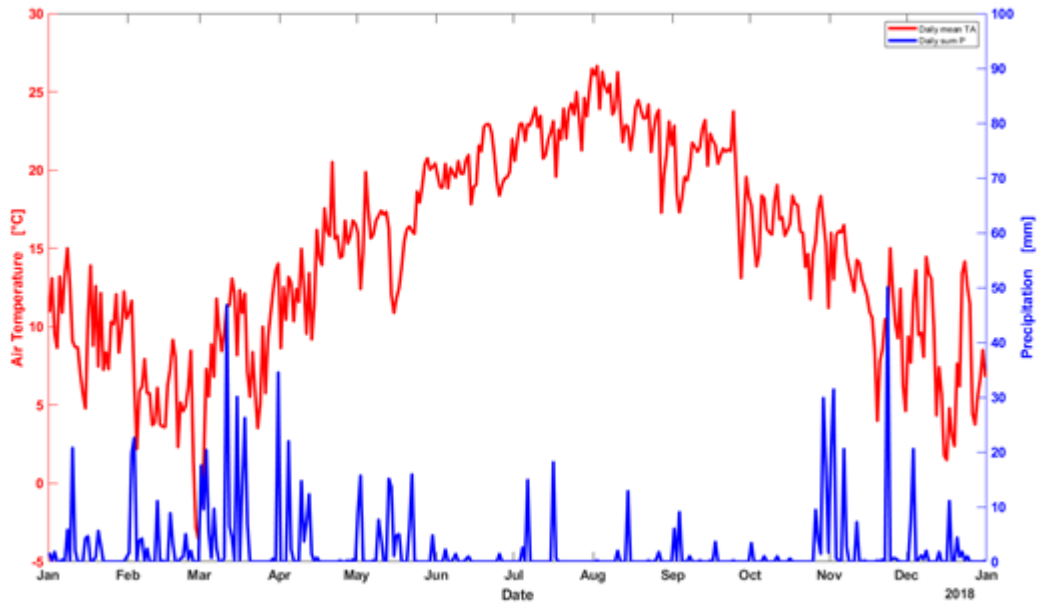


Fig. 61: Time evolution of the daily averaged Air Temperature (red) and daily total precipitation (blue) records for San Rossore forest station.

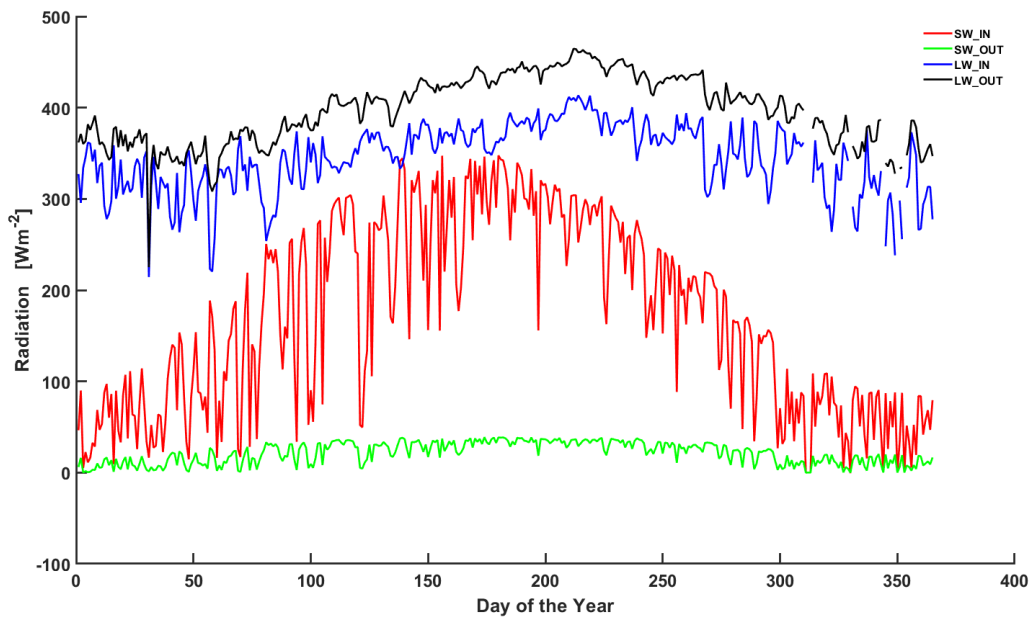


Fig. 62: Daily averages of the four components of the radiation budget above the San Rossore forest: ShortWave incoming (SW_IN, red), ShortWave reflected (SW_OUT, green), LongWave incoming (LW_IN, blue) and LongWave emitted (LW_OUT, black)

5.4 Results of the year 2018

5.4.1 Meteorology

The annual average of air temperature, estimated at the IT-SR2 station above the forest, has been 16.16°C for 2018, with daytime average value of 17.20°C and night time 14.71°C. Compared to the long term average of 14.2°C, the 2018 average was significantly higher, with a positive anomaly of +1.96°C. The maximum value of the daily average was 27.55°C and the minimum -1.73°C. The maximum and minimum half-hourly recorded values were 31.43°C and -5.47°C, respectively. The cumulative sum of precipitation resulted in a yearly total rainfall of 886mm, very close to the long term estimated average of 876mm. However, in 2018 sporadic but significant rain events occurred during the course of the summer months, like July, August and early September while the site usually experiences prolonged dry spells, with limited or negligible summer rainfall. In Fig. 61 the yearly trends of daily Air Temperature and Rain amount for the station of San Rossore forest are reported.

The wind regime was almost uniquely characterized by typical sea-breeze regime, with predominant wind directions land-to-sea (land breeze, blowing from East-North East) and sea-to-land (sea breeze, blowing from West-South West). This regime is depicted in Fig. 63, where the angular distribution of the directions of origin of the wind, measured by the sonic anemometer above the canopy, are reported. The maximum wind speed gust over the entire year, averaged over 30 minutes time interval, was 7.5ms⁻¹ while the overall average wind speed was 1.6ms⁻¹, corresponding to 27.0 kmh⁻¹ and 5.7 kmh⁻¹, respectively.

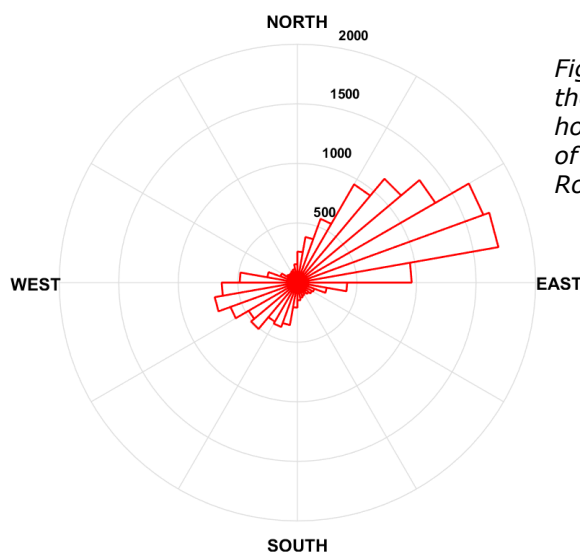


Fig. 63: Wind Rose reporting the distribution of all half-hourly direction of provenances of the wind above the San Rossore forest.

5.4.2 Radiation

The daily averaged values of LongWave and ShortWave incoming and outgoing radiation components, measured above the canopy of San Rossore forest, are plotted as a function of the day of the year in Fig. 62. The corresponding wavebands are determined by the radiometers selectivity, as reported in the section 5.3 above.

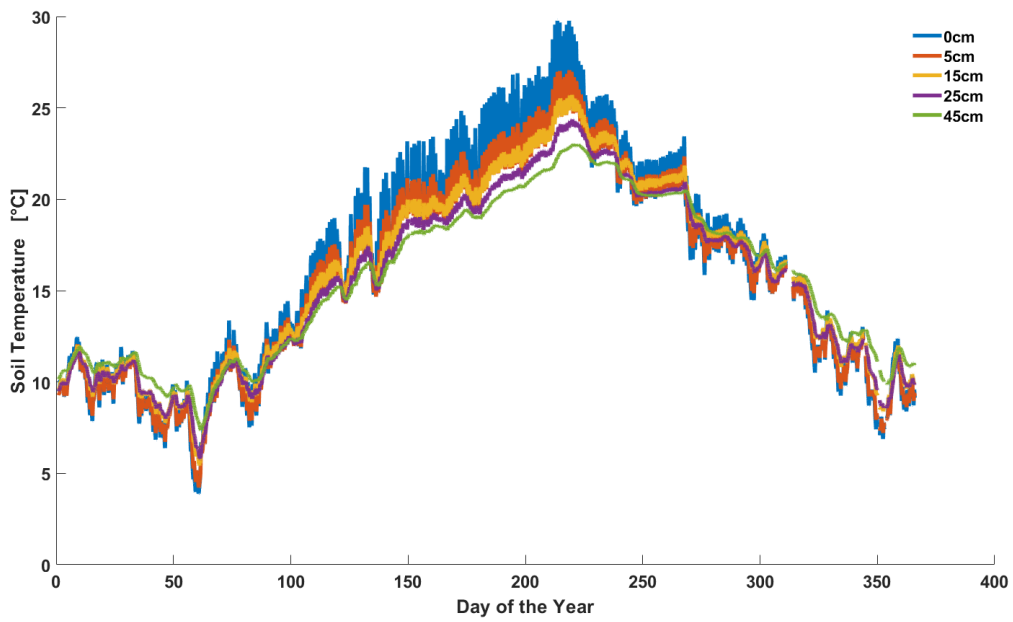


Fig. 64: Measurements of soil temperature at six different depths in the ground of San Rossore forest

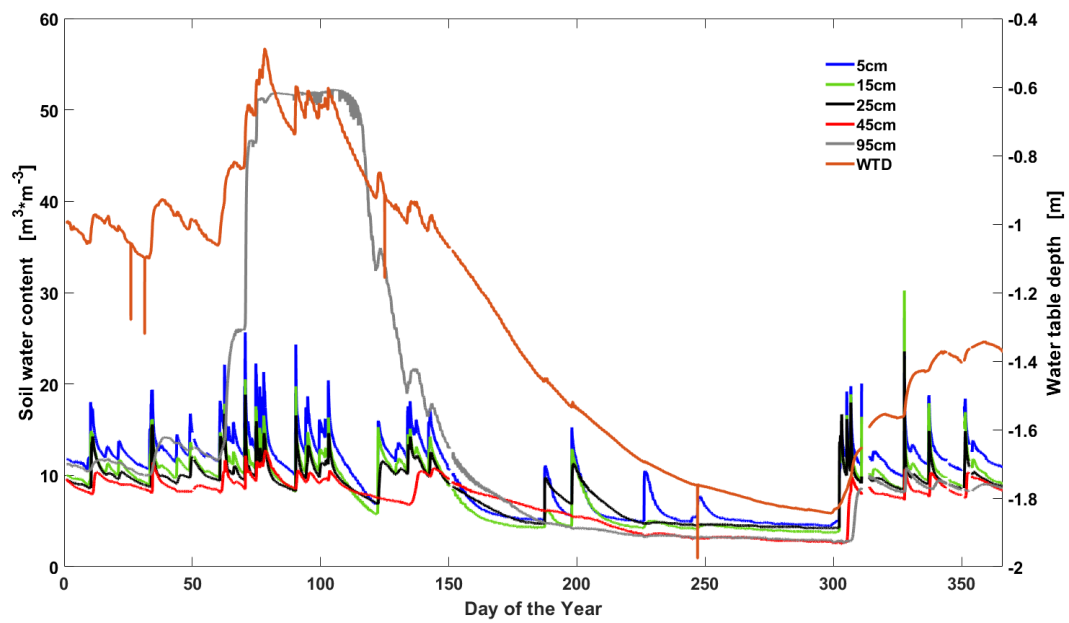


Fig. 65: Measurements of soil water content at five different depths and water table depth in the ground of San Rossore forest.

5.4.3 Soil meteo-climatic variables

All the measurements collected in the soil pits by the instrumentation described in the section 3 above, have been analysed and briefly reported. Measurements of soil temperature (TS) at six depths are shown in Fig. 64, while soil water content (SWC) and water table depth (WTD) records are plotted in Fig. 65. The yearly trends are consistent with the hydrometeorological cycle of the Mediterranean summer and the sporadic rain events during the driest months are detectable as well.

It is worth noting the relatively shallow depth of the water table depth for most part of the summer, compared to typical Mediterranean and dry climates. In this case, the average between two different sampling locations is reported. The minimum values of the summer period in these two locations, both close to the main tower, were -2.05m and -1.64m, suggesting that probably water was accessible to the trees via tap roots for the whole summer

5.4.4 Eddy covariance flux measurements

The eddy covariance methodology has been used to estimate turbulent variables at the forest-atmosphere interface in San Rossore, with special attention payed to mass (carbon, water) and energy (latent and sensible heat, momentum) exchanges. Well established processing scheme has been implemented both at raw data level to obtain half-hourly estimates of turbulent variables, both at the post-processing level to obtain defensible estimates of the carbon and water fluxes at longer time scales, i.e. daily to annual. These goals have been achieved through the successive implementation of two free software tools developed by the micrometeorological community, i.e the EdiRe softare package (University of Edinburgh) for half-hourly turbulent flux estimates based on high frequency anemometer and gas analyser measurements and the REddyProc online tool (Max Planck Institute for Biogeochemistry - <https://www.bgc-jena.mpg.de/bgi/index.php/Services/REddyProcWeb>). Inputs for the latter step were the EdiRe half-hourly outputs. The most relevant calculations and corrections applied by the EdiRe software are reported in section 3 above, while the criteria used to de-spike and select its outputs as input for the REddyProc runs have been chosen accordingly to calculations performed previous years, for the sake of consistency.

In synthesis the following steps have been done:

- Data have been filtered for turbulence conditions, according to quality checks methodology adopted in CARBOEUROPE and FLUXNET.
- Physically not plausible values, i.e. outliers, have been removed
- Friction velocity threshold has not been applied
- Traditional Night-Time values of Net Ecosystem Exchange (NEE) measurements have been used to partition the measured fluxes into photosynthetic assimilation (GPP) and respiratory release (Reco): $NEE = Reco - GPP$

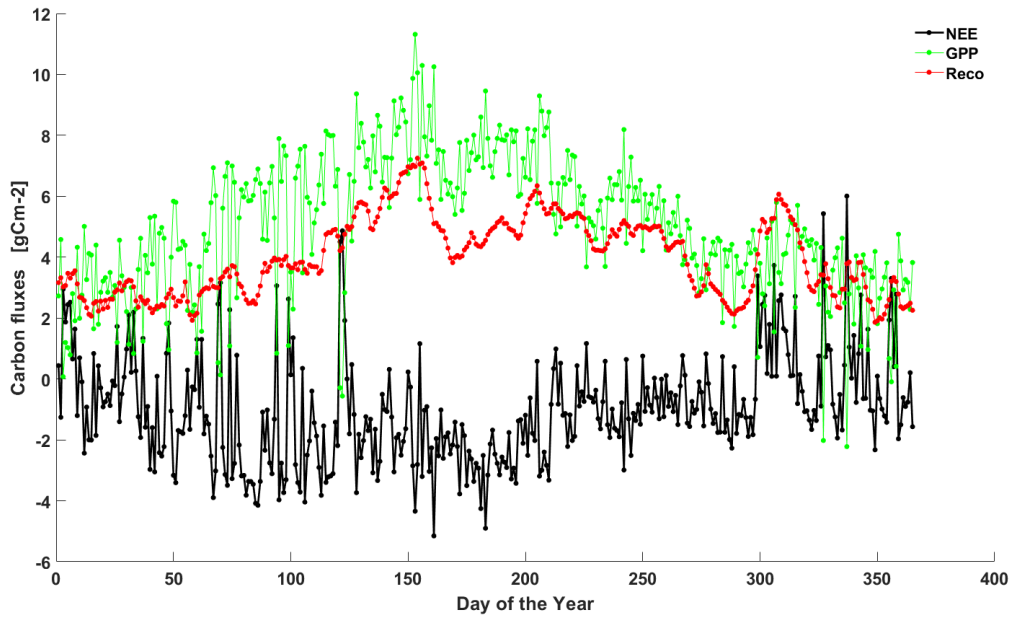


Fig. 66: Daily sums of the three components of the carbon cycle between San Rossore forest and the atmosphere: Net Ecosystem Exchange (NEE), Gross Primary Production (GPP) and Ecosystem Respiration (Reco).

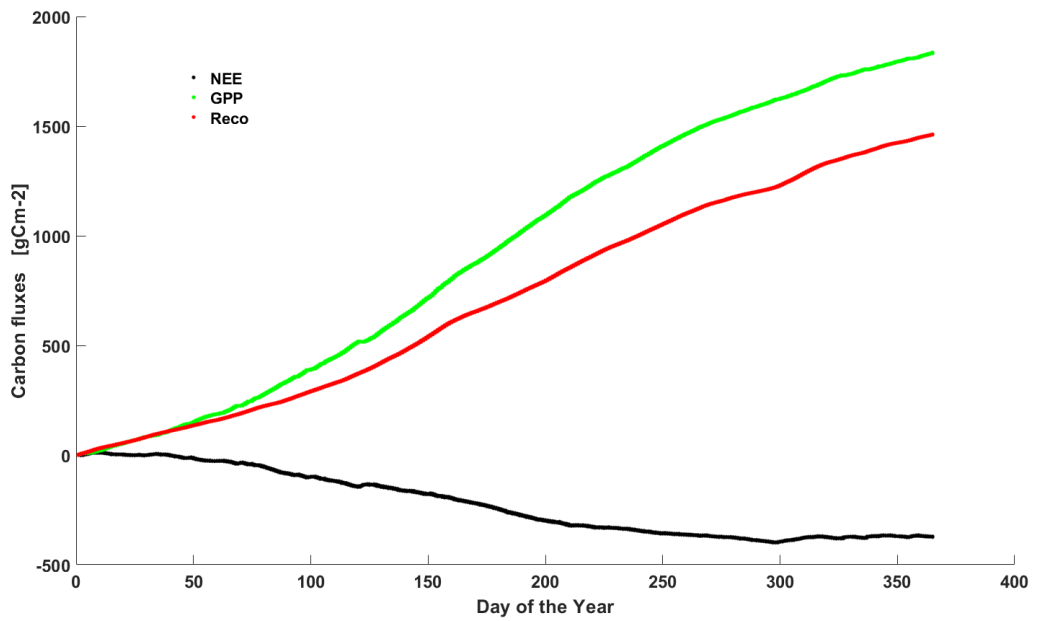


Fig. 67: Yearly trend of the three components of the carbon cycle between San Rossore forest and the atmosphere: Net Ecosystem Exchange (NEE), Gross Primary Production (GPP) and Ecosystem Respiration (Reco).

In details all the data collected in periods of “good and reliable” turbulence conditions, i.e. having quality checks (QC) equal to 0 and 1 according to the CARBOEUROPE and FLUXNET methodology, have been retained as inputs for the gap-filling and partitioning tool, while data with QC=2 have been discarded.

Values of carbon flux (NEE) outside the range $[-50 \mu\text{molCm}^{-2}\text{s}^{-1}; +50 \mu\text{molCm}^{-2}\text{s}^{-1}]$ have been discarded because physically and ecologically not reliable, while latent and sensible heat outside the range $[-200\text{Wm}^{-2}; 1000\text{Wm}^{-2}]$ have also been discarded for the same reason. The friction velocity threshold was not used at this stage and the night-time partitioning was applied for consistency with previous years estimates of NEE, GPP and Reco. In Fig. 66 daily sums of the three components of the carbon cycle at the San Rossore forest are plotted: the trends are consistent with previous years estimates and with theoretical expectations. At a first look an evident and substantial increase in ecosystem respiration can be detected at the end of the summer period, with consequent reduction of the overall carbon sink strength of the forest.

However, on the annual scale the ability of the forest to act as a sink of carbon, resulting from the balance between photosynthesis and respiration, seems to be confirmed and the order of magnitude of the three components is comparable with estimates from previous years. With the above-mentioned data selection criteria applied, the results for the whole 2018 as listed in Table 12 below:

Table 12: Carbon fluxes at the forest station of San Rossore in 2018.

NEE	$-373\text{gCm}^{-2}\text{y}^{-1}$
GPP	$1836\text{gCm}^{-2}\text{y}^{-1}$
Reco	$1463\text{gCm}^{-2}\text{y}^{-1}$

The cumulative sum of the three components are plotted in Fig. 67, as a function of the day of the year to visualize the yearly trend.

Similarly to the carbon fluxes, also the energy net exchanges, i.e. latent and sensible heat turbulent fluxes, have been measured between the forest of San Rossore and the atmosphere. Both the daily sums and the yearly cumulative trends for the energy components are reported in Fig. 68 and Fig. 69, respectively.

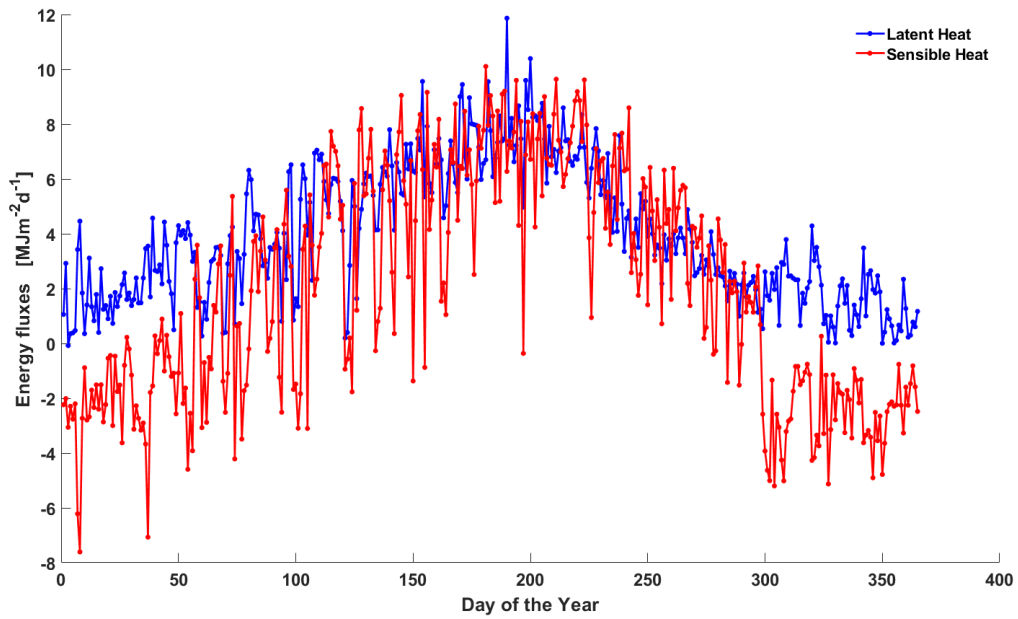


Fig. 68: Daily sums of the energy fluxes between San Rossore forest and the atmosphere: Latent heat and Sensible Heat

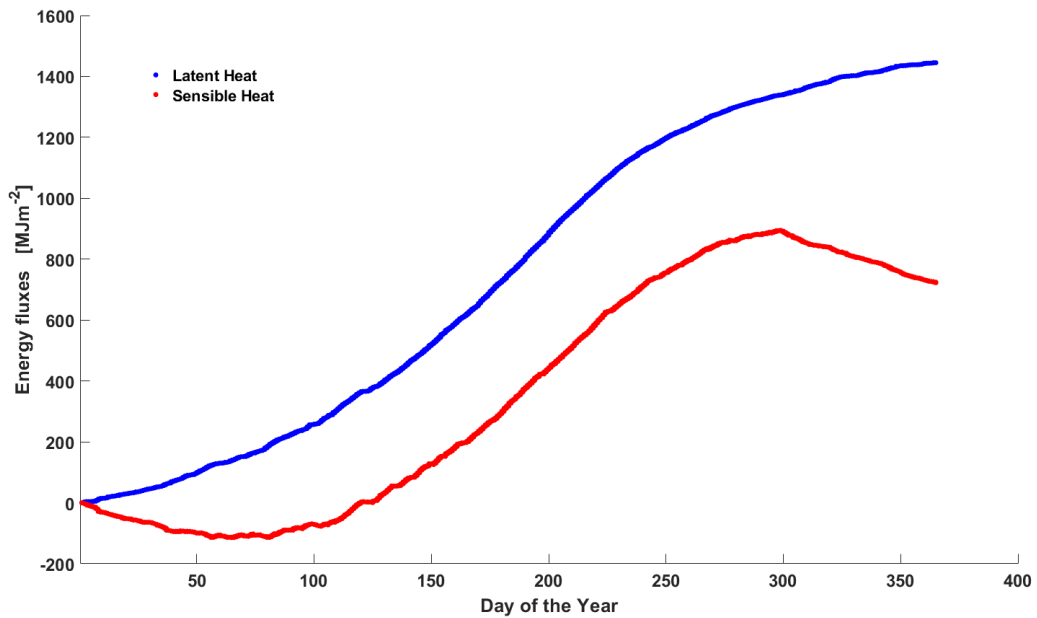


Fig. 69: Yearly trend of the cumulative sum of the energy fluxes between San Rossore forest and the atmosphere: Latent heat and Sensible Heat

5.4.5 Ancillary measurements

Finally, it is worth to mention that a series of additional biometric measurements have been collected on a campaign mode, the so-called "ancillary" measurements that constitute a fundamental complement to the set of continuously sampled and recorded micrometeorological measurements, for the correct interpretation of ecosystem behaviour. In particular at San Rossore the following ancillary measurements have been collected:

- eight different field surveys for collection of Digital Hemispherical Pictures in order to provide a time course non-destructive measurement series of the leaf area index (LAI)
- One assessment of the above ground wood biomass (AGB) and of the herbaceous biomass in the understorey of the forest at the peak of the growing season
- One collection of leaf samples during the winter for elemental analysis (C,N) and leaf to mass area ratio determination
- Forest mapping with specific laser range-finder

All the above mentioned ancillary measurements and samples have been collected following the most updated ICOS instructions and made available to the ICOS-ETC (Ecosystem Thematic Center) distributed in Italy (Università degli Studi della Tuscia, Viterbo), Belgium (Universiteit Antwerpen, Antwerpen) and France (INRA, Bordeaux) for an initial forest description and characterization and for long term repository.

References

- Adam, M., J. P. Putaud, S. Martins dos Santos, A. Dell'Acqua, and C. Gruening, Aerosol hygroscopicity at a regional background site (Ispra) in Northern Italy, *Atmos. Chem. Phys.*, **12**, 5703–5717, 2012
- Anderson, T.L., and Ogren, J.A., Determining aerosol radiative properties using the TSI3563 integrating nephelometer, *Aerosol Sci. Technol.*, **29**, 57–69, 1998.
- Arnott, W.P., Hamasha, K., Moosmüller, H., Sheridan, P.J., and Ogren, J.A., Towards aerosol light-absorption measurements with a 7-wavelength Aethalometer: Evaluation with a photoacoustic instrument and a 3 wavelength nephelometer, *Aerosol Sci. Technol.*, **39**, 17–29, 2005.
- Bergamaschi P. and D. Brunner, Analysis of the sensitivity of atmospheric measurements at the JRC Ispra Atmosphere - Biosphere - Climate Integrated monitoring Station, Footprint analysis based on FLEXPART-COSMO model, JRC technical report, EUR 27131 EN, 2015.
- Cavalli, F., Putaud, J.P., Toward a standardised thermal-optical protocol for measuring atmospheric organic and elemental carbon: the EUSAAR protocol, *Atmos. Meas. Tech.*, **3**, 79–89, 2010.
- Cavalli, F., Alastuey, A., Areskoug, H., Cech, J., Ceburnis, D., Genberg, J., Harrison, R.M., Jaffrezo, J.L., Kiss, G., Mihalopoulos, N., Perez, N., Quincey, P., Schwarz, J., Sellegri, K., Spindler, G., Theodosi, C., Yttri, K.E., Aas, W., Putaud, J.P., 2016. A European aerosol phenomenology -4: harmonized concentrations of carbonaceous aerosol at 10 regional background sites across Europe. *Atmos. Environ.*, **144**, 133–145, 2016.
- Cooke, W.F., Liousse, C., Cachier, H., and Feichter, J., Construction of a 1x1° fossil fuel emission data set for carbonaceous aerosol and implementation and radiative impact in the ECHAM4 model, *J Geophys. Res.*, **104**; 22,137–22, 1999.
- Dlugokencky, E.J., J.W. Mund, A.M. Croswell, M.J. Croswell, and K.W. Thoning (2019), Atmospheric Carbon Dioxide Dry Air Mole Fractions from the NOAA ESRL Carbon Cycle Cooperative Global Air Sampling Network, 1968–2018, Version: 2019-07, <https://doi.org/10.15138/wkqj-f215>.
- Dlugokencky, E.J., A.M. Croswell, J.W. Mund, M.J. Croswell, and K.W. Thoning (2019), Atmospheric Methane Dry Air Mole Fractions from the NOAA ESRL Carbon Cycle Cooperative Global Air Sampling Network, 1983–2018, Version: 2019-07, <https://doi.org/10.15138/VNCZ-M766>
- EMEP manual for sampling and chemical analysis (1995). *EMEP/CCC-Report 1/95. (Revised 1996; 2001; 2002)*. 1995.
- European Directive 2008/50/EC. On ambient air quality and cleaner air for Europe. 2008.
- Gruening C., et al., JRC Ispra EMEP-GAW regional station for atmospheric research: 2008 report, EUR 24088 EN, (2009), JRC55382.
- Hess, M., Koepke, P. Schult, I., Optical Properties of Aerosols and Clouds: The Software Package OPAC, *Bull. of Am. Meteorol. Soc.*, **79**; 831–844, 1998.
- Jensen, N. R., Gruening, C., Adams, M., Cavalli, F., Cavalli, P., Grassi, F., Dell'Acqua, A., Martins Dos Santos, S., Roux, D., Putaud, J.-P. JRC Ispra EMEP – GAW regional station for atmospheric research, 2009 report, *EUR 24678 EN*, (2010), JRC62602.
- Jensen, N. R., Gruening, C., Goded, I., Mueller, M., Hjorth, J., Wisthaler, A. Eddy-covariance flux measurements in an Italian deciduous forest using PTR-ToF, PTR-QMS and FIS. *Int. J. Env. An. Chem.*, **98**; 758–788, 2018). *Doi: 10.1080/03067319.2018.1502758*.
- Kiehl, J. T., Schneider, T. L., Rasch, P. J., Barth, M. C., Wong, J., Radiative forcing due to sulfate aerosols from simulations with the National Center for Atmospheric Research Community Climate Model, Version 3 (Paper 1999JD900495), *J. Geophys. Res.*, **105**; 1441–1458, 2000.
- Koffi, E. N., Bergamaschi, P., Karstens, U., Krol, M., Segers, A., Schmidt, M., Levin, I., Vermeulen, A. T., Fisher, R. E., Kazan, V., Klein Baltink, H., Lowry, D., Manca, G., Meijer, H. A. J., Moncrieff, J., Pal, S., Ramonet, M., Scheeren, H. A., and Williams, A. G.: Evaluation of the boundary layer dynamics of the TM5 model over Europe, *Geosci. Model Dev.*, **9**, 3137–3160, <https://doi.org/10.5194/gmd-9-3137-2016>, 2016.
- McMurry, P., Wang, X., Park, K., and Ehara, K. The relationship between mass and mobility for atmospheric particles: A new technique for measuring particle density, *Aerosol Sci. Tech.*, **36**, 227–238, 2002.
- Mira-Salama, D., Van Dingenen, R., Gruening, C., Putaud, J.-P., Cavalli, F., Cavalli, P., Erdmann, N., Dell'Acqua, A., Dos Santos, S., Hjorth, J., Raes, F., Jensen, N.R. Using Föhn conditions to characterize urban and regional sources of particles, *Atmospheric Research* **90**, 159–166, 2008.

- Mueller, T., *Development of correction factors for Aethalometers AE31 and AE33, ACTRIS-2 workshop*, Athens, 2015, <http://wmo-gaw-wcc-aerosol-physics.org>.
- Pépin L., Schmidt M., Ramonet M., Worthy D.E.J. and Ciais, P. Notes des Activités Instrumentales, A new gas chromatographic experiment to analyze greenhouse gases in flask samples and in ambient air in the region of Saclay, Institut Pierre-Simon Laplace (2001), <http://www.ipsl.jussieu.fr>.
- Petzold, A., H., Schönlinner, M., Multi-angle absorption photometry - A new method for the measurement of aerosol light absorption and atmospheric black carbon, *Journal of Aerosol Science*, **35** (4), 421-441, 2004.
- Putaud, J.-P., et al. (21 authors), 2004, A European aerosol phenomenology—2: chemical characteristics of particulate matter at kerbside, urban, rural and background sites in Europe. *Atmospheric Environment*, **38**, 2579-2595.
- Putaud, J.-P., et al. (39 authors), 2010, A European aerosol phenomenology—3: Physical and chemical characteristics of particulate matter from 60 rural, urban, and kerbside sites across Europe. *Atmospheric Environment*, **44**, 1308-1320.
- Putaud, J.P., F. Cavalli, S. Martins dos Santos, and A. Dell'Acqua, Long-term trends in aerosol optical characteristics in the Po Valley, Italy, *Atmos. Chem. Phys.*, **14**, 9129-9136, 2014.
- Putaud J.P., Bergamaschi P., Bressi M, Cavalli F., Cescatti A., Daou D., Dell'Acqua A., Douglas K., Duerr M., Fumagalli I., Goded I., Grassi F., Gruening C., Hjorth J., Jensen N.R., Lagler F., Manca G., Martins Dos Santos S., Matteucci M., Passarella R., Pedroni V., Pokorska O., Roux D. JRC – Ispra Atmosphere – Biosphere – Climate Integrated monitoring Station. 2013 report, JRC report EUR 26995 EN, 2014.
- Putaud J.P., Bergamaschi P., Cavalli F., Dell'Acqua A., Douglas K., Duerr M., Fumagalli I., Goded I., Grassi F., Gruening C., Jensen N.R., Lagler F., Manca G., Martins Dos Santos S., Matteucci M., Passarella R., Pedroni V., Pokorska O., Roux D. JRC – Ispra Atmosphere – Biosphere – Climate Integrated monitoring Station. 2015 report, JRC report EUR 28153 EN, 2017.
- Russell, L.M.: Aerosol organic-mass-to-organic carbon ratio measurements, *Environ. Sci. Technol.*, **37**, 2982-2987, 2003.
- Schmid, O., et al., Spectral light absorption by ambient aerosols influenced by biomass burning in the Amazon Basin I: comparison and field calibration of absorption measurements techniques, *Atmos. Chem. Phys.*, **6**, 3443-3462, 2006.
- Stratmann, F., Wiedensohler, A. A new data inversion algorithm for DMPS-measurements. *J. Aerosol Sci.*, **27** (Suppl 1), 339-340, 1996.
- Thoning, K.W., P.P. Tans, and W.D. Komhyr, Atmospheric carbon dioxide at Mauna Loa Observatory, 2. Analysis of the NOAA/GMCC data, 1974-1985., *J. Geophys. Res.*, **94**, 8549-8565, 1989.
- Van Dingenen, R., et al. (28 authors), 2004, A European aerosol phenomenology –1: Physical characterization of particulate matter at kerbside, urban, rural and background sites in Europe, *Atmospheric Environment*, **38**, 2561-2577.
- Weingartner, E., Saathoff, H., Schnaiter, M., Streit, N., Bitnar, B., and Baltensperger, U., Absorption of light by soot particles: determination of the absorption coefficient by means of aethalometers, *J. Aerosol Sci.*, **34**, 1445-1463, 2003.
- Weitkamp, C. (editor), *LIDAR Range-Resolved Optical Remote Sensing of the Atmosphere*, Springer, New York, 2005.
- WHO, Health risks of ozone from long-range transboundary air pollution, 2008.
- WMO Greenhouse gas bulletin, The State of Greenhouse Gases in the Atmosphere Based on Global Observations through 2016, https://library.wmo.int/opac/doc_num.php?explnum_id=4022, 2017.
- Worthy D. E. F., Levin, I., Trivett N. B. A., Kuhlmann A.J., Hopper J. F., and Ernst M. K. Seven years of continuous methane observations at a remote boreal site in Ontario, Canada, *J. Geophys. Res.*, **103** (D13), 15995-16007, 1998.
- Worthy, D. E. F., I. Levin, N. B. A. Trivett, A. J. Kuhlmann, J. F. Hopper, and M. K. Ernst, Seven years of continuous methane observations at a remote boreal site in Ontario, Canada, *J. Geophys. Res.*, **103** (D13), 15995-16007, 1998.
- Zahorowski, W., S. D. Chambers, A. Henderson-Sellers, Ground based radon-222 observations and their application to atmospheric studies, *J. Environm. Radioact.*, **76**, 3-33, 2004.

Links

[ACTRIS](http://www.actris.eu), *www.actris.eu*

[ARPA Lombardia](http://ita.arpalombardia.it/ITA/qaria/doc_RichietaDati.asp), *ita.arpalombardia.it/ITA/qaria/doc_RichietaDati.asp*

[Calipso](http://www.nasa.gov/mission_pages/calipso/main), *www.nasa.gov/mission_pages/calipso/main*

[CCC](http://www.nilu.no/projects/ccc) (Chemical Co-ordinating Centre of EMEP), *www.nilu.no/projects/ccc*

[CEN](http://www.cen.eu/cen/pages/default.aspx) (European Committee for Standardisation), *www.cen.eu/cen/pages/default.aspx*

[CLRTAP](http://www.unece.org/env/lrtap/welcome.html), *www.unece.org/env/lrtap/welcome.html*

[EARLINET](http://www.earlinet.org), *www.earlinet.org*

[ECAC](https://www.actris-ecac.eu/) (European Centre for Aerosol Calibration), *https://www.actris-ecac.eu/*

[EMEP](http://www.emep.int), *www.emep.int*

[EPTR](https://prtr.eea.europa.eu/) (European Pollutant Release & Transfer Register), *https://prtr.eea.europa.eu/*

[EUSAAR](http://www.eusaar.net), *www.eusaar.net*

[GAW](http://www.wmo.int/pages/prog/arep/gaw) (Global Atmosphere Watch), *www.wmo.int/pages/prog/arep/gaw*

[ICOS](http://www.icos-ri.eu), *www.icos-ri.eu*

[InGOS](http://www.ingos-infrastructure.eu), *www.ingos-infrastructure.eu*

[WDCA](http://www.gaw-wdca.org) (World Data Centre for Aerosol), *www.gaw-wdca.org*

[WMO](https://public.wmo.int/en) (World Meteorological Organization), *https://public.wmo.int/en*.

List of figures

<i>Fig. 1: The JRC-Ispra site and the location of the provisional EMEP-GAW site, the greenhouse gas laboratory, and the new atmospheric observatory, built on the spot of the historical EMEP-GAW station. The provisional site and the GHG laboratory are no longer in operation since July 2017 and 2018, respectively.</i>	3
Fig. 2: The laboratories for atmospheric GHG measurements at Building 5 with 15m mast (left), and at the new Atmospheric Observatory with the 100m-tall tower (Building 77r).....	6
Fig. 3: Bd 5 GHG-system flow scheme	6
Fig. 4: The top panel shows a schematic of the GC-system set-up. Typical chromatograms are shown in the lower panels.	8
Fig. 5: Sampling, conditioning and distribution system diagram for the GHG measurements at the new Atmospheric Observatory (Building 77r).	10
Fig. 6: Graphical illustration of the Keeling plot method applied to specific CH ₄ measurements. 1/c represents the reciprocal of the atmospheric concentration of CH ₄ for that specific observation [Pataki et.al, 2003].	12
<i>Fig. 7: Time series of continuous CH₄ ambient measurements at Ispra (Building 5) between October 2007 and July 2018 with associated uncertainties. CH₄ ambient concentrations are reported as hourly mean values of dry air mole fractions. Furthermore, monthly mean concentrations from the background station Mace Head (MHD) on the West coast of Ireland are also included (Mace Head data from Simon O'Doherty, University of Bristol).</i>	15
Fig. 8: Time series of continuous CO ₂ ambient measurements at Ispra (Building 5) between October 2007 and July 2018 with associated uncertainties. CO ₂ ambient concentrations are reported as hourly mean values of dry air mole fractions. Furthermore, flask measurements from the background station Mace Head (MHD) on the West coast of Ireland are also included (Dlugokencky, et al., 2017; Thoning, 2019).	17
Fig. 9: Time series of continuous N ₂ O ambient measurements at Ispra (Building 5) between September 2010 and July 2018 with associated uncertainties. N ₂ O ambient concentrations are reported as hourly mean values of dry air mole fractions. Furthermore, monthly mean concentrations from the background station Mace Head (MHD) on the West coast of Ireland are also included (Mace Head data from Simon O'Doherty, University of Bristol).	18
Fig. 10: Time series of continuous SF ₆ ambient measurements at Ispra (Building 5) between September 2010 and July 2018 with associated uncertainties. SF ₆ ambient concentrations are reported as hourly mean values of dry air mole fractions. Furthermore, monthly mean concentrations from the background station Mace Head (MHD) on the West coast of Ireland are also included (Mace Head data from Simon O'Doherty, University of Bristol).	19
Fig. 11: Time series of continuous CH ₄ and CO ₂ ambient measurements at the Atmospheric Observatory (Bd 77r), sampled at three different heights (40m, 60m, 100m), between December 2016 and December 2018. Concentrations are reported as hourly mean values of dry air mole fractions. Furthermore, flask measurements from the background station Mace Head (MHD) on the West coast of Ireland are also included (Dlugokencky et al., 2019a; and Dlugokencky, 2019b).	20
<i>Fig. 12: ²²²Rn measurements at Atmospheric Observatory (building 77r). The figure shows the time series of hourly mean ²²²Radon activity, collected at 100m height, between December 2016 and December 2018.</i>	20
Fig. 13: Values of δ ¹³ C _s for CO ₂ estimated for the periods spring – summer 2018 (a) and autumn – winter 2018 (b). Each point represents the intercept of the geometric mean regression applied to the Keeling plot values for a specific night.	22
Fig. 14: Values of δ ¹³ C _s for CH ₄ estimated for the periods spring – summer 2018 (a) and autumn – winter 2018 (b). Each point represents the intercept of the geometric mean regression applied to the Keeling plot values for a specific night.	23
Fig. 15: most recent map of the EMEP stations across Europe (2017) taken from the 2019 Chemical co-ordinating Centre (CCC) report.	24

Fig. 16: Atmospheric short-lived species measurements performed at the JRC-Ispra atmospheric observatory since 1985.....	26
<i>Fig. 17. Short-lived pollutants' data coverage for year 2018.</i>	28
Fig. 18. Sampling inlet system for the gaseous air pollutant at the mobile lab. Inlet for the measurements is about 5 m above ground	31
Fig. 19: particle number size distribution observed at both ends of the horizontal part of the aerosol manifold (Dec. 2017).....	34
Fig. 20: MAAP detection chamber (sketch from the manual of the instrument).....	39
Fig. 21: Set-up of the Data Acquisition System.	42
Fig. 22: Graphic user interface of the EMEP-GAW station data evaluation.	44
Fig. 23. EMEP inter-laboratory comparisons for rainwater analyses (1987-2018): JRC-Ispra results.	46
Fig. 24. JRC-Ispra instrument's (#22) performance for the determination of (top) total carbon (TC) and (bottom) elemental carbon (EC/TC ratio) during the ACTRIS inter-laboratory comparison 2018-1.	46
Fig. 25: Solar global irradiation, precipitation amount, and temperature monthly values observed at the Observatory in Ispra in 2018, compared to the 1990-2010 period \pm standard deviations.	48
Fig. 26. Seasonal variations of the 24 hr averaged concentrations of SO ₂ , CO, NO ₂ , NO, O ₃ and NO _x in 2018 (thin lines) and 1990-2010 monthly averages (thick lines: yellow=SO ₂ , blue=CO, green=NO ₂ , orange=O ₃). Concentrations are in EMEP standard conditions (1013 hPa, 293K). 50	50
Fig. 27: AOT 40 (ppb h), SOMO35 (ppb day) and number of exceedances of the 1hr-averaged 180 $\mu\text{g}/\text{m}^3$ threshold in 2018 (bars). Lines show values for the reference period 1990-2010. 51	51
Fig. 28: 24hr-integrated PM _{2.5} mass concentrations from off-line gravimetric measurements at 20 % RH and chemical determination of main constituents in 2018.	52
Fig. 29. Regressions between the gravimetric PM _{2.5} measurements at 20 % RH and the sum of PM _{2.5} chemical constituents (left), and the FDMS-TEOM PM ₁₀ measurements (right) in 2018.52	52
Fig. 30 24-hr integrated concentrations of the main PM _{2.5} constituents in 2018, and the relative unaccounted mass	54
Fig. 31. SO ₄ ²⁻ + NO ₃ ⁻ vs. NH ₄ ⁺ ($\mu\text{eq}/\text{m}^3$) in PM _{2.5} for 2018	56
Fig. 32: Average composition of PM _{2.5} in 2018 for days on which PM _{2.5} > 25 $\mu\text{g}/\text{m}^3$ (top) and 3 < PM _{2.5} < 10 $\mu\text{g}/\text{m}^3$ (bottom), over cold (Jan., Feb., Mar., Nov., Dec.) and warm (Apr. – Oct.) months.	56
Fig. 33. 24 hr – averaged particle number concentrations for Dp < 800 nm and Dp >500 nm.	58
Fig. 34. 24 hr - averaged particle geometric mean mobility diameter (from DMPS) and standard deviation.....	58
Fig. 35. 24 hr - averaged particle volume concentrations for Dp< 800 nm and Dp > 800 nm.58	58
Fig. 36. Monthly mean particle number (left) and volume (right) size distributions measured in 2018 with a DMPS (10-800 nm, solid lines) and an APS (0.85-10 μm , dashed lines). Particle densities of 1.4 g cm⁻³ for cold months and 1.1 g cm⁻³ for warm months (May –Oct.) were used to convert aerodynamic to geometric diameters.....	60
Fig. 37. 2018 regressions between (left) PM _{2.5} mass concentrations determined from gravimetric measurements at 20% RH and particle volume (Dp < 2.5 μm) calculated from DMPS and APS measurements (<40% RH), and (right) between PM ₁₀ mass concentrations measured with the TEOM-FDMS at 30 % RH and particle volume (Dp < 10 μm) at <40% RH.	60
Fig. 38. Daily mean atmospheric particle light scattering (top), backscattering (middle), and absorption (bottom) coefficients at three wavelengths, derived from Nephelometer, Aethalometer and MAAP measurements (not corrected for RH) performed in 2018.	62

Fig. 39. Comparison between the Aethalometer and MAAP derived light absorption coefficients at 660 and 670 nm, respectively. Data points are daily averages (360) from 2018.....	63
Fig. 40. Aerosol 24-hr averaged single scattering albedo and backscatter to total scatter ratio at three wavelengths corresponding to blue, green and red light, as calculated for 2018 (RH < 40%).....	64
Fig. 41. Regression between the aerosol extinction coefficient and PM ₁₀ mass (FDMS-TEOM) and volume (DMPS + APS) concentrations in 2018.	64
Fig. 42. Aerosol vertical profile measurements performed daily with the Raman Lidar in 2018.	66
Fig. 43. Scheduled aerosol vertical profiling measurements performed monthly during the EARLINET climatology and Calipso overpass time slots in 2018.	66
<i>Fig. 44: Examples of results of the inter-comparison with an ACTRIS-reference LiDAR (red).</i>	66
Fig. 45 (a) Precipitation amount, conductivity and (b) concentrations of 3 major ions in precipitation (bars) and pH (crosses) in 2018, and during the 1990-99 period (line).....	68
Fig. 46. Wet deposition fluxes of 3 main ions measured in rain water in 2018.	68
Fig. 47. Oxidised sulphur species monthly mean concentrations and yearly wet deposition. ...	70
<i>Fig. 48. Oxidised nitrogen species monthly mean concentrations and yearly wet deposition. .</i>	70
Fig. 49. Reduced nitrogen species monthly mean concentration and yearly wet deposition. ...	70
Fig. 50. Particulate matter mass concentration monthly (grey) and annual (black) averages. The red line is the long term trend over annual averages. All values are gravimetric measurements or estimates from gravimetric measurements.	72
Fig. 51. Ozone yearly and monthly mean concentrations.	72
Fig. 52. Number of O ₃ limit value exceedances (days) and AOT40 and SOMO35 values.	72
Fig. 53. Particle number (left) and volume (right) monthly mean concentrations.	74
Fig. 54. Aerosol green light scattering and absorption monthly mean coefficients	74
Fig. 55. Aerosol optical characteristics at 550 nm (monthly means): single scattering albedo and backscatter ration (left hand axis) and scattering Ångström exponent (right hand axis).	74
Fig. 56: the flux tower of 24 m at the Pinus pinea site in San Rossore	78
Fig. 57: Measurement principle of sonic anemometers, sketch from www.gill.co.uk	83
Fig. 58: LI-7200 analyser head (from www.licor.com), arrow indicates sampling volume	83
Fig. 59: Sketch of a soil heat flux sensor (drawing from www.wikipedia.org)	85
Fig. 60: Principle of water level calculation using the Diver (sketch from www.swstechnology.com).	85
Fig. 61: Time evolution of the daily averaged Air Temperature (red) and daily total precipitation (blue) records for San Rossore forest station.	88
Fig. 62: Daily averages of the four components of the radiation budget above the San Rossore forest: ShortWave incoming (SW_IN, red), ShortWave reflected (SW_OUT, green), LongWave incoming (LW_IN, blue) and LongWave emitted (LW_OUT, black)	88
Fig. 63: Wind Rose reporting the distribution of all half-hourly direction of provenances of the wind above the San Rossore forest.....	89
Fig. 64: Measurements of soil temperature at six different depths in the ground of San Rossore forest	90
Fig. 65: Measurements of soil water content at five different depths and water table depth in the ground of San Rossore forest.	90

Fig. 66: Daily sums of the three components of the carbon cycle between San Rossore forest and the atmosphere: Net Ecosystem Exchange (NEE), Gross Primary Production (GPP) and Ecosystem Respiration (Reco).....	92
Fig. 67: Yearly trend of the three components of the carbon cycle between San Rossore forest and the atmosphere: Net Ecosystem Exchange (NEE), Gross Primary Production (GPP) and Ecosystem Respiration (Reco).....	92
Fig. 68: Daily sums of the energy fluxes between San Rossore forest and the atmosphere: Latent heat and Sensible Heat	94
Fig. 69: Yearly trend of the cumulative sum of the energy fluxes between San Rossore forest and the atmosphere: Latent heat and Sensible Heat.....	94

List of tables

Table 1: Source signatures for $\delta^{13}\text{C}_s - \text{CO}_2$	12
Table 2: Source signatures for $\delta^{13}\text{C}_s - \text{CH}_4$ of different sources (<i>Dlugokencky et.al, 2011</i>). ...	12
Table 3: Measurement sequence of Picarro G2401. This cycle is repeated continuously every hour.	13
Table 4: Variables related to short-lived pollutants and radiative forcers measured in 2018..	28
Table 5: Parameters of the EUSAAR-2 analytical protocol	40
Table 6: Annual mean concentrations and contributions of major $\text{PM}_{2.5}$ constituents in 2018.	57
Table 7: Mean aerosol chemical composition ($\text{PM}_{2.5}$) in 2017 and extinction cross section.....	65
Table 8: Statistics relative to the precipitation samples collected in 2018 (averages are volume weighted), compared to long-term averages.	69
Table 9: ICOS class 2 Ecosystem Station core parameters.	80
Table 10: ICOS variables measured continuously during 2018 in San Rossore	80
Table 11: Processing steps for flux calculations using the EdiRe Software package.	86
Table 12: Carbon fluxes at the forest station of San Rossore in 2018.....	93

GETTING IN TOUCH WITH THE EU

In person

All over the European Union there are hundreds of Europe Direct information centres. You can find the address of the centre nearest you at: https://europa.eu/european-union/contact_en

On the phone or by email

Europe Direct is a service that answers your questions about the European Union. You can contact this service:

- by freephone: 00 800 6 7 8 9 10 11 (certain operators may charge for these calls),
- at the following standard number: +32 22999696, or
- by electronic mail via: https://europa.eu/european-union/contact_en

FINDING INFORMATION ABOUT THE EU

Online

Information about the European Union in all the official languages of the EU is available on the Europa website at: https://europa.eu/european-union/index_en

EU publications

You can download or order free and priced EU publications from EU Bookshop at: <https://publications.europa.eu/en/publications>. Multiple copies of free publications may be obtained by contacting Europe Direct or your local information centre (see https://europa.eu/european-union/contact_en).

The European Commission's science and knowledge service

Joint Research Centre

JRC Mission

As the science and knowledge service of the European Commission, the Joint Research Centre's mission is to support EU policies with independent evidence throughout the whole policy cycle.



EU Science Hub

ec.europa.eu/jrc



@EU_ScienceHub



EU Science Hub - Joint Research Centre



Joint Research Centre



EU Science Hub

